UQAR Université du Québec à Rimouski

OPTIMISATION DES PARAMÈTRES DE FABRICATION ADDITIVE ET DES TRAITEMENTS THERMIQUES POUR L'AMÉLIORATION DES PROPRIÉTÉS MÉCANIQUES DE L'ACIER INOXYDABLE 17-4 PH EN VUE D'APPLICATIONS DE HAUTE PERFORMANCE

Mémoire présenté

dans le cadre du programme de maîtrise en ingénierie

en vue de l'obtention du grade de maître ès sciences appliquées (M.Sc.A.)

PAR

© YASSMINE CHEDLY

Août 2025

Composition du jury :

Éric Villeneuve, président du jury, Université du Québec à Rimouski

Noureddine Barka, directeur de recherche, Université du Québec à Rimouski

Ilyes Maamri, examinateur externe, Tekna

Hendra Hermawan, examinateur externe, Université Laval

Dépôt initial le 09 Juillet 2025 Dépôt final le 28 Août 2025

UNIVERSITÉ DU QUÉBEC À RIMOUSKI
Service de la bibliothèque

Avertissement

La diffusion de ce mémoire ou de cette thèse se fait dans le respect des droits de son auteur, qui a signé le formulaire « *Autorisation de reproduire et de diffuser un rapport, un mémoire ou une thèse* ». En signant ce formulaire, l'auteur concède à l'Université du Québec à Rimouski une licence non exclusive d'utilisation et de publication de la totalité ou d'une partie importante de son travail de recherche pour des fins pédagogiques et non commerciales. Plus précisément, l'auteur autorise l'Université du Québec à Rimouski à reproduire, diffuser, prêter, distribuer ou vendre des copies de son travail de recherche à des fins non commerciales sur quelque support que ce soit, y compris Internet. Cette licence et cette autorisation n'entraînent pas une renonciation de la part de l'auteur à ses droits moraux ni à ses droits de propriété intellectuelle. Sauf entente contraire, l'auteur conserve la liberté de diffuser et de commercialiser ou non ce travail dont il possède un exemplaire.

À mes chers parents.

REMERCIEMENTS

Je tiens tout d'abord à exprimer ma profonde gratitude à mon directeur de recherche, Noureddine Barka, pour sa précieuse orientation, ses conseils avisés et son soutien tout au long de ce travail. Sa rigueur scientifique et sa bienveillance ont été des sources d'inspiration qui ont grandement contribué à l'avancement et à la réussite de ce projet.

Je souhaite également remercier chaleureusement toute l'équipe du laboratoire des Matériaux, Produits et Procédés de Pointe (LMP3), tout particulièrement Narges Omidi et Asim Iltaf pour l'accueil qui m'a été réservé, les moyens techniques mis à ma disposition et les échanges enrichissants qui ont jalonné cette expérience. Leur implication m'a été d'une grande aide dans la réalisation des expériences et des analyses.

Mes remerciements s'adressent également aux personnes qui ont contribué, de près ou de loin, à la concrétisation de ce travail. Je pense notamment à Samuel Gagnon, Charles-André Fraser et Dany Morin, pour leur appui technique.

Je n'oublie pas mes amis : A, D, O, H, N, A, M qui ont toujours été présents pour m'encourager et partager des moments de convivialité, apportant ainsi un équilibre essentiel durant cette période spéciale et exigeante.

Enfin, je tiens à exprimer toute ma gratitude à mes parents Hanene & Jamel pour leur amour infini, leur encouragement et leur confiance inébranlable en mes capacités. Un grand merci à mon petit frère Yassine pour sa présence et son soutien. J'aimerai remercier toute ma grande famille pour leurs encouragements et leur affection qui ont été d'un grand réconfort.

RÉSUMÉ

Cette étude vise à optimiser les paramètres de fabrication de pièces en acier inoxydable martensitique 17-4 PH produites par fusion laser sur lit de poudre (LPBF). En raison du manque de données exhaustives concernant l'influence des paramètres de fabrication et des traitements thermiques sur les performances finales de ce matériau, ce travail propose une analyse approfondie pour identifier les combinaisons optimales adaptées à diverses exigences mécaniques et industrielles.

L'approche expérimentale rigoureuse adoptée repose sur une méthodologie structurée intégrant des plans d'expérience Taguchi, différents traitements thermiques spécifiques (H900, H1025, H1150), ainsi que deux orientations d'impression (0° et 45°). Les propriétés mécaniques étudiées incluent la microdureté, la résistance à la traction, la ténacité au choc (essai Charpy) et le comportement en fatigue. L'analyse détaillée de la microstructure et des surfaces de rupture (fractographie) a permis de mieux cerner les mécanismes influencés par les paramètres du procédé et les traitements thermiques.

Les résultats mettent clairement en évidence le rôle prépondérant de la température de vieillissement sur les propriétés mécaniques et microstructurales finales. Le traitement thermique H1150 (620°C) favorise nettement une ductilité élevée et une excellente résistance à l'impact (120 J). À l'inverse, les traitements à plus basse température (H900, 480°C) améliorent considérablement la dureté et la résistance mécanique, mais réduisent fortement la ductilité, entraînant un comportement plus fragile du matériau. L'optimisation rigoureuse de la densité d'énergie volumique (VED) s'est révélée essentielle afin de minimiser la porosité résiduelle et d'assurer des propriétés mécaniques équilibrées.
Par ailleurs, l'analyse du comportement en fatigue met en évidence une influence marquée de l'orientation d'impression sur la durée de vie des pièces. Notamment, les échantillons imprimés à 45° présentent une meilleure résistance à la propagation des fissures, ce qui améliore significativement leurs performances en fatigue.

Ces résultats offrent des recommandations pratiques précieuses aux industries qui souhaitent intégrer la fabrication additive métallique dans leur processus de fabrication. Cette recherche leur permet ainsi d'ajuster précisément les paramètres de procédé afin de répondre efficacement à des critères mécaniques spécifiques, répondant ainsi aux exigences de performance industrielle les plus élevées.

Mots clés : Fabrication additive métallique, LPBF, acier inoxydable 17-4 PH, optimisation des paramètres, propriétés mécaniques, traitements thermiques, fatigue, résistance au choc, microstructure, orientation d'impression.

ABSTRACT

This study aims to optimize the production parameters for martensitic stainless steel 17-4 PH components manufactured by Laser Powder Bed Fusion (LPBF). Given the limited availability of comprehensive data on the precise effects of manufacturing parameters and heat treatments on the final performance of this material, this research provides an in-depth analysis to identify optimal parameter combinations suited to specific mechanical and industrial requirements.

A systematic experimental approach employing a structured methodology, including Taguchi experimental designs, specific heat treatments (H900, H1025, H1150), and two build orientations (0° and 45°), was adopted. The mechanical properties investigated encompass microhardness, tensile strength, impact toughness (Charpy test), and fatigue behavior. Detailed microstructural and fractographic analyses enabled a deeper understanding of the underlying mechanisms influenced by process parameters and thermal treatments.

Results clearly highlight the predominant influence of aging temperature on final mechanical and microstructural properties. The H1150 treatment (620°C) significantly promotes high ductility and excellent impact resistance (120 J). Conversely, lower aging temperatures (H900, 480°C) substantially increase hardness and strength but drastically reduce ductility, resulting in increased material brittleness. Rigorous optimization of volumetric energy density (VED) was crucial to achieving minimal residual porosity and balanced mechanical properties.
Furthermore, fatigue behavior analysis revealed a marked impact of build orientation on fatigue life. Particularly, specimens printed at 45° demonstrated superior resistance to crack propagation, which significantly improves their fatigue performance.

These findings provide valuable practical guidelines for industries aiming to incorporate metal additive manufacturing into their processes, enabling precise adjustments of manufacturing parameters to meet specific mechanical performance requirements and industrial standards.

Keywords: Metal additive manufacturing, LPBF, 17-4 PH stainless steel, parameter optimization, mechanical properties, heat treatments, fatigue, impact toughness, microstructure, build orientation.

TABLE DES MATIÈRES

LISTE DES TABLEAUX

LISTE DES FIGURES

LISTE DES ABRÉVIATIONS, DES SIGLES ET DES ACRONYMES

AM	Additive Manufacturing (Fabrication Additive)
LPBF	Laser Powder Bed Fusion (Fusion Laser sur Lit de Poudre)
SLM	Selective Laser Melting
EOS	Electro Optical Systems
PH	Precipitation Hardening (Durcissement par précipitation)
ASTM	American Society for Testing and Materials
MEB	Microscope Électronique à Balayage
EDS	Spectroscopie à Dispersion d'Énergie
UTS	Ultimate Tensile Strength (Résistance à la traction ultime)
YS	Yield Strength (Limite d'élasticité)
VED	Volumetric Energy Density (Densité d'Énergie Volumique)
HIP	Hot Isostatic Pressing (Pressage Isostatique à Chaud)
LCF	Low-Cycle Fatigue (Fatigue à faible nombre de cycles)
HCF	High-Cycle Fatigue (Fatigue à grand nombre de cycles)

LISTE DES SYMBOLES

P	Puissance du laser **(W)**
V	Vitesse de balayage **(mm/s)**
HD	Espacement des hachures **(µm)**
t	Épaisseur de couche **(µm)**
ρ	Densité relative **(%)**
UTS	Résistance à la traction ultime **(MPa)**
YS	Limite d’élasticité **(MPa)**
EL	Allongement **(%)**
HV	Dureté Vickers
HRC	Dureté Rockwell C
E	Module d'élasticité **(GPa)**
N	Nombre de cycles à rupture
R	Ratio de charge (σmin/σmax)

INTRODUCTION GÉNÉRALE

1. MISE EN CONTEXTE

La fabrication additive, communément appelée impression 3D, constitue une avancée technologique majeure dans l'industrie manufacturière. Contrairement aux méthodes soustractives classiques, qui enlèvent progressivement du matériau pour obtenir la pièce finale, la fabrication additive construit les objets couche par couche, réduisant ainsi le gaspillage de matière tout en permettant de réaliser des formes géométriques complexes, souvent impossibles à obtenir autrement [1].

Depuis son apparition dans les années 1980, cette technologie, initialement dédiée au prototypage rapide, s'est étendue à divers secteurs industriels stratégiques tels que l'aéronautique, l'automobile, la médecine et l'électronique, principalement grâce aux progrès significatifs réalisés dans les matériaux et les procédés [2]. La fabrication additive métallique occupe une place centrale parmi ces innovations grâce à sa capacité à produire des pièces robustes, légères et extrêmement complexes, répondant ainsi à des exigences industrielles de plus en plus élevées. Parmi les différents procédés disponibles, la fusion laser sur lit de poudre (LPBF) se démarque particulièrement par sa précision exceptionnelle et sa capacité à réaliser des géométries complexes [3].

Le procédé LPBF utilise un laser de haute puissance pour fusionner sélectivement des couches successives de poudre métallique. Chaque couche de poudre est uniformément déposée, puis solidifiée localement selon le parcours du faisceau, permettant d'obtenir des pièces denses et aux géométries complexes, comme illustré sur la Figure 1.

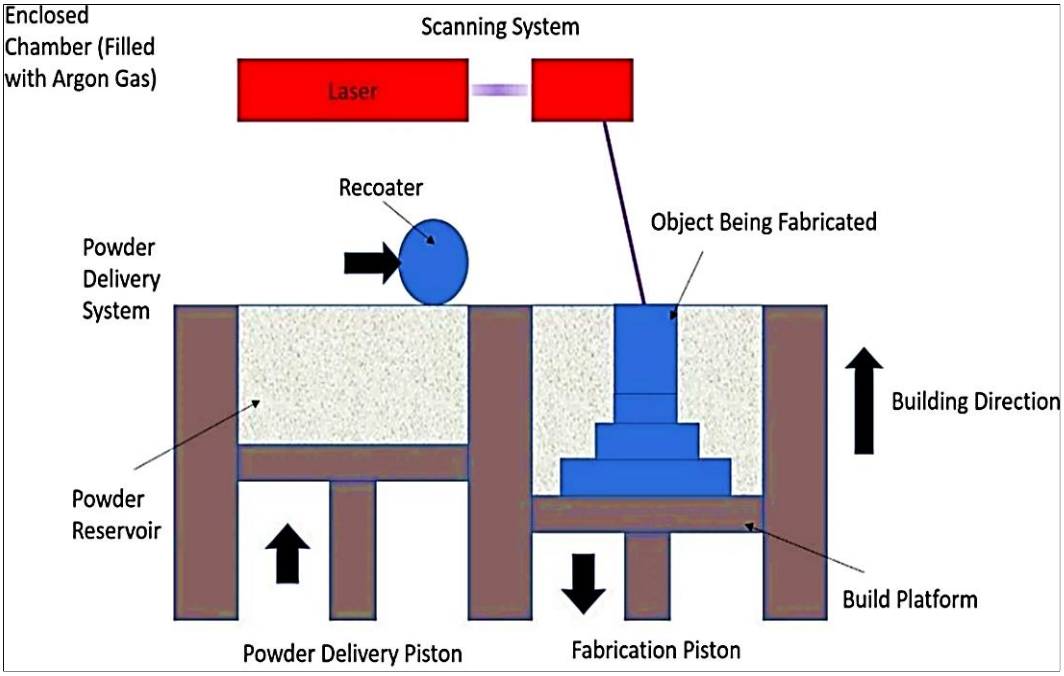

Figure 1: Schéma de principe du procédé de fusion laser sur lit de poudre (LPBF) [4].

Cette technologie s’est rapidement développée grâce aux avancées réalisées dans les domaines du laser, de la robotique et du traitement numérique, rendant possible l'intégration de matériaux variés tels que les alliages d’aluminium, les superalliages à base de nickel et les aciers inoxydables [5]. Néanmoins, la complexité du procédé LPBF provient principalement de la sensibilité des paramètres interconnectés impliqués, tels que la puissance et la vitesse du laser, l’épaisseur des couches de poudre, l’espacement des hachures, ainsi que les conditions d'inertage et la densité d'énergie appliquée, comme illustré dans la Figure 2. Toute variation minime de ces paramètres peut induire des défauts critiques tels que des porosités, des déformations résiduelles ou des microfissures, compromettant ainsi la qualité et la performance finale des pièces [7], [8].

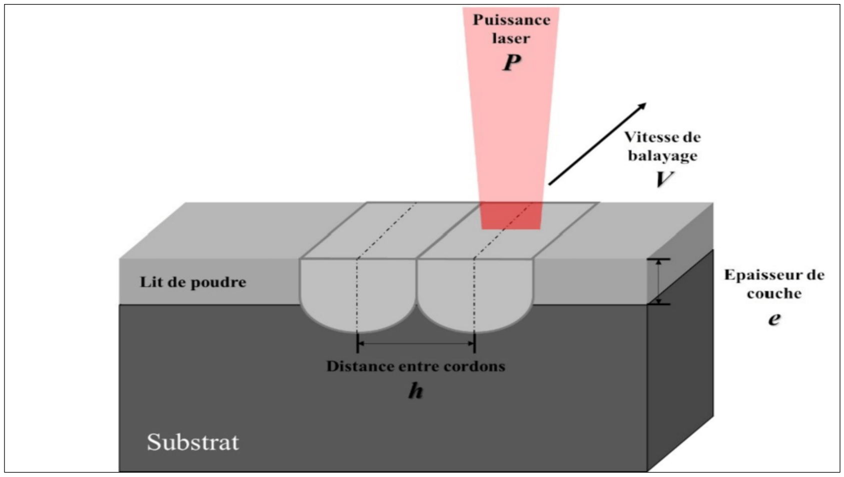

Figure 2: Schéma représentatif de la stratégie du processus fusion laser sur lit de poudre [6].

Par conséquent, un contrôle rigoureux du processus de fabrication s'avère indispensable pour garantir non seulement la qualité finale des pièces, mais aussi leur reproductibilité. Cette maîtrise implique une gestion précise de plusieurs aspects critiques, tels que la caractérisation minutieuse des poudres métalliques utilisées, la surveillance en temps réel des paramètres clés et l'utilisation avancée d'outils de simulation numérique pour prédire les interactions thermiques et mécaniques durant la fabrication. L'objectif étant d'anticiper les anomalies et de minimiser les risques d'erreurs afin d'assurer une fabrication fiable et répétitive.

Malgré les progrès notables réalisés, la technologie LPBF reste confrontée à plusieurs défis majeurs. Parmi ceux-ci figurent la maîtrise des propriétés anisotropes induites par le processus de fabrication couche par couche, ainsi que l'influence complexe des traitements thermiques, tels que le vieillissement, sur les propriétés mécaniques finales des pièces produites [9]. Ces traitements sont essentiels pour ajuster la microstructure, améliorer les propriétés mécaniques et atteindre les performances requises par les applications industrielles critiques. Toutefois, leur interaction précise avec les paramètres du procédé LPBF reste mal maîtrisée, nécessitant ainsi une étude approfondie pour optimiser ces interactions complexes.

C’est précisément dans ce cadre que s’inscrit ce travail de recherche. L’objectif principal de cette étude est d'examiner rigoureusement l’effet combiné des paramètres de fabrication LPBF et des traitements thermiques spécifiques sur les propriétés mécaniques et microstructurales de l’acier inoxydable 17-4 PH. La contribution originale réside particulièrement dans l'approche expérimentale et statistique adoptée pour déterminer les paramètres optimaux qui garantissent une qualité optimale et reproductible des pièces produites.

En outre, cette recherche apporte une compréhension approfondie des mécanismes à l’origine de la porosité résiduelle et de l’anisotropie des propriétés mécaniques, contribuant directement à améliorer la fiabilité globale du procédé LPBF. À travers l’analyse expérimentale précise des effets des paramètres critiques tels que la densité d'énergie et les conditions de vieillissement, cette étude propose des stratégies concrètes permettant un meilleur contrôle des propriétés finales des pièces fabriquées par LPBF.

Enfin, le coût élevé associé aux matériaux et aux équipements LPBF constitue toujours un frein important à l’adoption élargie de cette technologie. Cependant, l’optimisation des paramètres du procédé peut significativement réduire le gaspillage de matière et augmenter l’efficacité économique à long terme, favorisant ainsi une adoption plus large par l'industrie [10].

En conclusion, ce travail contribue activement aux efforts actuels visant à relever les défis techniques et économiques majeurs de la fabrication additive métallique, en particulier la technologie LPBF. Cette recherche s’insère dans une approche multidisciplinaire indispensable pour optimiser et démocratiser cette technologie prometteuse.

2. REVUE DE LITTÉRATURE

Les caractéristiques finales des matériaux produits par LPBF sont étroitement liées aux paramètres du processus et aux traitements thermiques post-fabrication.

De nombreuses recherches ont examiné ces éléments afin d'améliorer la microstructure, les propriétés mécaniques et la résistance à la fatigue des alliages métalliques, notamment l'acier inoxydable 17-4 PH.

L'étude réalisée par Bae et al. [11] est une recherche expérimentale et numérique portant sur l'acier 17-4 PH fabriqué par LPBF et par pressage isostatique à chaud (HIP). Le but de cette étude était d'optimiser les paramètres du procédé pour réduire la porosité et la déformation thermique, tout en améliorant les caractéristiques mécaniques. Les résultats ont mis en évidence qu'une densité d'énergie optimale d'environ 84,92 J/mm³ s'est avérée efficace pour la réduction de la porosité et l'atténuation de la déformation thermique. L'application du traitement HIP a entraîné une amélioration de la densité, de la dureté et de la résistance du matériau. Néanmoins, la création d'une structure martensitique plus uniforme s'est traduite par une réduction de la ductilité. Cette étude met en évidence la nécessité d'atteindre un équilibre entre la densité d'énergie et le post-traitement, afin de concevoir des composants fiables et de hautes qualités adaptées aux applications d'ingénierie critiques.

Dans la recherche réalisée par Sahadevan et al. [12], la méthode Taguchi a été appliquée pour analyser l'impact des paramètres critiques du processus, à savoir la puissance du laser, la vitesse de balayage et l'espacement des hachures, sur la microdureté de l'acier inoxydable 17-4 PH fabriqué par fusion sélective au laser (SLM). Les résultats indiquent que la puissance du laser a eu la plus grande influence sur la microdureté, suivie par la vitesse de balayage et l'espacement des hachures. Les paramètres optimaux ayant conduit à une microdureté maximale de 351.2 HV, ont été identifiés comme une puissance laser de 300 W, une vitesse de balayage de 1 000 mm/s et une distance de balayage de 0.08 mm. Il a été démontré que la régulation de ces paramètres est cruciale pour obtenir une microdureté élevée pour les pièces fabriquées par SLM, ce qui suggère que cette approche pourrait être exploitée pour optimiser d'autres processus de fabrication additive dans un contexte industriel.

Cette étude d'Otsuka et al. [13] examine la relation entre les défauts et la microstructure concernant la résistance à la fatigue de l'acier inoxydable 17-4 PH durci par précipitation et produit par LPBF. Les microfissures et les agrégats de carbure autour des défauts tels que les pores affectent de manière significative l'initiation et la propagation des fissures de fatigue.

L'estimation du modèle de Murakami indique que la zone entourant les défauts améliore la prédiction de la limite d'endurance. En outre, le traitement thermique augmente la variabilité microstructurale, en particulier dans les zones contenant des défauts, ce qui peut diminuer finalement la résistance à la fatigue. L'optimisation efficace des paramètres du processus peut améliorer significativement la résistance à la fatigue.

Li et al. [14] ont étudié la microstructure et les propriétés mécaniques de l'acier inoxydable 17-4 PH produit par LPBF et subissant un traitement thermique. La recherche montre qu'après le traitement en solution, l'austénite se transforme en martensite, tandis que le traitement de vieillissement à 450°C précipite des nanoparticules de NbC et de ε-Cu, qui améliorent considérablement la résistance à la traction. Dans ces conditions de vieillissement, le matériau présente une résistance ultime à la traction (UTS) de 1387 MPa et un allongement de 7,3 %, ce qui représente une augmentation de 25,2 % de l'UTS par rapport à l'état tel qu'il est imprimé. Cependant, à mesure que la température de vieillissement augmente, les précipités deviennent plus grossiers, ce qui réduit la résistance mais améliore la ductilité.

Cette étude d'Afkhami et al. [15] explore l'influence des paramètres de fabrication du LPBF et des traitements d'impact mécanique à haute fréquence (HFMI) sur les propriétés mécaniques de l'acier inoxydable 316L. Les auteurs ont constaté que le traitement HFMI améliorait considérablement la résistance à la fatigue et la limite d'élasticité par rapport aux échantillons tels que construits, mais au prix d'une ductilité réduite et d'une augmentation des défauts de surface. L'analyse microstructurale a montré la formation d'une structure austénitique monophasée avec de fines sous-structures cellulaires. L'étude conclut que si le HFMI est efficace pour améliorer la résistance statique et la résistance à la fatigue, une optimisation plus poussée est nécessaire pour atténuer les imperfections de surface qui pourraient entraîner une défaillance prématurée sous charge cyclique.

Les recherches menées par Huang et al. [16], Li et al. [14], ainsi qu'Eisazadeh et al. [17] analysent de manière collective l'impact du traitement thermique sur la microstructure et les propriétés mécaniques de l'acier inoxydable 17-4 PH, obtenu par LPBF. L'ensemble de ces recherches met en évidence l'importance cruciale des traitements thermiques post-processus dans l'optimisation de la microstructure ainsi que des propriétés mécaniques, notamment la résistance, la ductilité et la dureté. Plus précisément, Huang et al. [16] ont examiné les traitements H900, H1025 et H1150, mettant en évidence l'impact de ces conditions sur le comportement mécanique. Eisazadeh et al. [17] ont réalisé une étude comparative entre le 17-4 PH produit par LPBF et celui produit par des méthodes conventionnelles, mettant en évidence que les traitements thermiques améliorent les propriétés mécaniques dans les deux cas.

Il apparaît donc judicieux d'analyser en profondeur l'effet synergique des paramètres du procédé LPBF et des traitements thermiques post-fabrication appliqués à l'acier 17-4 PH, notamment en ce qui concerne les transformations microstructurales, les propriétés mécaniques et le comportement en fatigue. Cette étude permettrait de faciliter l'intégration et l'adoption de ce procédé et de ce matériau dans des applications industrielles critiques, telles que l'aéronautique, qui nécessitent des performances élevées et une grande fiabilité. L'importance de cette recherche réside dans l'optimisation des paramètres combinés de fabrication pour produire des pièces de haute qualité et de propriétés mécaniques élevées. À notre connaissance, peu d'études se sont concentrées sur l'optimisation combinée des paramètres du procédé LPBF et des traitements thermiques appliqués à l'acier 17-4 PH tout en investiguant la microstructure, les propriétés mécaniques et le comportement en fatigue. Cette contribution est donc cruciale pour combler cette lacune et pour proposer des lignes directrices applicables à des secteurs industriels exigeants, où la fiabilité et la performance des pièces sont primordiales.

3. PROBLÉMATIQUE

Malgré les avancées significatives dans le domaine de la fabrication additive, de nombreux défis persistent, justifiant la nécessité de poursuivre les recherches sur l'optimisation des paramètres du procédé LPBF, en raison de sa complexité et de sa sensibilité [18], [19]. La porosité, la formation de microfissures et les propriétés mécaniques anisotropes sont les principaux défauts résultant des difficultés de contrôle des conditions de fabrication et des traitements thermiques, compromettant ainsi les performances et la fiabilité des composants critiques [20], [21].

La performance optimale sera atteinte lorsque les paramètres de fabrication, tels que la densité d'énergie appliquée et les conditions de refroidissement, seront adéquats. Les traitements thermiques jouent un rôle essentiel dans l'établissement des propriétés finales des pièces, mais ils sont très sensibles aux conditions initialement établies lors de la fabrication [22], [23].

Par conséquent, la question générale de cette recherche est la suivante : Quels sont les paramètres du procédé LPBF et des traitements thermiques optimaux pour fabriquer des pièces en acier 17-4 PH avec des propriétés mécaniques et une microstructure idéales, répondant aux exigences strictes des industries aérospatiale, automobile et maritime ? Cette étude vise à réduire la variabilité des propriétés, à améliorer la densité et la résistance des pièces, en élaborant des stratégies robustes de contrôle qualité. Parallèlement, ce travail contribuera à l'avancement des connaissances scientifiques sur la façon dont les paramètres de fabrication interagissent avec les traitements thermiques de manière complexe.

Finalement, ce travail vise à présenter des recommandations pratiques pour les industries, basées sur une analyse approfondie des interactions entre les paramètres de fabrication, les traitements thermiques et les performances des matériaux. Cela permet non seulement la compréhension du processus, mais aussi la proposition des solutions pratiques aux problèmes actuels pour une adoption plus contrôlée et large de la technologie LPBF et de l'acier 17-4 PH au sein des secteurs critiques.

4. OBJECTIFS

La fabrication additive a connu une révolution et un développement considérable ces dernières années. L'utilisation des diverses techniques de fabrication additive dans les lignes de production offre des avantages significatifs, tels que la réduction des déchets et la possibilité de produire des pièces avec une complexité accrue. Cependant, ces technologies restent relativement coûteuses et nécessitent une maîtrise approfondie et une compréhension rigoureuse des processus et des phénomènes en jeu pour éviter les erreurs et améliorer leur adoption.

Comme souligné précédemment, le procédé LPBF est actuellement reconnu comme l'une des technologies les plus performantes en matière de fabrication additive métallique. Il offre la possibilité de fabriquer des composants de haute qualité et grande fiabilité, pouvant rivaliser, voire dépasser, les composants produits de façon traditionnelle.

De plus, les industries aérospatiale et marine montrent un intérêt croissant pour l'intégration de l'acier martensitique 17-4 PH dans leurs applications critiques, en raison de ses excellentes propriétés mécaniques et de sa résistance à la corrosion. Parallèlement, elles s'ouvrent de plus en plus à l'utilisation de la fabrication additive pour répondre à leurs besoins de production.

Dans ce contexte, cette recherche vise à explorer les propriétés mécaniques, les caractéristiques microstructurales, le comportement en fatigue et la durée de vie de l'acier 17-4 PH fabriqué par le procédé LPBF à l'aide de la machine EOS M290 disponible dans le laboratoire. Une étude approfondie de l'effet combiné des paramètres du procédé LPBF et des traitements thermiques sera réalisée, grâce à des paramètres de production bien définis et justifiées. L'objectif ultime est d'optimiser la conception et la production des pièces, de garantir leur fiabilité et de maximiser leur durée de vie. Les résultats obtenus auront des implications directes pour les industries à la recherche de solutions innovantes pour la fabrication de composants complexes, robustes et fiables.

Cette étude se décline en quatre objectifs spécifiques :

1- Évaluation expérimentale des paramètres du procédé LPBF et des traitements thermiques sur la microstructure et la microdureté de l'acier 17-4 PH :

Le premier objectif consiste à évaluer expérimentalement et statistiquement l'effet des paramètres LPBF tels que la puissance du laser, la vitesse de balayage, l'espacement des hachures et les conditions de vieillissement sur les caractéristiques microstructurales. Il s'agit également d'analyser leur impact sur les mécanismes de renforcement et la microdureté.

2- Étude comparative sur l'effet des paramètres de fabrication additive et des traitements thermiques sur les propriétés mécaniques de l'acier 17-4 PH fabriqué par LPBF en vue d'applications à haute performance :

Le deuxième objectif vise à comparer l'influence des paramètres LPBF et des traitements thermiques sur le comportement en traction de l'acier 17-4 PH. Les propriétés étudiées incluront la limite ultime de traction, la limite élastique et l'élongation. Une optimisation du nombre de tests sera effectuée, avec une corrélation systématique avec les caractéristiques microstructurales.

3- Investigation de la tenacité de l'acier 17-4 PH fabriqué par LPBF :

Le troisième objectif porte sur l'étude des propriétés d'impact de l'acier 17-4 PH via des tests Charpy. Les résultats obtenus seront corrélés avec les tests de traction afin de déterminer les paramètres optimaux pour les essais de fatigue, tout en optimisant le nombre de tests nécessaires.

4- Étude du comportement en fatigue de l'acier 17-4 PH après optimisation des paramètres :

Le dernier objectif est d'analyser et de comprendre le comportement en fatigue de cet acier, en faisant varier uniquement la direction d'orientation d'impression des éprouvettes tout en conservant les mêmes paramètres d'impression. Cette étape permettra de déterminer la limite d'endurance, de tracer la courbe S-N et de comparer les performances pour les deux orientations d'impression.

5. MÉTHODOLOGIE

Afin de répondre clairement aux objectifs spécifiques définis précédemment, une méthodologie structurée et rigoureuse en huit étapes a été mise en place dans cette recherche: 1) Revue de littérature, 2) Création et validation du plan d'expérience, 3) Impression et préparation des échantillons, 4) Réalisation des essais mécaniques : microdureté, traction, mesure de densité, et test d'impact Charpy, 5) Évaluation de la microstructure et analyse fractographique des surfaces de rupture, 6) Impression des échantillons pour les tests de fatigue, avec choix des paramètres optimaux et variation de l'orientation d'impression, 7) Réalisation des tests de fatigue pour les deux orientations, 8) Analyse microstructurale et fractographique après rupture.

La première étape consistait à effectuer une revue de littérature pour acquérir une compréhension approfondie des procédés LPBF. Cette analyse a permis de classifier les recherches existantes, d'identifier les phénomènes en jeu, de comprendre l'importance des traitements thermiques et leur influence, ainsi que de recenser les avancées et les limites actuelles. Cette revue a également permis de définir les objectifs précis de l'étude.

Dans la deuxième étape, pour répondre spécifiquement aux objectifs 1 et 2, un plan d'expérience comportant quatre facteurs principaux: la puissance laser, la vitesse de balayage, l'espacement des hachures et la température de vieillissement, avec trois niveaux, a été élaboré et validé. Les valeurs de ces paramètres ont été ajustées de ±10 % par rapport aux recommandations du fournisseur de poudre. Un plan d'expérience Taguchi L9, comportant quatre facteurs et trois niveaux, a été adopté pour structurer les essais.

Dans la troisième et la sixième étape, trois séries d'impressions ont été réalisées pour produire l'ensemble des échantillons nécessaires pour l'étude, conformément aux objectifs fixés. Cette étape a débuté par la conception des éprouvettes, l'ajout des supports et la préparation de la machine EOS M290. La poudre utilisée était de l'acier inoxydable EOS 17-4 PH. Après impression, un traitement thermique de relaxation des contraintes a été appliqué à tous les plateaux. Les éprouvettes ont ensuite été découpées, usinées pour obtenir leur forme finale, puis soumises à un traitement thermique complémentaire.

La quatrième étape s'est concentrée sur la caractérisation mécanique afin de répondre directement aux objectifs 1, 2 et 3. Des essais de microdureté ont été réalisés avec un appareil Clemex, tandis que les essais de traction ont suivi la norme ASTM E8/E8M avec trois répétitions par condition. Les tests d'impact Charpy, conformes à la norme ASTM E23, ont permis d'évaluer la résistance aux chocs.

Dans la cinquième étape, une étude de microstructure et de fractographie est effectuée, répondant ainsi aux objectifs 1, 2 et 3. Des images microscopiques ont été obtenues à l'aide d'un microscope optique et d'un microscope électronique à balayage (MEB) équipé d'un spectroscope à dispersion d'énergie (EDS) pour l'analyse élémentaire. La préparation des échantillons comprenait la découpe, l'enrobage, le polissage et l'attaque chimique afin de révéler la microstructure. Une analyse fractographique a été réalisée après des essais de traction et d'impact d'énergie afin d'étudier les mécanismes de rupture et de comprendre le comportement du matériau.

Lors de la sixième étape, les paramètres optimaux pour l'impression et le traitement thermique des spécimens de fatigue ont été choisis en s'appuyant sur les résultats obtenus dans les étapes précédentes. Deux orientations d'impression (0° et 45°) ont été choisies afin d'analyser leur influence sur le comportement en fatigue.

La septième étape a permis de répondre spécifiquement à l'objectif 4 en réalisant des tests de fatigue conformément à la norme ASTM E466-15. Ces essais ont conduit à l'établissement des courbes S-N et à la détermination des limites d'endurance pour les deux orientations d'impression étudiées.

Enfin, la huitième étape a complété l'analyse en réalisant une caractérisation microstructurale et fractographique approfondie après rupture, toujours dans le cadre du dernier objectif. Cette analyse finale a permis d'établir clairement les liens entre les mécanismes microstructuraux observés et les performances en fatigue des échantillons, contribuant ainsi à valider et affiner les conclusions générales de l'étude.

6. DIVISION DU MÉMOIRE

Ce mémoire est structuré en quatre parties principales.

Le premier article traite de l'influence des paramètres de fabrication additive et des traitements thermiques sur l'évolution microstructurale et la microdureté de l'acier 17-4 PH.

Le deuxième article met en évidence les résultats issus des essais de traction. L'impact des paramètres LPBF et de la température de vieillissement sur la limite ultime de traction, la limite élastique et l'élongation des différentes combinaisons a été étudié. L'article se termine par une analyse statistique approfondie qui permet de mieux comprendre l'effet de chaque paramètre sur les résultats finaux, dans le cadre d'applications à hautes performances.

Le troisième article, destiné à une conférence, présente les résultats obtenus lors du test d'impact Charpy. L'objectif est d'évaluer la capacité du matériau à absorber l'énergie et d'analyser l'impact combiné des paramètres de fabrication et de post-fabrication sur les propriétés d'impact.

Le dernier article aborde l'étude du comportement en fatigue des pièces en acier 17-4 PH fabriquées par LPBF, après l'optimisation des paramètres. Une variation de la direction d'impression a été introduite, et l'article se termine par une comparaison des résultats entre ces deux orientations.

CHAPITRE 1
ÉVALUATION STATISTIQUE ET EXPÉRIMENTALE DES PARAMÈTRES DU PROCÉDÉ LPBF ET DES TRAITEMENTS THERMIQUES SUR LA MICROSTRUCTURE ET LA MICRODURETÉ DE L'ACIER INOXYDABLE 17-4 PH

Cet article a été soumis dans "Journal of Materials Engineering and Performance" portant le numéro de référence JMEP-25-01-40398.

1.1 RÉSUMÉ EN FRANÇAIS DU PREMIER ARTICLE

Cette étude présente une évaluation expérimentale et statistique approfondie des effets des paramètres du procédé Fusion Laser sur Lit de Poudre (LPBF) – puissance du laser, vitesse de balayage, espacement des hachures – ainsi que des traitements thermiques post-LPBF sur la microstructure, la microdureté et les défauts de fabrication de l'acier inoxydable 17-4 PH. Les observations en microscopie optique révèlent qu'une plage spécifique de densité d'énergie volumétrique (VED) allant de 54,148 J/mm^3 à 88,977 J/mm^3 minimise les défauts de fabrication, les porosités étant principalement d'origine gazeuse, tandis que les défauts liés à un manque de fusion sont pratiquement éliminés. Ainsi, dans cette plage de VED, les variations de microdureté restent faibles et homogènes, indiquant que les défauts de fabrication n'ont qu'une influence marginale sur les valeurs de microdureté. L'analyse statistique des valeurs de microdureté montre que la température de vieillissement est le principal facteur influençant la microdureté, expliquant environ 96,99 % de la variation observée, avec une diminution de la microdureté à mesure que la température augmente. Un modèle prédictif des valeurs de microdureté a été établi à partir des données, avec une marge d'erreur inférieure à 5 %, offrant ainsi un outil fiable pour atteindre les niveaux de microdureté souhaités dans l'acier 17-4 PH fabriqué par LPBF. Enfin, cette étude met en

évidence qu'une plage optimale de VED, située entre 65,519 J/mm³ et 88,977 J/mm³, est idéale pour la fabrication de pièces en acier 17-4 PH.

Mots-clés : Fusion Laser sur Lit de Poudre, Acier Inoxydable 17-4 PH, Microdureté, Traitement de vieillissement, Microstructure.

Cet article, intitulé « Statistical and Experimental Evaluation of LPBF Process Parameters and Heat Treatments on the Microstructure and Microhardness of 17-4 PH Stainless Steel », a été soumis pour publication à la revue "*Journal of Materials Engineering and Performance (JMEP)"* le 13 Janvier 2025. L'évaluation par les pairs est en cours. En tant que premier auteur, j'ai principalement conçu et conduit l'ensemble des expériences, assisté aux observations microstructurales et réalisé l'analyse statistique des résultats et le modèle prédictif. J'ai également mené l'interprétation des données relatives aux paramètres du procédé LPBF et aux traitements thermiques. Narges Omidi, deuxième auteur, a supervisé l'analyse des données et assisté dans la validation des résultats expérimentaux. Elle a également contribué à la révision du manuscrit. Shayan Dehghan a aidé dans la discussion des résultats de l'analyse XRD de la microstructure. Le professeur Noureddine Barka, a apporté une contribution essentielle à la définition du cadre théorique de la recherche et à la supervision en tant que directeur principal, et Abderrazak El Ouafi comme Co-superviseur.

1.2 STATISTICAL AND EXPERIMENTAL EVALUATION OF LPBF PROCESS PARAMETERS AND HEAT TREATMENTS ON THE MICROSTRUCTURE AND MICROHARDNESS OF 17-4 PH STAINLESS STEEL

Yassmine Chedly[1], Narges Omidi[1]*, Shayan Dehghan[1], Noureddine Barka[1], Abderrazak El Ouafi[1]

[1] Department of Mathematics, Computer Science and Engineering, University of Québec at Rimouski (UQAR), Rimouski, Québec, Canada, G5L 3A1

*Corresponding author: Narges Omidi

1.1.1 Abstract

This study presents a comprehensive experimental evaluation of how Laser powder bed fusion (LPBF) process parameters—laser power, scan speed, hatching spacing, and aging temperature—and post-LPBF heat treatments affect the microstructure, and statistical analysis of the microhardness of 17-4 PH stainless steel. Optical microscopy observations revealed that within a specific volumetric energy density (VED) range of 54.148 to 88.977 J/mm³, manufacturing defects are significantly reduced, with only gas porosities remaining, and lack of fusion (LOF) defects are effectively eliminated. Within this range, microhardness values showed minimal variation, indicating that residual defects had little influence on hardness. Statistical analysis confirmed that aging temperature is the dominant factor, accounting for approximately 96.99% of the variation in microhardness, with higher aging temperatures leading to reduced hardness. A predictive regression model was developed, achieving an error of less than 5%, providing a reliable tool for estimating hardness in LPBF-processed 17-4 PH stainless steel. Overall, the study identifies an optimal VED range of 65.519 to 88.977 J/mm³ for achieving favorable mechanical properties.

Key words: Laser Powder Bed Fusion, 17-4 PH Stainless Steel, Microhardness, Aging treatment, Microstructure.

1.1.2 Introduction

Additive Manufacturing (AM), particularly Laser Powder Bed Fusion (LPBF), has revolutionized the fabrication of complex metal components by enabling geometries unachievable through conventional methods [1],[2],[3]. LPBF offers key advantages, including reduced material waste, high design flexibility, and precise control over internal structures [4]. Among the materials suited for LPBF, 17-4 PH stainless steel—a precipitation-hardened martensitic alloy—stands out due to its exceptional combination of high strength, corrosion resistance, and dimensional stability, primarily attributed to its high chromium content [5],[6]. Its good weldability, along with ferromagnetic properties, makes it particularly effective for manufacturing mechanically and functionally demanding parts with complex geometries [7].

The as-built condition of 17-4 PH stainless steel fabricated via LPBF often presents challenges due to rapid thermal cycling, which induces non-equilibrium microstructures, high residual stresses, and significant anisotropy in mechanical properties [6]. These effects can compromise dimensional stability, reduce mechanical reliability, and lead to variability in performance across the component [8]. Typical defects include pores, lack of fusion, and unmelted regions, as reported by Sabooni et al. [9], all of which diminish structural integrity. Microstructural heterogeneity, as highlighted by Li et al. [10] and Kim et al. [11], further complicates property prediction and quality assurance, while directional dependence in mechanical response—documented by Abe et al. [12] and Laleh et al. [13]—underscores the need for strategies that mitigate anisotropy.

To address the limitations of the as-built microstructure, extensive research has focused on optimizing LPBF process parameters to improve microstructural uniformity, reduce defects, and enhance mechanical performance. Fang et al. [14] reported that a balanced interplay between laser power and scanning speed is essential for minimizing residual stresses while maintaining favorable phase compositions. Hsu et al. [15] demonstrated that increasing energy input promotes the formation of martensite due to thermal stresses, while tighter hatch spacing increases laser overlap, encouraging austenite reversion and leading to a dual-phase microstructure. Sghaier et al. [16] found that LPBF-produced samples exhibit higher microhardness and strength compared to rolled counterparts, attributed to fine martensitic structures formed during rapid solidification, though accompanied by greater porosity and inclusions. Huang et al. [17] systematically quantified the influence of energy density on microstructural evolution, showing a direct correlation between energy input, part density, and microhardness—with peak values of 99.4% density and 441 HV achieved at 200 W laser power and 25 mm/s scanning speed. Yasa et al. [18] explored the effect of layer thickness, concluding that productivity can be improved without significantly compromising density or hardness, provided that scanning parameters are well-controlled. These studies collectively emphasize the critical role of process parameter optimization in tailoring phase composition, minimizing defects, and enhancing the mechanical performance of LPBF-fabricated 17-4 PH components.

Building on the importance of processing parameter optimization, post-processing—particularly heat treatment—plays a critical role in tailoring the final microstructure and mechanical properties of LPBF-fabricated 17-4 PH stainless steel. However, conventional heat treatment protocols, developed for wrought materials, may not be directly applicable to additively manufactured components due to their distinct as-built microstructures, as noted by Facchini et al. [19] and Liu et al. [20]. Several studies have examined the influence of post-treatment parameters on microhardness and phase evolution. Sabooni et al. [21] demonstrated that aging at 480 °C significantly increased microhardness, reaching a peak of 477 ± 16.8 HV after 5 h due to the formation of nanoscale ε-Cu-rich precipitates that hinder dislocation motion via the Orowan mechanism. However, extended aging (15 h) led to precipitate coarsening and the formation of reversed austenite, reducing hardness to 451 ± 21 HV while enhancing ductility through transformation-induced plasticity mechanisms.

Kovacs et al. [22] found that a combination of solution annealing at 1038 °C and aging at 480 °C (H900 condition) optimized hardness, achieving a peak value of 445 HV. Similarly, Huang et al. [23] investigated standard aging conditions (H900, H1025, H1150), observing that H900 yielded the highest strength due to Cu-rich precipitation, which shifted from shearing to Orowan bypass with increasing aging temperature. Expanding the scope to 15-5 PH stainless steel, Mansoura et al. [24] identified aging temperature as the most influential factor in enhancing microhardness, with the highest value (46.5 HRC) achieved at 500 °C for 1 h due to fine, uniformly distributed Cu precipitates. Negron et al. [25] reported that solution annealing at 1038 °C for 3 h followed by aging at 482 °C for 1.5 h improved microhardness to approximately 454 HV through uniform precipitation. However, prolonged annealing increased porosity, underscoring the need for optimized heat treatment durations to balance mechanical performance and structural integrity in LPBF components.

The heat treatment of 17-4 PH stainless steel is well standardized in conventional metallurgy, as outlined in ASTM A564-13, where solution annealing followed by aging is critical for achieving optimal mechanical properties. These treatments promote the precipitation of fine copper-rich phases that enhance hardness and strength, with maximum hardness typically attained at moderate aging conditions such as 480 °C for one hour. At elevated temperatures, however, austenite reversion along martensite lath boundaries leads to softening and reduced mechanical performance due to precipitate coarsening and phase transformation dynamics [26], [27], [28], [29]. While these mechanisms are well established for wrought or conventionally processed alloys, they may not directly translate to components produced by LPBF. The layer-by-layer nature of LPBF induces unique microstructures, residual stress profiles, and thermal histories, which significantly influence phase stability, precipitation behavior, and ultimately mechanical performance. As a result, LPBF-fabricated 17-4 PH stainless steel requires tailored post-processing strategies that consider the specific process-induced microstructural features to achieve desired mechanical properties—particularly microhardness. Current gaps remain in understanding how these tailored heat treatments should be optimized in relation to specific LPBF parameters.

Recent efforts, such as the study by Aripin et al. [30],[31] , have begun addressing the combined influence of build orientation and heat treatment on LPBF-processed 17-4 PH stainless steel. Their work demonstrated that the microstructure, particularly the martensite-to-austenite phase balance, is highly sensitive to the thermal history imposed by varying build orientations and post-processing treatments. Specifically, they observed that a 0° build orientation coupled with H750 heat treatment maximized the martensite content and preserved melt pool boundaries, resulting in superior mechanical properties, including a hardness increase from 27.2 HRC to 39.5 HRC. Conversely, higher heat treatment temperatures such as H1100 promoted microstructural homogenization and grain growth, reducing yield strength despite increased hardness. Consequently, a gap remains in understanding how microstructure-sensitive properties like microhardness are influenced by the interplay of LPBF parameters and heat treatment conditions. This study aims to address that gap through a focused sensitivity analysis.

This study addresses the need for tailored heat treatment strategies for LPBF-fabricated 17-4 PH stainless steel through a comprehensive sensitivity analysis focused on microhardness. The novelty of this work lies in its systematic evaluation of the effects of LPBF process parameters—laser power, scanning speed, and hatch spacing—along with aging temperature, on microhardness. In prior research, the authors have demonstrated that while tensile strength and yield strength are primarily governed by microstructural features, and elongation is more sensitive to manufacturing defects—particularly lack of fusion—microhardness is uniquely influenced by both [32], [33]. As such, microhardness serves as a balanced indicator of both microstructural integrity and defect sensitivity. To quantify the impact of each processing variable, statistical analysis using ANOVA was applied to microhardness data, enabling a detailed understanding of parameter sensitivity. Furthermore, a predictive linear regression model was developed to estimate microhardness across varied processing conditions. This integrated approach offers valuable insights for optimizing LPBF and heat treatment parameters to achieve targeted mechanical performance in 17-4 PH components.

1.1.3 Material and methods

This study employed 17-4 PH stainless steel powder supplied by EOS, specifically developed for LPBF applications. The powder exhibited a spherical morphology with particle sizes ranging from 10 to 45 µm, as shown in Figure 1.1-(a). Figure 1.1-(b) displays the surface morphology of a representative particle, and Figure 1.1-(c) presents the EDS elemental analysis of the powder surface, confirming the presence of the expected alloying elements and the absence of detectable oxygen. The identified elements are consistent with the nominal chemical composition provided by the supplier, as listed in Table 1.1.

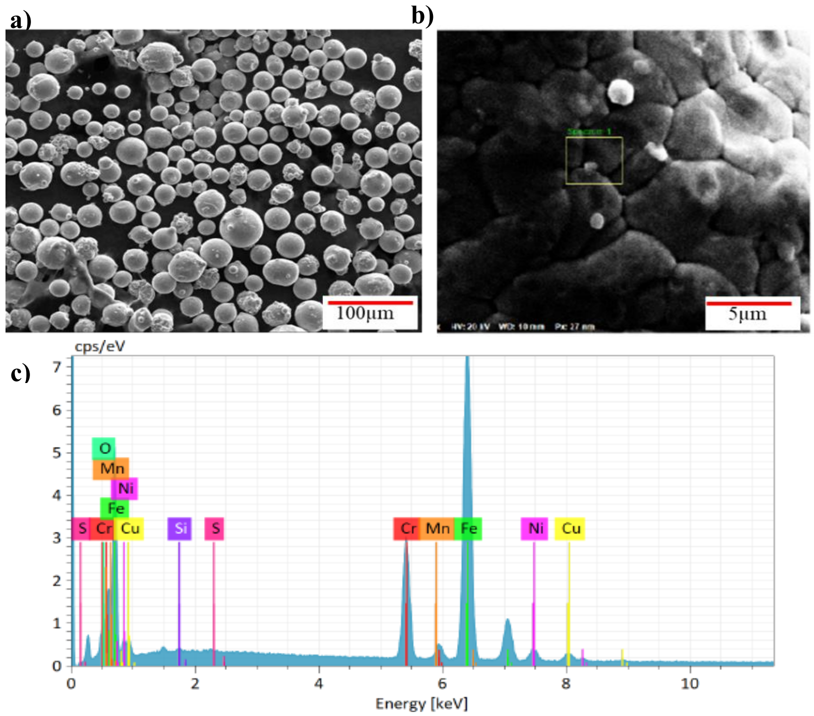

Figure 1.1: a) SEM image of the 17-4 PH stainless steel powder, b) SEM image of the powder at higher magnification, focusing on particle surface morphology, and c) EDS analysis of the powder composition.

Table 1.1: Chemical composition of EOS 17-4 PH Stainless Steel powder.

Element	**Fe**	**C**	**Mn**	**P**	**S**	**Si**	**Cr**	**Ni**	**Cu**	**Nb, Ta**
Volume (wt. %)	Bal.	0.07 max	1.0 max	0.04 max	0.03 max	1.0 max	15.0-17.5	3.0-5.0	3.0-5.0	0.15-0.45

In this study, 17-4 PH stainless steel components were fabricated using an EOS M290 machine with a build volume of 250 × 250 × 325 mm³ and a maximum laser power of 400 W. An inert argon atmosphere was maintained at a controlled pressure and a flow rate of approximately 0.6 m³/h to prevent oxidation during fabrication. The build plate temperature was set at 65 °C to reduce thermal shock during processing. The selected parameter levels are presented in Table 1.2. Each parameter—laser power, scan speed, and hatch distance—was varied at three levels, approximately ±10% from the manufacturer's recommended settings, to remain within a processing window associated with minimal defects. The layer thickness was maintained at 40 μm for all builds.

Table 1.2: Process parameters levels.

Parameter	Level 1	Level 2 (recommended)	Level 3
Laser Power (W)	198	220	242
Scan Speed (mm/s)	679.95	755.5	831.05
Hatch Distance (µm)	90	100	110

After manufacturing, the samples underwent heat treatments as outlined in Table 1.3. Immediately after the LPBF process, all samples—still attached to the build plate—were stress-relieved at 650 °C for one hour, followed by slow furnace cooling to reduce residual stresses. This treatment was chosen based on prior studies, as it effectively reduces residual stresses without inducing significant austenite reversion or precipitate evolution [34]. Following stress relief, the samples were removed from the build plate and solution-annealed at 1040 °C for 30 minutes, then air cooled. These parameters are based on the material supplier's recommendations. This step aimed to dissolve existing precipitates and homogenize the microstructure. The solution-annealed specimens were then divided into three groups for aging treatments at 480 °C (H900), 565 °C (H1025), and 620 °C (H1150), each held for one hour followed by air cooling. These aging temperatures were selected based on literature findings that associate 480 °C with peak hardness due to coherent copper precipitates, and higher temperatures (565 °C and 620 °C) with over-aging conditions where precipitate coarsening and retained austenite formation reduce hardness and strength but enhance ductility [35]. The heat treatment conditions are detailed in Table 1.3.

Table 1.3: Heat treatment process for 17-4 PH stainless steel.

Heat treatment	Temperature (°C)	Duration
Stress relieving	650°C	1h, followed by slow cooling
Solution annealing	1040°C	30 min, followed by air cooling
Aging	480°C/565°C/620°C	1h, followed by air cooling

The experimental design for this study was constructed using a Taguchi orthogonal array, based on the three levels of process parameters presented in Table 1.2, along with the selected aging temperatures in Table 1.3. The complete combination of these parameters is shown in Table 1.4. This design was developed to enable the use of ANOVA and regression analysis in the subsequent statistical evaluation, allowing for the identification of the most influential factors affecting microhardness, while minimizing the number of experimental trials. The volumetric energy density (VED) values presented in Table 1.4, were calculated using Eq.1, where P is the laser power (W), V is the scanning speed (mm/s), LT is the layer thickness (μm), and HD is the hatch distance (μm). VED serves as a useful indicator of the overall energy input during the LPBF process and is referenced in the discussion of microstructural features and manufacturing defects. For general trends, processing conditions are discussed in terms of VED. However, in the statistical analysis, the individual parameter values are analyzed in detail to determine their specific contributions to the microhardness behavior.

$$VED = \frac{P}{V*LT*HD} \qquad \text{Eq.1 [36].}$$

Table 1.4: Design of experiments.

	Laser power P (w)	**Scan speed V (mm/s)**	**Hatch distance HD (μm)**	**VED (J/mm3)**	**Aging temperature T (°C)**
S1	198	679.95	90	80.888	480
S2	198	755.5	100	65.519	565
S3	198	831.05	110	54.148	620
S4	220	679.95	100	80.888	620
S5	220	755.5	110	66.181	480
S6	220	831.05	90	73.535	565
S7	242	679.95	110	80.888	565
S8	242	755.5	90	88.977	620
S9	242	831.05	100	72.799	480

For microstructural observation and microhardness testing, samples were sectioned along the build direction, mounted, and polished following ASTM E3-11 standards. Polishing was performed from coarse 9 μm grits down to a final 0.05 μm finish. Chemical etching was conducted using Fry's reagent for one minute in accordance with ASTM E407-07. Microstructural characterization was conducted using optical microscopy and the SEC SNE-4500M scanning electron microscope (SEM), equipped with a Bruker Esprit EDS sensor. Microhardness was measured using a Clemex ST-2000 Vickers hardness tester, following ASTM E384-17. A total of 16 indentations were made per sample using a 300 gf load for 10 s. The indents were done in a 4×4 rectangular grid with 1000 μm spacing between each point, covering both longitudinal and transverse directions within a cross-sectional plane parallel to the build direction. The average microhardness value (HRC) was calculated from these 16 measurements to ensure representative assessment across a broad sampling area.

X-ray Diffraction (XRD) analysis was performed on three representative samples aged at different temperatures to identify phase constituents and detect crystallographic changes due to processing.

Finally, regression analysis was used to model the relationship between process parameters and microhardness. ANOVA was applied to evaluate the statistical significance of each parameter—laser power, scan speed, hatch distance, and aging temperature—by comparing mean S/N ratios and sample group means. The linear regression model quantified how microhardness varies with each unit change in process parameters. The general regression equation is provided in Eq. 2.

$$y = \beta_0 + \beta_1 X_1 + \beta_2 X_2 + \cdots + \beta_n X_n + \epsilon \qquad \text{Eq.2 [37].}$$

Where:

- y: is the response variable (microhardness in this case).
- $X_1, X_2, \ldots, X_n$: are the independent variables (laser power, scan speed, hatch distance, aging temperature).
- β_0 is the intercept, representing the expected value of y when all X_i are zero.
- $\beta_1, \beta_2, \ldots, \beta_n$ are the regression coefficients representing the change in the response for each unit change in the respective X.
- ϵ is the error term.

1.1.4 Results and discussion

1.1.4.1 Microstructural analysis

The as-built microstructure of 17-4 PH stainless steel is anticipated to have martensite (α') and retained austenite (γ), with BCC peaks signifying that the predominant phases are martensitic and ferritic, exhibiting a columnar structure oriented along the build direction. The fast heating and cooling rates (10^3 C/s to 10^5 C/s) indicative of the LPBF process limit the full development of austenite, resulting in the persistence of delta ferrite. Retained austenite is further stabilized by nickel enrichment at grain boundaries, which obstructs martensite development. Precipitates, including Nb-Cr intermetallic phases, Nb-Cr carbides, and possible Cu-rich particles, are also reported along dendrite boundaries. Additionally, MnS inclusions are observed at much lower concentrations than in wrought samples, likely due to the high cooling rates that limit nucleation time [38], [39].

Following the as-built condition, the microstructure of LPBF-manufactured 17-4 PH stainless steel undergoes significant evolution during heat treatment, as established in the literature. Stress relief at 650 °C for one hour reduces retained austenite from 38.7–50% to about 15–20%, producing a mainly martensitic structure while maintaining the dendritic/cellular morphology and micro segregation [38], [40]. However, this treatment does not fully homogenize the microstructure or dissolve all precipitates [38]. Subsequent solution annealing at 1040 °C transforms BCT martensite back to FCC austenite, relieves residual stresses, and promotes recrystallization, reducing retained austenite to below 5%. Aging then induces precipitation of Cu-rich particles within the martensitic matrix—initially coherent BCC phases that enhance hardness. At higher aging temperatures, these precipitates coarsen and may become non-coherent FCC structures, while some reversed austenite may form due to Ni segregation [40]. The resulting structure comprises martensite, Cu-rich precipitates, and minor reversed austenite.

The optical micrographs of all samples after aging at temperatures H900, H1025, and H1150 are shown in Figure 1.2. After solution treatment at 1040°C, the microstructure consists primarily of martensite laths with a high dislocation density. Predominant in all conditions, the martensitic structure demonstrates a coarse network in H900 with clear, well-defined boundaries, indicative of minimal thermal diffusion (Figure 1.2-(a), Figure 1.2-(e) and Figure 1.2-(i)). As the aging temperature increases, as shown in Figure 1.2-(b), Figure 1.2-(d) and Figure 1.2-(g), the martensitic boundaries become less distinct, suggesting partial reversion to austenite or relaxation of the martensitic structure, which is less apparent in H900 [41]. The presence of more austenite in these conditions correlates with increased ductility and reduced hardness, as the austenite phase generally exhibits higher toughness, but lower yield strength compared to martensite.

Aging treatments cause the precipitation of coherent copper-rich phases that begin to form at temperatures as low as 400°C. At the H900 condition, copper precipitates are small (15-25 nm), fine, evenly distributed and maintain coherency with the matrix, yielding the highest hardness due to effective dislocation pinning [42]. In contrast, at higher temperatures such as H1025 in Figure 1.2-(b), (f) and (g); and H1150 in Figure 1.2-(c), (d) and (h), over-aging causes the coarsening of precipitates, grow larger and become more incoherent with the matrix, as evidenced by the irregular shapes and less uniform distribution [35].

The precipitation behaviour of 17-4 PH stainless steel under the H900, H1025, and H1150 conditions reflects a temperature-dependent evolution of microstructure that can be effectively analysed using the Johnson-Mehl-Avrami-Kolmogorov (JMAK) model [43], [44]. At H900 (~482°C), precipitation of fine, coherent copper-rich particles in the martensitic matrix, containing almost all the copper content (~3.4 wt%), has been observed [45], [46]. In this condition, spherical zones (originally with a bcc structure and becoming an FCC phase by growth) nucleate and grow with an average diameter of ~150 Å; consequently, maximum hardness arises after efficient dislocation pinning [47]. This can be quantitatively interpreted within the frame of transformation kinetics by the JMAK model, expressed as $X(t)=1-\exp(-k\cdot tn)$, where $X(t)$ is the fraction of precipitated material at time t, k is the rate constant, and n is the Avrami exponent that reflects nucleation and growth mechanisms [43], [44]. At H1025 (~552°C), the coarsening of copper precipitates initiates with a partial loss of coherency, while reversed austenite begins to develop at lath borders, influenced by copper enrichment and diffusional mechanisms. At H1150 (~621°C), substantial austenite development occurs, characterized by continuous interlath layers and blocky intralath regions, which markedly decrease hardness due to over-aging. The fact that these observations are further supported by the JMAK model, where higher temperatures produce slower nucleation rates and longer growth times, moving the microstructure to coarser, less coherent precipitates. Additionally, NbC carbides contribute to microstructural stability, particularly at elevated temperatures. The interplay between these phases demonstrates the critical influence of aging temperature on precipitation kinetics and mechanical properties, consistent with findings in the reference [48].

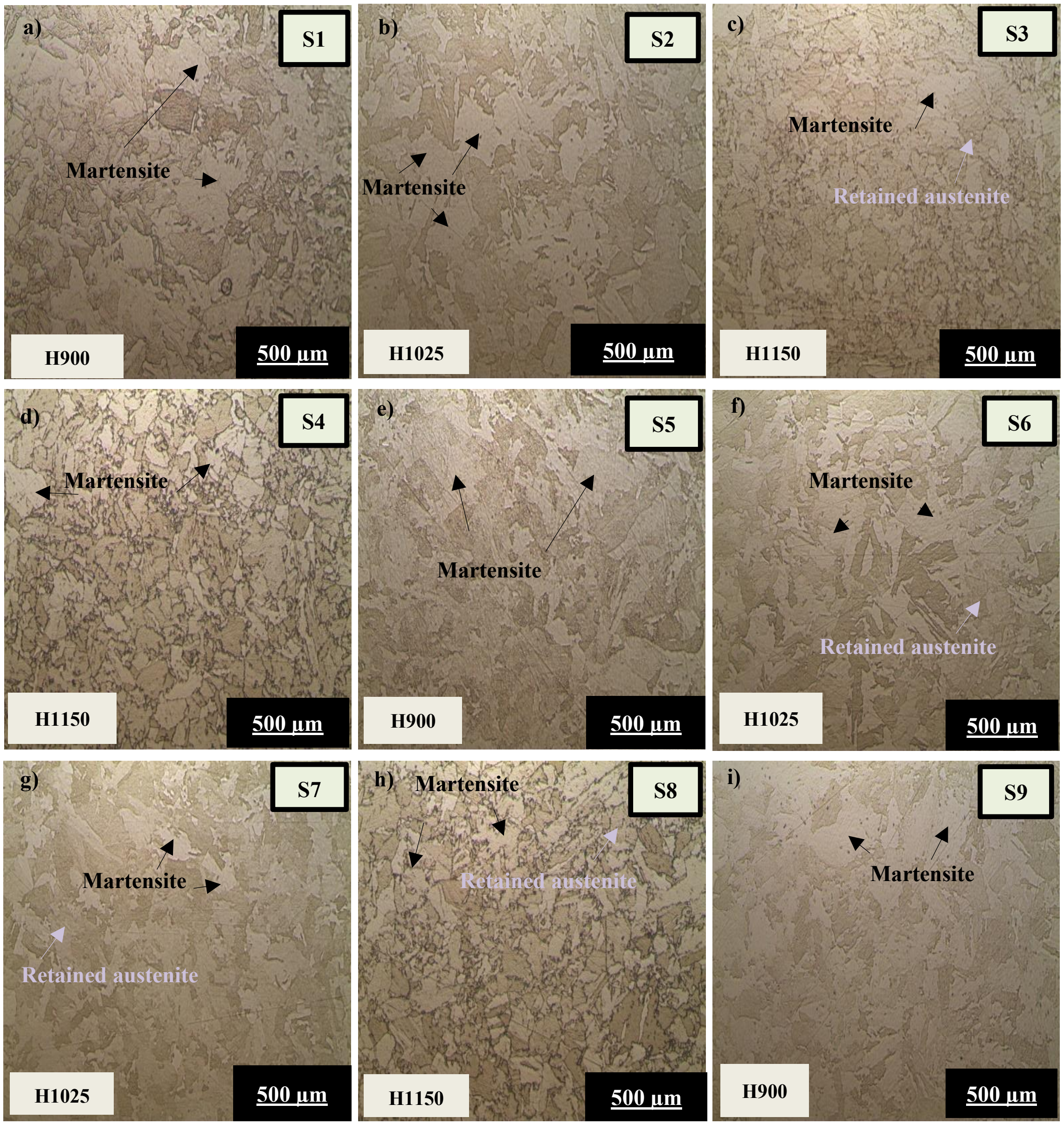

Figure 1.2: Optical micrographs of etched 17-4 PH stainless steel samples at 500 µm magnification, at different aging conditions a), e) and i) : H900; b), f) and g) : H1025; c), d) and h) : H1150.

Figure 1.3 presents SEM micrographs and EDS elemental mappings of sample S1 at multiple magnifications, illustrating the microstructural and compositional features of the 17-4 PH stainless steel. In Figure 1.3-(a) and -(b), the martensitic matrix is clearly discernible, with finer details revealed at higher magnification. Distinct features have been annotated as

NbC carbides and Cu-rich precipitates. While direct identification of NbC through SEM is challenging due to their nanoscale dimensions, the morphology and distribution observed are consistent with prior reports, and their identification is supported through literature references [49]. Thus, we have opted to retain these annotations with appropriate citation.

The EDS mapping in Figure 1.3-(c) confirms the spatial distribution of key alloying elements—carbon (C), chromium (Cr), iron (Fe), nickel (Ni), and copper (Cu). The Cu-rich regions identified in the SEM images correspond to local enrichments in the copper EDS signal, supporting their classification as Cu-rich precipitates. These precipitates are known to form during aging and play a significant role in enhancing hardness via precipitation strengthening.

Chromium appears to be uniformly distributed, reinforcing its role in martensitic phase stabilization and corrosion resistance. Likewise, the observed nickel distribution near grain boundaries is indicative of its function in stabilizing retained austenite. Overall, this combined microstructural and compositional analysis highlights the interactions among precipitates and the matrix, which collectively govern the mechanical behavior of the alloy [50].

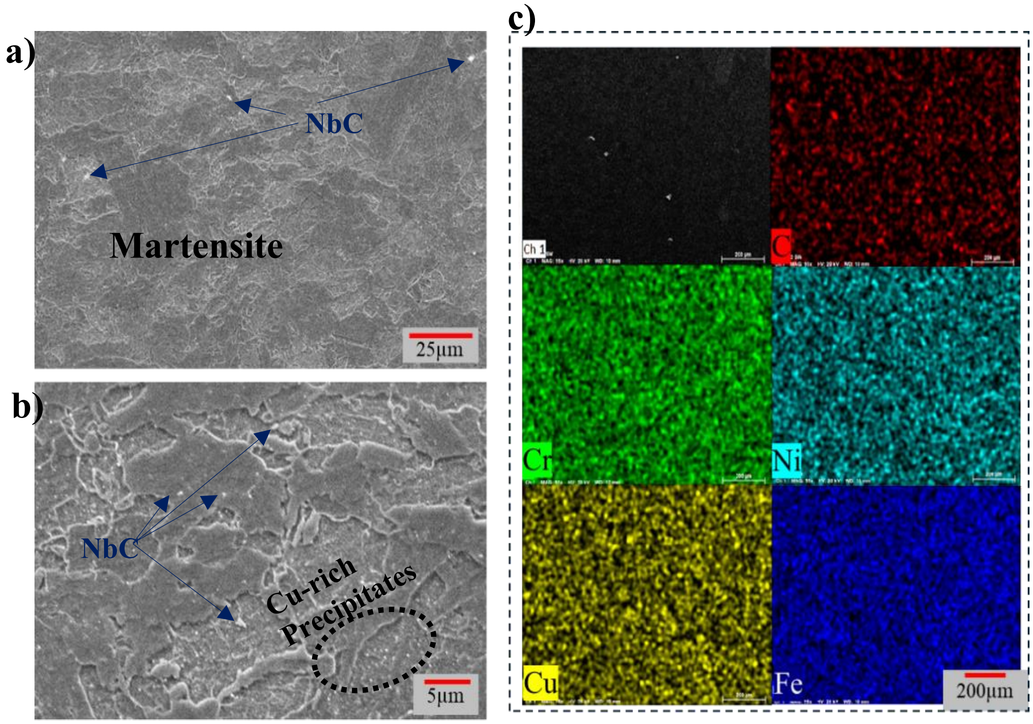

Figure 1.3: SEM micrographs of sample S1 at different magnifications: (a) at 10 µm, (b) at 20 µm, (c) at 50 µm, and (d) EDS elemental mapping at 200 µm showing the distribution of key elements (C, Cr, Fe, Ni, Cu).

To further validate the microstructural evolution discussed above, XRD analysis was conducted to quantify crystallographic phases, residual stresses, and crystallite sizes across selected samples. Figure 1.4-(a) and Figure 1.4-(b) illustrates the XRD patterns of sample S1, sample S3, and sample S6 aged at 480 °C, 565 °C, and 620 °C, respectively. The XRD patterns revealed that as expected, the alloy predominantly consisted of a martensite phase with a preferred orientation of the (011) plane is observed in all samples. No austenite phase is detected in the XRD patterns of the samples probably due to the very small volume fraction. Alternatively, the absence of the austenite phase in the XRD patterns of the samples can be attributed to the aging treatment process and the transformation of the remaining austenite to martensite during LPBF [51]. In sample 1, the peak corresponding to the (011) plane has shifted to higher angles. Generally, the shift of peaks to higher 2θ values indicates residual stress in the structure, enhancing the material's fatigue and crack initiation resistance [52]. Therefore, the residual stress in sample 1 is probably higher.

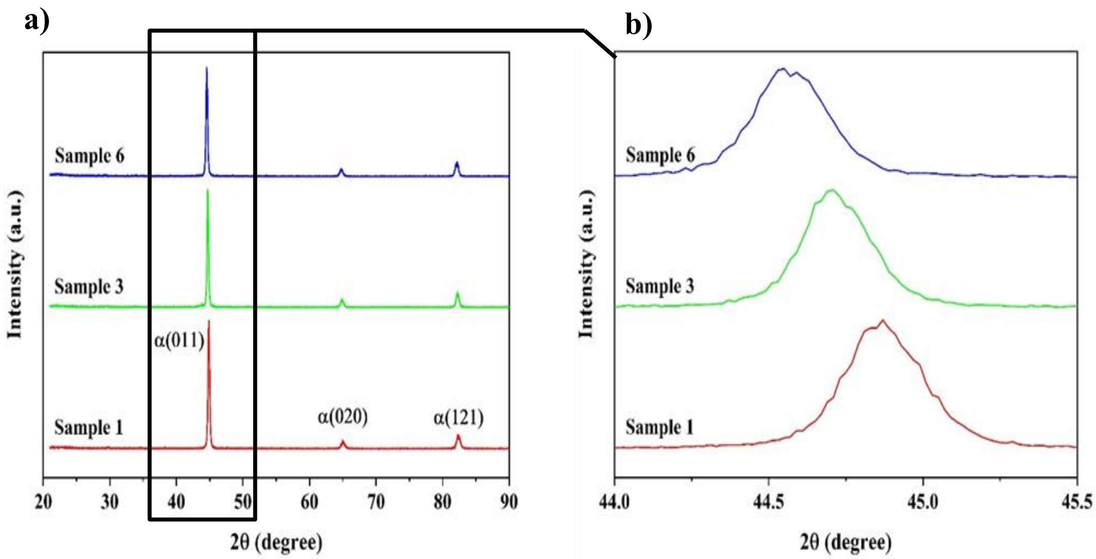

Figure 1.4: a) XRD spectra of samples 1, 3, and 6, b) at 45 (degree).

The size of the crystalline particles in a sample were calculated using Debye-Scherrer equation (The Eq.3). Where, D_{nm} represents the average size of the crystalline domains (nm), K is the shape factor, typically about 0.9, λ is the wavelength of the X-ray used in the diffraction experiment (1.54 Å), β is the full width at half maximum (FWHM) of the peak in radians and θ is the Bragg angle.

$$D_{nm} = \frac{K\lambda}{\beta \cos\theta} \qquad \text{Eq.3}$$

Also, the microstrain (ε_{strain}) of the samples has been calculated using Eq.4 to evaluate internal stresses and deformations within the crystalline structure by analyzing the peak broadening.

$$\varepsilon_{strain} = \frac{\beta}{4\tan\theta} \qquad \text{Eq.4}$$

Table 1.5 presents the crystallite size and lattice strain, extracted from XRD results. These values were calculated to assess the influence of microstructural refinement and internal stresses on the mechanical behavior of the LPBF-fabricated samples. The crystallite size and lattice strain are critical factors that influence the mechanical properties of LPBF-fabricated materials. However, this can also lead to higher residual stresses, reflected in the lattice strain values. Sample 3, with the largest crystallite size and lowest lattice strain, likely possesses a balance of good tensile strength and reduced brittleness, making it potentially more ductile. Samples 1 and 6, with smaller crystallite sizes, may exhibit higher tensile strength but also higher residual stresses, which could affect their overall toughness and ductility.

Table 1.5: The structural parameters of the samples obtained from XRD analysis.

Sample	**2θ (101)**	**FWHM β (Radian)**	**Crystallite size D (nm)**	**Lattice strain ε (%)**
1	44.835	4.3×10^{-3}	35.1	0.267
3	44.681	3.5×10^{-3}	42.7	0.222
6	44.532	4.1×10^{-3}	36.4	0.26

Residual stress σ derived from lattice strain through Hooke's Law for isotropic materials, which correlates stress and strain via the material's Young's modulus, E, and Poisson's ratio ν :

$$\sigma = \frac{E}{1+\nu}\varepsilon \qquad \text{Eq.5}$$

Assuming the following typical values for 17-4 PH stainless steel:

Young's modulus, E = 200 GPa, Poisson's ratio, ν = 0.3

The residual stresses for the samples were approximated as follows:

$$\sigma_{(sample\ 1)} \approx 410\ MPa, \qquad \sigma_{(sample\ 3)} \approx 341.5\ MPa, \qquad \sigma_{(sample)\ 6} \approx 400\ MPa$$

1.1.4.2 Manufacturing defects and porosity

Regarding the effect of processing parameters, the LPBF-processed 17-4 PH stainless steel exhibited two primary types of porosity: lack of fusion (LOF) and gas porosities, as shown in Figure 1.5. Optical microscopy images of LOF defects are presented in Figure 1.5-(a) and Figure 1.5-(b). These porosities typically result from insufficient overlap between successive layers or tracks, or from inadequate energy input, which prevents complete melting of powder particles. This leads to unmolten or partially melted regions and weak interlayer bonding. LOF defects are known to significantly degrade mechanical properties. Figure 1.5-(c) illustrates gas porosity, characterized by spherical voids formed due to gas entrapment during melting and solidification. The origin of these gases may include the decomposition of powder impurities, residual gases in the powder bed, or insufficient control of the ambient atmosphere. These gas-induced voids increase the total porosity and may compromise the overall performance of the material.

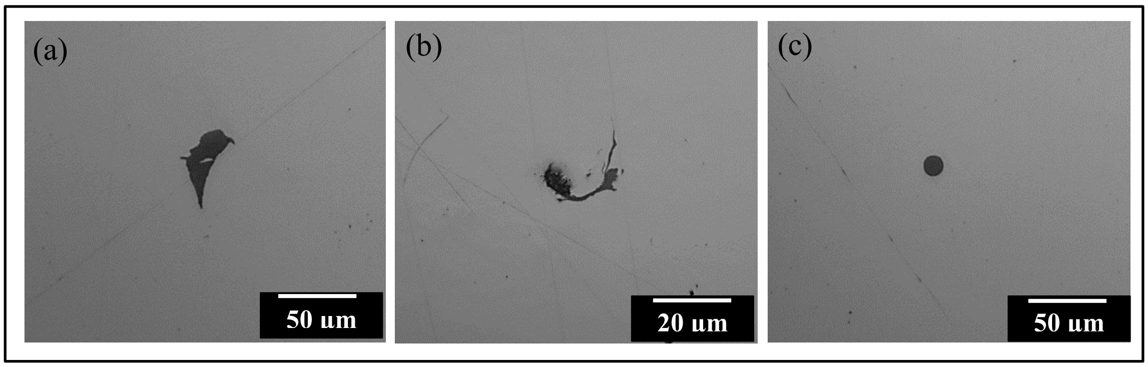

Figure 1.5: Optical microscopy image of manufacturing defects in additively manufactured specimens including: (a) and (b) LOF, (c) spherical gas porosity.

Notably, with a high VED range of 54 to 89 J/mm³, the manufacturing defects arising from the processing parameters were very low, resulting in materials that were nearly fully dense. Manufacturing defects, such as LOF, could barely be found. They were mostly evident in sample S2 and sample S3, which had the minimum VED of 54 and 65.5 J/mm³ respectively. Notably, within the same heat temperature range, the porosity size reduces with decreasing hatching space. Figure 1.6 shows the porosity evolution of the material at different processing parameters at a temperature of 620°C. Figure 1.6-(a) to Figure 1.6-(c) shows the optical microscopy images of the porosity reduction with the reduction in hatching space from 110 to 90 µm. It can be concluded that a higher hatching space leads to a greater possibility of manufacturing defects and entrapped gases in the material. When exposed to high temperatures, these defects and gases have a higher likelihood of growing due to thermal expansion and diffusion mechanisms. This expansion increases the internal pressure within the pores, causing them to enlarge.

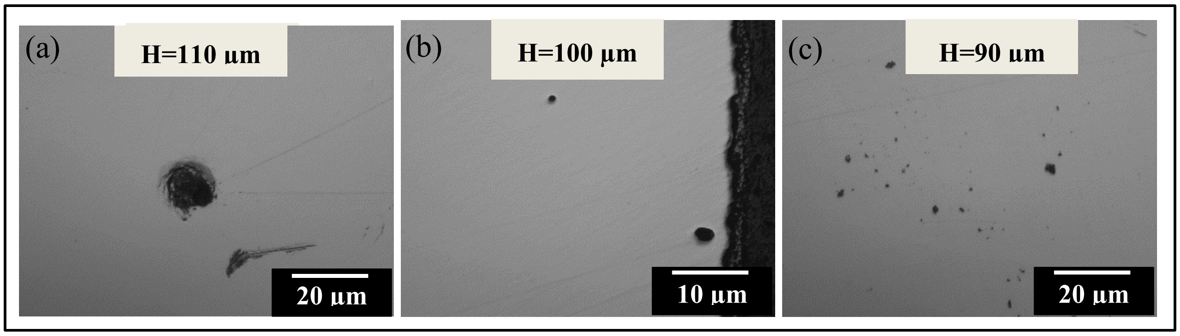

Figure 1.6: Effect of hatching space on porosity size: (a)-(c) Optical microscopy images with hatching space of 110, 100, and 90 µm, respectively at the same heat treatment condition, illustrating the reduction in porosity size with decreasing hatching space.

1.1.4.3 Microhardness

Figure 1.7 presents the average microhardness results across all samples, highlighting the effects of aging temperature, VED, and relative density. In Figure 1.7-(a), the hardness values range from 32.68 to 44.52 HRC. The highest value is observed in sample S1, aged at 480 °C, while the lowest occurs in sample S4, aged at 620 °C. As shown in Figure 1.7-(b), there is a clear inverse relationship between aging temperature and hardness: lower aging temperatures result in higher hardness. Aging temperature was identified as the most influential parameter among those studied.

This trend is attributed to the precipitation hardening mechanism in 17-4 PH. At 480 °C, fine Cu-rich precipitates form, enhancing hardness. At 620 °C, precipitate coarsening and grain growth lead to over-tempering and a reduction in hardness [53]. The intermediate condition at 565 °C achieves a balanced hardness due to a favorable compromise between precipitation strengthening and limited grain growth.

Figure 1.7-(c) shows the relationship between VED and hardness. Although the effect is less pronounced than that of aging temperature, higher VED generally leads to slightly higher hardness, especially for samples aged at 480 °C. One contributing factor is that higher VED reduces manufacturing defects such as lack of fusion and gas porosity, which can locally decrease hardness due to incomplete bonding or voids. Therefore, samples processed at higher VED tend to exhibit more uniform and slightly elevated microhardness

values. In the case of sample S1, the higher microhardness is attributed to its fine martensitic grain structure and the presence of evenly distributed, coherent Cu-rich precipitates, as observed in Figure 1.2-(a) and Figure 1.3-(a). Additionally, the minimal porosity seen in this sample further supports the uniformity of its hardness distribution. Nonetheless, samples S5 and S9, also aged at 480 °C but processed at lower VEDs of 66.18 and 72.80 J/mm^3, showed comparable hardness to S1. This confirms that while VED has some influence, aging temperature remains the dominant factor.

Figure 1.7-(d) illustrates the effect of relative density on hardness. A distinct correlation is observed up to ~98% density, beyond which further increases have minimal impact. At high relative densities, the contribution of internal defects to hardness diminishes, and the dominant influence shifts to heat treatment. The role of relative density becomes more critical in the presence of large porosities, which can act as crack initiation sites and reduce local hardness. However, once porosity is sufficiently minimized, hardness is primarily governed by microstructural evolution during aging.

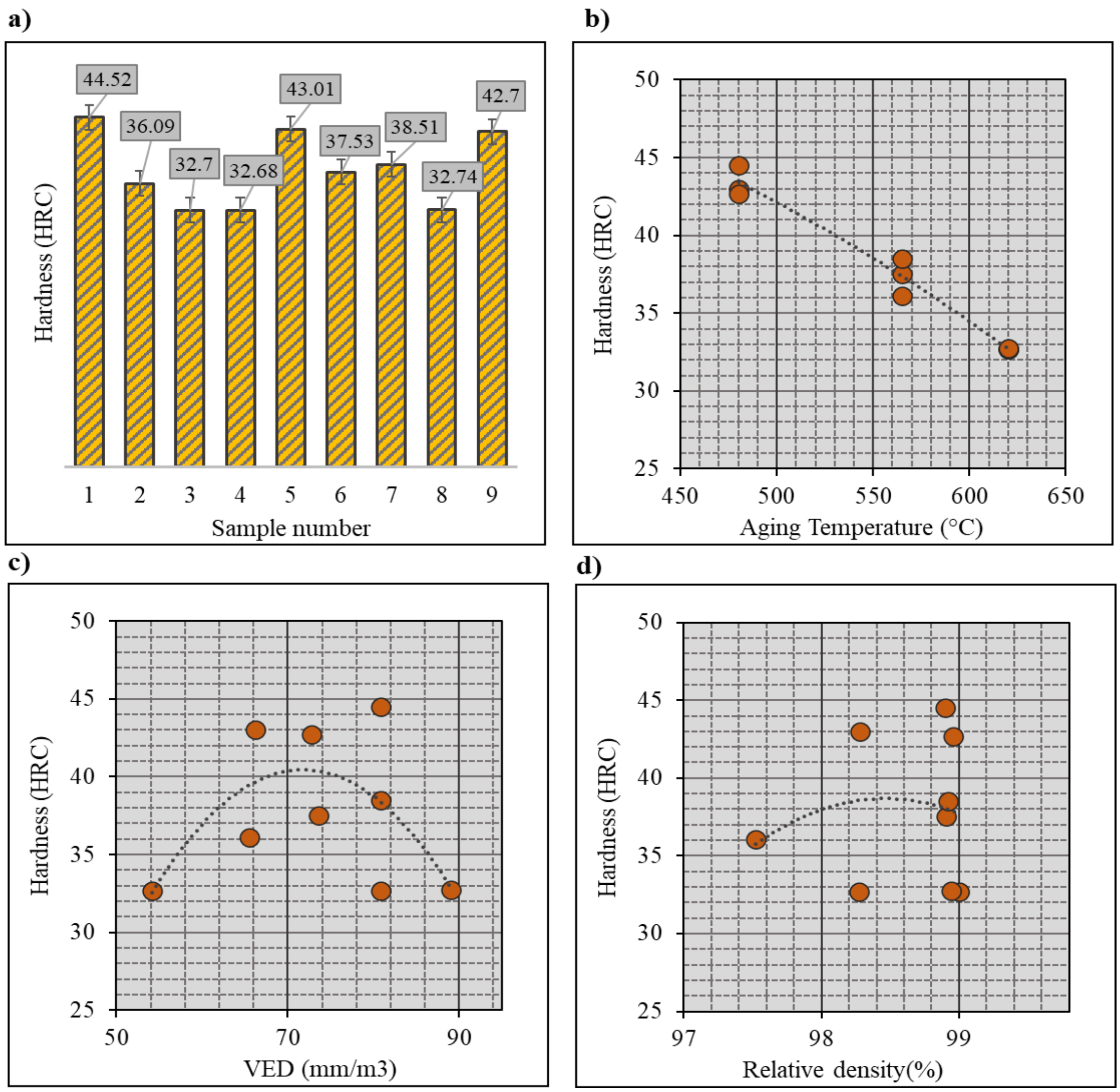

Figure 1.7: (a) Microhardness Histogram, (b) Microhardness VS Aging Temperature curve, (c) Microhardness VS VED curve, and (d) Microhardness VS Relative density curve.

Figure 1.8 illustrates the effect of aging temperature on microhardness through profiles measured across samples aged at 480 °C, 565 °C, and 620 °C. The highest values were recorded at 480 °C, attributed to the formation of finely dispersed Cu-rich precipitates that hinder dislocation motion. At 565 °C, hardness was slightly lower yet stable, indicating a balanced microstructure with moderate precipitate growth. However, a localized increase in microhardness is observed between 150–250 μm at this temperature. This sharp rise is most likely due to the presence of a higher density of fine, partially coherent Cu-rich precipitates in this region, which enhances dislocation pinning. Such morphology may result from localized variation in thermal history or phase transformation kinetics, leading to temporarily optimized precipitation conditions. In contrast, samples aged at 620 °C showed the lowest hardness, consistent with over-tempering and reduced dislocation density due to precipitate coarsening [54].

The very small variation in microhardness across the samples and the absence of abrupt local drops indicate that manufacturing defects such as pores or lack of fusion were not severe enough to influence the hardness distribution. Furthermore, the consistency of these maps suggests that elemental evaporation, particularly of volatile elements like carbon, did not occur to a degree that would induce significant microstructural inhomogeneity. These observations align with the mechanical property trends, where the mechanical response was primarily governed by the aging temperature rather than the slight variations in processing parameters. Overall, aging temperature had the dominant effect on hardness. VED contributed secondarily, particularly under optimal aging, while relative density had minimal influence once high densification was reached.

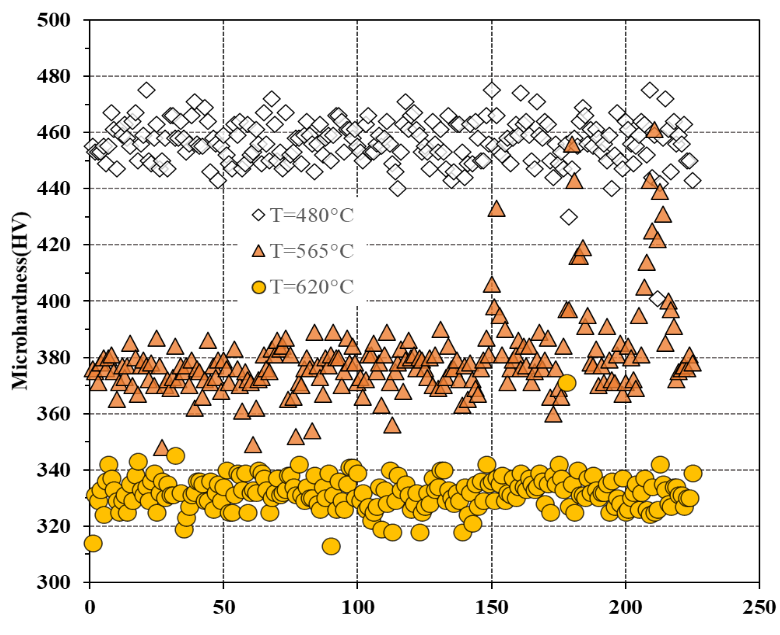

Figure 1.8: Microhardness map of 17-4 PH at different heat treatment temperatures.

1.1.4.4 Statistical analysis of Microhardness

According to the ANOVA results in Table 1.6, aging temperature had the most significant effect on microhardness, contributing 96.99% of the total variation, with a strong negative coefficient of –0.7377 ($p = 0.000$). A significance level of $p < 0.05$ was used to determine statistical relevance. The decrease in hardness with increasing aging temperature is attributed to precipitate coarsening and grain growth, which lower dislocation resistance—consistent with prior findings on material softening at elevated aging conditions.

Scan speed accounted for 0.91% of the variation (coefficient: –0.0666, $p = 0.005$), indicating that higher speeds reduce energy input and can lead to incomplete melting and reduced hardness. In contrast, hatch distance contributed only 0.06%, with no statistical significance ($p = 0.414$). This minimal impact is likely due to its limited influence on laser overlap and fusion quality in the tested range.

As summarized in Table 1.7, the model shows a high adjusted R^2 of 97.59%, and a predicted R^2 of 96.98%, confirming that the selected LPBF parameters—especially aging temperature—reliably explain the variation in microhardness. The strong agreement between actual and predicted values validates the model's accuracy and applicability.

Table 1.6: Regression Analysis for Microhardness.

Source	**DF**	**Seq SS**	**Contribution**	**Adj SS**	**Adj MS**	**F-Value**	**P-Value**
Regression	4	49223.9	97.96%	49223.9	12306.0	264.18	0.000
Laser power	1	0.3	0.00%	0.3	0.3	0.01	0.932
Scan speed	1	455.7	0.91%	455.7	455.7	9.78	0.005
Hatch distance	1	32.4	0.06%	32.4	32.4	0.69	0.414
Aging temperature	1	48735.4	96.99%	48735.4	48735.4	1046.24	0.000
Error	22	1024.8	2.04%	1024.8	46.6		
Lack-of-Fit	4	981.0	1.95%	981.0	245.3	100.82	0.000
Pure Error	18	43.8	0.09%	43.8	2.4		
Total	26	50248.7	100.00%				

Table 1.7: Model summary for Microhardness.

Model	S	R^2	Adj R^2	Press	Predicted R^2	AICc	BIC
Microhardness	6.82505	97.96%	97.59%	1516.32	96.98%	191.01	194.58

Figure 1.9 shows the main effects of laser power, scan speed, hatch distance, and aging temperature on microhardness. The plots confirm that aging temperature had the most significant influence, as seen by the sharp decline in microhardness with increasing temperature (Figure 1.9-(d)). This trend aligns with the experimental results discussed earlier and reinforces the findings from the ANOVA analysis. In comparison, laser power, scan speed, and hatch distance (Figure 1.9-(a) to (c)) show relatively minor effects. Laser power presents a nearly constant trend, while scan speed and hatch distance have slight variations in hardness, consistent with their low contribution percentages observed in the statistical model. These results validate the earlier conclusion that aging temperature is the primary factor controlling microhardness in LPBF-processed 17-4 PH stainless steel. It could be concluded, among the processing parameters, slightly higher laser power (~242 W), lower scan speed (~679.95 mm/s), and narrower hatching space (~90 µm) are optimal, as they promote finer microstructures and faster cooling rates, enhancing hardness.

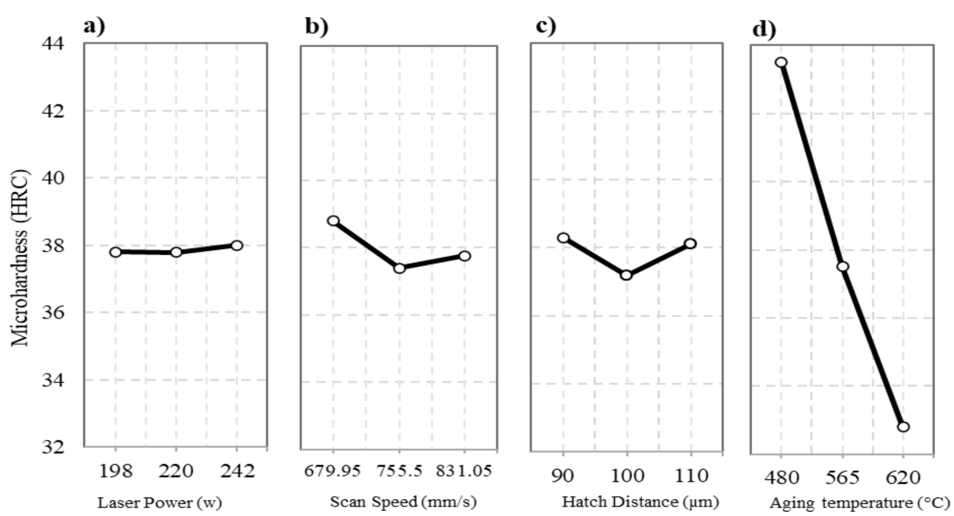

Figure 1.9: Effect of a) laser power, b) scan speed, c) hatch distance and d) aging temperature on the microhardness.

The predictive regression model for microhardness (HRC), formulated in Eq. 6, quantitatively characterizes the influence of LPBF process parameters and post-processing heat treatment on the mechanical response of 17-4 PH stainless steel. The model employs a multiple linear regression approach, selected for its interpretability and adequacy based on the observed linearity between the independent variables and microhardness response.

$$Microhardness = 849.3 - 0.0063\,P - 0.0666\,V - 0.134\,HD - 0.7377\,T \qquad \text{Eq. 6}$$

Where: P is laser power (W), V is scanning speed (mm/s), HD is hatching distance (μm), and T is aging temperature (°C). The regression coefficients directly quantify the sensitivity of microhardness to each process variable. Notably, the negative coefficient for aging temperature (-0.7377, $p < 0.001$) reflects a strong inverse relationship, indicating that hardness decreases significantly with increased thermal exposure due to precipitate coarsening and matrix softening.

The model demonstrates high fidelity, as evidenced by a coefficient of determination ($R^2 = 97.96\%$), adjusted R^2 (97.59%), and predicted R^2 (96.98%). The close proximity of these values indicates minimal overfitting and robust generalizability to new conditions. The standard error of the estimate (S = 6.83 HRC) is low relative to the range of measured values (32.68 to 44.52 HRC), supporting precise predictive resolution.

Figure 1.10-(a) depicts the correlation between predicted and experimental microhardness values, with data points aligned closely along the line of unity. The near-unity slope of the fitted curve ($y = 0.0001x^2 + 0.991x$) and minimal nonlinearity confirm that a linear model sufficiently captures the system behavior. Figure 1.10-(b) details the residual errors, all of which remain below 5%, with a mean absolute percentage error (MAPE) of approximately 1.65%, substantiating the model's practical accuracy.

ANOVA further confirms the significance of the regression: the model's F-value (264.18) and corresponding p-value (<0.001) indicate overall model validity. Among the process variables, scan speed ($p = 0.005$) also shows a statistically significant effect, while hatch distance ($p = 0.414$) and laser power ($p = 0.932$) are statistically insignificant under the current experimental conditions—though they may be influential under broader parameter windows. This model serves not only as an explanatory tool but also as a predictive framework for process optimization. By inputting desired hardness targets, practitioners can back-calculate feasible LPBF and heat treatment settings within defined operating envelopes, effectively reducing experimental iterations. Such a capability is vital in production settings where dimensional accuracy, surface integrity, and performance consistency are critical.

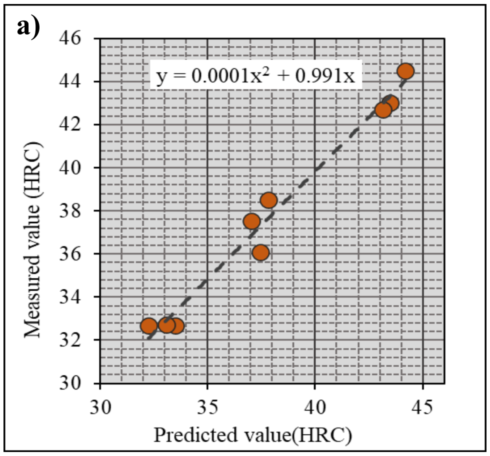

b)

Measured Microhardness (HRC)	Predicted Microhardness (HRC)	Error (%)
44.52	44.2	0.72
36.09	37.43	3.71
32.7	32.26	1.35
32.68	33.5	2.51
43.01	43.49	1.12
37.53	37.01	1.39
38.51	37.8	1.84
32.74	33.08	1.04
42.7	43.14	1.03

Figure 1.10: (a) Correlation between Predicted and Measured Microhardness Values; (b) Comparison of Measured and Predicted Microhardness Values with Percentage Error.

1.1.5 Conclusion

In this study, the effects of processing parameters and aging treatment temperature on the microstructure and microhardness of LPBF manufactured 17-4 PH stainless steel were investigated. The results can be concluded as follows:

- The microstructure of the LPBF-manufactured 17-4 PH stainless steel consisted mainly of lath martensite with Cu-rich precipitates and minor retained austenite, consistent with the expected transformations after solution treatment and aging. This similarity to conventionally manufactured and aged 17-4 PH stainless steel was attributed to re-austenitization, which transformed the cellular structure formed during rapid solidification in the LPBF process into austenite, followed by rapid cooling that resulted in a quenched martensitic matrix. The aging treatment further refined the structure, promoting the precipitation of Cu-rich phases, with their distribution and morphology governed by the aging temperature. These features were observed in the optical and SEM micrographs, and the XRD results confirmed the dominance of martensitic phases. Compared to the literature, the observed features align with previously reported microstructures in conventionally processed 17-4 PH stainless steel after similar thermal treatments.

- The microhardness values for the LPBF-manufactured material were consistent with the range observed in conventionally manufactured 17-4 PH stainless steel at similar aging temperatures. Optical microscopy revealed the presence of porosity, primarily gas porosities and occasional lack-of-fusion (LOF) defects, particularly in samples processed with lower VED values (e.g., S2 and S3), where VED was as low as 54.1 J/mm^3. However, in samples processed within the optimal VED range of 65.5–88.9 J/mm^3, the porosity was minimized, with relative densities exceeding 98%. These defects did not greatly influence the overall distribution of microhardness within the sample, which was relatively consistent, except for a slight increase at 565°C due to precipitation formation. It was observed that once relative density surpassed 98%, the impact of internal defects on hardness became negligible, and aging temperature emerged as the dominant factor. Although these defects do not strongly influence the value of microhardness, their presence in some cross-section areas seems to promote a local plastic deformation. This observation shows the demand for more in-depth studies on the influence of manufacturing defects on the mechanical behavior of materials, which will be addressed in future investigations.
- The statistical analysis has further supported these experimental observations: the aging temperature is the most important factor in the microhardness analysis. Increased aging temperature decreased the microhardness correspondingly from 44.52 HRC to 32.68 HRC. A prediction model for LPBF-manufactured 17-4 PH stainless steel was developed to estimate its microhardness with an error margin of less than 5%. The method further develops the predictability of microhardness from processing conditions and provides a useful tool for optimizing the mechanical properties of additively manufactured 17-4 PH stainless steel.

1.1.6 References

[1] S. A. M. Tofail, E. P. Koumoulos, A. Bandyopadhyay, S. Bose, L. O'Donoghue, and C. Charitidis, 'Additive manufacturing: scientific and technological challenges, market uptake and opportunities', *Materials Today*, vol. 21, no. 1, pp. 22–37, Jan. 2018, doi: 10.1016/j.mattod.2017.07.001.

[2] A. K. Kushwaha *et al.*, 'Powder bed fusion–based additive manufacturing: SLS, SLM, SHS, and DMLS', in *Tribology of Additively Manufactured Materials*, Elsevier, 2022, pp. 1–37. doi: 10.1016/B978-0-12-821328-5.00001-9.

[3] H. Jayawardane, I. J. Davies, J. R. Gamage, M. John, and W. K. Biswas, 'Sustainability perspectives – a review of additive and subtractive manufacturing', *Sustainable Manufacturing and Service Economics*, vol. 2, p. 100015, Apr. 2023, doi: 10.1016/j.smse.2023.100015.

[4] A. K. Pal, A. K. Mohanty, and M. Misra, 'Additive manufacturing technology of polymeric materials for customized products: recent developments and future prospective', *RSC Adv.*, vol. 11, no. 58, pp. 36398–36438, 2021, doi: 10.1039/D1RA04060J.

[5] M. Gouné, T. Iung, and J. Schmitt, *New Advanced High Strength Steels: Optimizing Properties*, 1st ed. Wiley, 2023. doi: 10.1002/9781394257430.

[6] A. Stashkov *et al.*, 'Magnetic, electric properties and hardness of 17-4 PH stainless steel fabricated by selective laser melting', *J. Phys.: Conf. Ser.*, vol. 1389, no. 1, p. 012124, Nov. 2019, doi: 10.1088/1742-6596/1389/1/012124.

[7] M. Bahrami Balajaddeh and H. Naffakh-Moosavy, 'Pulsed Nd:YAG laser welding of 17-4 PH stainless steel: Microstructure, mechanical properties, and weldability investigation', *Optics & Laser Technology*, vol. 119, p. 105651, Nov. 2019, doi: 10.1016/j.optlastec.2019.105651.

[8] M. A. Aripin, Z. Sajuri, J. Syarif, A. H. Baghdadi, and I. F. Mohamed, 'Evaluation of microstructure and porosity for 3D printed stainless steel', *Materials Today: Proceedings*, vol. 66, pp. 3082–3086, 2022, doi: 10.1016/j.matpr.2022.07.396.

[9] S. Sabooni *et al.*, 'Laser powder bed fusion of 17–4 PH stainless steel: A comparative study on the effect of heat treatment on the microstructure evolution and mechanical properties', *Additive Manufacturing*, vol. 46, p. 102176, Oct. 2021, doi: 10.1016/j.addma.2021.102176.

[10] K. Li *et al.*, 'Homogenization timing effect on microstructure and precipitation strengthening of 17–4PH stainless steel fabricated by laser powder bed fusion', *Additive Manufacturing*, vol. 52, p. 102672, Apr. 2022, doi: 10.1016/j.addma.2022.102672.

[11] Y. H. Kim, M. K. Kim, J. Suhr, T. Lee, and M. K. Kim, 'Exploring the Effect of Heat Treatment on the Mechanical Performance of 17-4PH Stainless Steel Specimens Fabricated by Metal Additive Manufacturing', *Exp Mech*, vol. 64, no. 8, pp. 1333–1342, Oct. 2024, doi: 10.1007/s11340-024-01089-3.

[12] Y. Abe *et al.*, 'Effect of Layer Directions on Internal Structures and Tensile Properties of 17-4PH Stainless Steel Parts Fabricated by Fused Deposition of Metals', *Materials*, vol. 14, no. 2, p. 243, Jan. 2021, doi: 10.3390/ma14020243.

[13] M. Laleh, A. E. Hughes, W. Xu, I. Gibson, and M. Y. Tan, 'A critical review of corrosion characteristics of additively manufactured stainless steels', *International Materials Reviews*, vol. 66, no. 8, pp. 563–599, Nov. 2021, doi: 10.1080/09506608.2020.1855381.

[14] Z.-C. Fang, Z.-L. Wu, C.-G. Huang, and C.-W. Wu, 'Review on residual stress in selective laser melting additive manufacturing of alloy parts', *Optics & Laser Technology*, vol. 129, p. 106283, Sep. 2020, doi: 10.1016/j.optlastec.2020.106283.

[15] T.-H. Hsu *et al.*, 'Effect of processing parameters on the fractions of martensite in 17-4 PH stainless steel fabricated by selective laser melting', *Journal of Alloys and Compounds*, vol. 859, p. 157758, Apr. 2021, doi: 10.1016/j.jallcom.2020.157758.

[16] T. A. M. Sghaier, H. Sahlaoui, T. Mabrouki, H. Sallem, and J. Rech, 'A comparative study on microstructure and mechanical properties of 17-4PH processed by a laser powder bed fusion vs rolling process', *Prog Addit Manuf*, Oct. 2024, doi: 10.1007/s40964-024-00837-0.

[17] L. Huang, Y. Cao, H. Zhao, Y. Li, Y. Wang, and L. Wei, 'Effect of process parameters on density and mechanical behaviour of a selective laser melted 17-4PH stainless steel alloy', *Open Physics*, vol. 20, no. 1, pp. 66–77, Feb. 2022, doi: 10.1515/phys-2022-0008.

[18] E. Yasa, İ. Atik, and İ. Kandemir, 'Material-specific phenomena and developing higher yield process parameters in laser powder bed fusion of 17-4 PH stainless steel', *J Braz. Soc. Mech. Sci. Eng.*, vol. 45, no. 1, p. 38, Jan. 2023, doi: 10.1007/s40430-022-03946-5.

[19] L. Facchini, E. Magalini, P. Robotti, A. Molinari, S. Höges, and K. Wissenbach, 'Ductility of a Ti-6Al-4V alloy produced by selective laser melting of prealloyed powders', *Rapid Prototyping Journal*, vol. 16, no. 6, pp. 450–459, Oct. 2010, doi: 10.1108/13552541011083371.

[20] S. Y. Liu, S. Shao, H. Guo, R. Zong, C. X. Qin, and X. Y. Fang, 'The microstructure and fatigue performance of Inconel 718 produced by laser-based powder bed fusion and post heat treatment', *International Journal of Fatigue*, vol. 156, p. 106700, Mar. 2022, doi: 10.1016/j.ijfatigue.2021.106700.

[21] S. Sabooni *et al.*, 'Laser powder bed fusion of 17–4 PH stainless steel: A comparative study on the effect of heat treatment on the microstructure evolution and mechanical properties', *Additive Manufacturing*, vol. 46, p. 102176, Oct. 2021, doi: 10.1016/j.addma.2021.102176.

[22] S. E. Kovacs *et al.*, 'Additive Manufacturing of 17-4PH Alloy: Tailoring the Printing Orientation for Enhanced Aerospace Application Performance', *Aerospace*, vol. 10, no. 7, p. 619, Jul. 2023, doi: 10.3390/aerospace10070619.

[23] R. Huang *et al.*, 'Additive manufacturing of 17-4PH stainless steel: Effect of heat treatment on microstructure evolution and strengthening behavior', *Materials Science and Engineering: A*, vol. 908, p. 146770, Aug. 2024, doi: 10.1016/j.msea.2024.146770.

[24] A. Mansoura, S. Dehghan, N. Barka, S. Sattarpanah Karganroudi, and M. Houria, 'Effect of heat treatment parameters on microstructure and microhardness of 15-5PH stainless steel fabricated by selective laser melting', *J Braz. Soc. Mech. Sci. Eng.*, vol. 46, no. 7, p. 424, Jul. 2024, doi: 10.1007/s40430-024-04999-4.

[25] J. Negron, M. Ali, A. Almotari, A. Algamal, A. Alafaghani, and A. Qattawi, 'Impact of Different Heat Treatments on the Mechanical Properties and Microstructure of Precipitation-Hardened Stainless Steel Fabricated by Laser Powder Bed Fusion', *Metallogr. Microstruct. Anal.*, vol. 13, no. 2, pp. 317–331, Apr. 2024, doi: 10.1007/s13632-024-01051-8.

[26] U. K. Viswanathan, S. Banerjee, and R. Krishnan, 'Effects of aging on the microstructure of 17-4 PH stainless steel', *Materials Science and Engineering: A*, vol. 104, pp. 181–189, Oct. 1988, doi: 10.1016/0025-5416(88)90420-X.

[27] T. K. Shoemaker, Z. D. Harris, and J. T. Burns, 'Nanometer-scale porosity evolution and mechanical properties of additively manufactured 17-4PH stainless steel', *Materials Science and Engineering: A*, vol. 902, p. 146567, Jun. 2024, doi: 10.1016/j.msea.2024.146567.

[28] H. Mirzadeh and A. Najafizadeh, 'Aging kinetics of 17-4 PH stainless steel', *Materials Chemistry and Physics*, vol. 116, no. 1, pp. 119–124, Jul. 2009, doi: 10.1016/j.matchemphys.2009.02.049.

[29] C. N. Hsiao, C. S. Chiou, and J. R. Yang, 'Aging reactions in a 17-4 PH stainless steel', *Materials Chemistry and Physics*, vol. 74, no. 2, pp. 134–142, Mar. 2002, doi: 10.1016/S0254-0584(01)00460-6.

[30] M. A. Aripin *et al.*, ‘Effects of Build Orientations on Microstructure Evolution, Porosity Formation, and Mechanical Performance of Selective Laser Melted 17-4 PH Stainless Steel’, *Metals*, vol. 12, no. 11, p. 1968, Nov. 2022, doi: 10.3390/met12111968.

[31] M. A. Aripin *et al.*, ‘Microstructure and mechanical properties of selective laser melted 17–4 PH stainless steel; Build direction and heat treatment processes’, *Materials Today Communications*, vol. 36, p. 106479, Aug. 2023, doi: 10.1016/j.mtcomm.2023.106479.

[32] O. Jaballah, N. Omidi, C. Belmarouf, A. Iltaf, N. Barka, and A. E. Ouafi, ‘Optimization of LPBF Processing and Aging Treatment Parameters for Maraging Steel Using Genetic Algorithms: Experimental Validation and Fracture Behavior Analysis’, *Lasers Manuf. Mater. Process.*, May 2025, doi: 10.1007/s40516-025-00296-7.

[33] N. Omidi, A. Iltaf, M. Houria, M. Jahazi, N. Barka, and C. Belzile, ‘Enhancing Mechanical Properties of Additively Manufactured H13: A Two-Step Approach Integrating Processing Parameters Optimization and a Tailored Heat Treatment’, *Met. Mater. Int.*, vol. 31, no. 5, pp. 1286–1312, May 2025, doi: 10.1007/s12540-024-01808-4.

[34] A. Kerbout, A. Tanji, H. Hermawan, and N. Barka, ‘Influence of Selective Laser Melting Process and Heat Treatment Parameters on the Corrosion Resistance of 17-4 Precipitation Hardening Stainless Steel’, *Metals*, vol. 15, no. 3, p. 232, Feb. 2025, doi: 10.3390/met15030232.

[35] A. Sathyanath and A. Meena, ‘Microstructural evolution and strain hardening behavior of heat-treated 17-4 PH stainless steel’, *Materials Today Communications*, vol. 25, p. 101416, Dec. 2020, doi: 10.1016/j.mtcomm.2020.101416.

[36] N. Omidi, M. Houria, M. M. Monjez, M. Jahazi, N. Barka, and A. E. Ouafi, ‘Processing parameters optimization for enhanced mechanical strength in PBF-ed H13 tool steel: minimizing manufacturing defects including microstructural inhomogeneity, sub-surface porosities, and oxide formation’, *Int J Adv Manuf Technol*, vol. 136, no. 5–6, pp. 2681–2706, Jan. 2025, doi: 10.1007/s00170-024-14951-4.

[37] A. Mansoura, S. Dehghan, N. Barka, and S. S. Kangranroudi, ‘Investigation into the effect of process parameters on density, surface roughness, and mechanical properties of 316L stainless steel fabricated by selective laser melting’, *Int J Adv Manuf Technol*, vol. 130, no. 5–6, pp. 2547–2562, Jan. 2024, doi: 10.1007/s00170-023-12865-1.

[38] S. Cheruvathur, E. A. Lass, and C. E. Campbell, ‘Additive Manufacturing of 17-4 PH Stainless Steel: Post-processing Heat Treatment to Achieve Uniform Reproducible Microstructure’, *JOM*, vol. 68, no. 3, pp. 930–942, Mar. 2016, doi: 10.1007/s11837-015-1754-4.

[39] C. Garcia-Cabezon, M. A. Castro-Sastre, A. I. Fernandez-Abia, M. L. Rodriguez-Mendez, and F. Martin-Pedrosa, ‘Microstructure–Hardness–Corrosion Performance of 17–4 Precipitation Hardening Stainless Steels Processed by Selective Laser Melting in Comparison with Commercial Alloy’, *Met. Mater. Int.*, vol. 28, no. 11, pp. 2652–2667, Nov. 2022, doi: 10.1007/s12540-021-01155-8.

[40] H. Eskandari, H. R. Lashgari, L. Ye, M. Eizadjou, and H. Wang, ‘Microstructural characterization and mechanical properties of additively manufactured 17–4PH stainless steel’, *Materials Today Communications*, vol. 30, p. 103075, Mar. 2022, doi: 10.1016/j.mtcomm.2021.103075.

[41] T. LeBrun, T. Nakamoto, K. Horikawa, and H. Kobayashi, ‘Effect of retained austenite on subsequent thermal processing and resultant mechanical properties of selective laser melted 17–4 PH stainless steel’, *Materials & Design*, vol. 81, pp. 44–53, Sep. 2015, doi: 10.1016/j.matdes.2015.05.026.

[42] C. Rowolt, B. Milkereit, A. Springer, C. Kreyenschulte, and O. Kessler, ‘Dissolution and precipitation of copper-rich phases during heating and cooling of precipitation-hardening steel

X5CrNiCuNb16-4 (17-4 PH)’, *J Mater Sci*, vol. 55, no. 27, pp. 13244–13257, Sep. 2020, doi: 10.1007/s10853-020-04880-4.
[43] M. Avrami, ‘Kinetics of Phase Change. I General Theory’, *The Journal of Chemical Physics*, vol. 7, no. 12, pp. 1103–1112, Dec. 1939, doi: 10.1063/1.1750380.
[44] K. Barmak, ‘A Commentary on: “Reaction Kinetics in Processes of Nucleation and Growth”*’, *Metall Mater Trans B*, vol. 49, no. 6, pp. 3616–3680, Dec. 2018, doi: 10.1007/s11663-010-9421-1.
[45] M. Murayama, K. Hono, and Y. Katayama, ‘Microstructural evolution in a 17-4 PH stainless steel after aging at 400 °C’, *Metall Mater Trans A*, vol. 30, no. 2, pp. 345–353, Feb. 1999, doi: 10.1007/s11661-999-0323-2.
[46] H. Mirzadeh and A. Najafizadeh, ‘Aging kinetics of 17-4 PH stainless steel’, *Materials Chemistry and Physics*, vol. 116, no. 1, pp. 119–124, Jul. 2009, doi: 10.1016/j.matchemphys.2009.02.049.
[47] G. Yeli, M. A. Auger, K. Wilford, G. D. W. Smith, P. A. J. Bagot, and M. P. Moody, ‘Sequential nucleation of phases in a 17-4PH steel: Microstructural characterisation and mechanical properties’, *Acta Materialia*, vol. 125, pp. 38–49, Feb. 2017, doi: 10.1016/j.actamat.2016.11.052.
[48] H. Mirzadeh and A. Najafizadeh, ‘Aging kinetics of 17-4 PH stainless steel’, *Materials Chemistry and Physics*, vol. 116, no. 1, pp. 119–124, Jul. 2009, doi: 10.1016/j.matchemphys.2009.02.049.
[49] K. Li *et al.*, ‘Homogenization timing effect on microstructure and precipitation strengthening of 17–4PH stainless steel fabricated by laser powder bed fusion’, *Additive Manufacturing*, vol. 52, p. 102672, Apr. 2022, doi: 10.1016/j.addma.2022.102672.
[50] A. Dash and A. Bandyopadhyay, ‘17-4 PH and SS316L bimetallic structures via additive manufacturing’, *Virtual and Physical Prototyping*, vol. 19, no. 1, p. e2292695, Dec. 2024, doi: 10.1080/17452759.2023.2292695.
[51] S. Sabooni *et al.*, ‘Laser powder bed fusion of 17–4 PH stainless steel: A comparative study on the effect of heat treatment on the microstructure evolution and mechanical properties’, *Additive Manufacturing*, vol. 46, p. 102176, Oct. 2021, doi: 10.1016/j.addma.2021.102176.
[52] M. Rezayat, M. Morales, M. Moradi, and A. Mateo, ‘Laser wobbling surface texturing of AISI 301LN steel for enhancement of the corrosion resistance at high temperature’, *Optics & Laser Technology*, vol. 171, p. 110375, Apr. 2024, doi: 10.1016/j.optlastec.2023.110375.
[53] S. Mahadevan, R. Manojkumar, T. Jayakumar, C. R. Das, and B. P. C. Rao, ‘Precipitation-Induced Changes in Microstrain and Its Relation with Hardness and Tempering Parameter in 17-4 PH Stainless Steel’, *Metall Mater Trans A*, vol. 47, no. 6, pp. 3109–3118, Jun. 2016, doi: 10.1007/s11661-016-3440-8.
[54] Dossett, J., & Totten, G. E., *ASM Handbook, Volume 4A: Steel Heat Treating Fundamentals and Processes, ASM Intern.* 2013.

CHAPITRE 2
EXPLORATION DE L'EFFET DES PARAMÈTRES DE FABRICATION ADDITIVE SUR LA MICROSTRUCTURE ET LE COMPORTEMENT EN TRACTION DE L'ACIER 17-4 PH APRÈS TRAITEMENTS THERMIQUES : UNE INVESTIGATION EXPÉRIMENTALE ET STATISTIQUE

Cet article a été publié dans « The International Journal of Advanced Manufacturing Technology » portant le numéro de référence : JAMT-D-25-01922R2

2.1 RÉSUMÉ EN FRANÇAIS DU DEUXIÈME ARTICLE

Cette étude analyse les effets des paramètres du procédé LPBF – puissance du laser, vitesse de balayage et espacement des hachures – ainsi que des traitements thermiques subséquents (H900, H1025 et H1150) sur les propriétés mécaniques de l’acier inoxydable 17-4 PH. Les observations microstructurales révèlent des changements minimes de la taille des grains d’austénite et des lames de martensite dans les matériaux traités avec différents paramètres de processus mais soumis à une même température de traitement thermique.

Ces variations n'ont eu qu’un effet négligeable sur la résistance à la traction (UTS) et sur la limite d'élasticité (YS), ces dernières étant principalement gouvernées par le traitement thermique, qui contrôle la cinétique de précipitation, la taille et la formation des phases de renforcement – des mécanismes clés dans l’acier inoxydable 17-4 PH. L'analyse statistique a montré que la température de vieillissement expliquait 96,20 % de la variation de l'UTS et 94 % de la variation de l'YS, mettant en évidence l’influence minimale des autres variables. En revanche, l'élongation était davantage influencée par les paramètres de traitement, avec 75,41 % de la contribution provenant de la température de vieillissement, ce qui est inférieur à l’influence observée sur l'UTS et l'YS. L'élongation est étroitement liée aux porosités, qui

initient des fissures et réduisent l'élongation. Cet effet était particulièrement plus prononcé à des températures de vieillissement plus élevées (par exemple, 620°C), où des défauts ont provoqué des creux anormaux qui, bien que petits et difficiles à détecter par microscopie optique, ont affecté l'élongation d'environ 2 %. Pour éviter de tels défauts, il est recommandé d'adopter une densité d'énergie volumétrique (VED) supérieure à 70 J/mm³, car cela permet d'obtenir des caractéristiques de fracture comparables à celles des matériaux fabriqués de manière conventionnelle. Enfin, des modèles prédictifs pour l'UTS, l'YS et l'élongation ont été développés avec une marge d'erreur inférieure à 5 %. Ces modèles, recommandés pour des plages de VED comprises entre 70 et 90 J/mm³, permettent de prédire avec une grande précision les propriétés du matériau pour tous les paramètres de fabrication et des températures de vieillissement, en particulier dans la région élastique, garantissant des propriétés matérielles cohérentes pour des applications critiques de précision.

Mots-clés : Fusion Laser sur Lit de Poudre, Acier inoxydable 17-4 PH, Traitement de vieillissement, Comportement en traction, Modèle de régression prédictif.

Cet article intitulé "Exploring the Effect of Processing Parameters on the Microstructure and Tensile Behavior of 17-4 PH Steel after Heat Treatments: An Experimental study with Statistical Investigation", a été soumis pour publication à la revue "*The International Journal of Advanced Manufacturing Technology"* le 09 Avril 2025, a été accepté pour publication le 17 Juin 2025 et a été publié le 05 Août 2025. En tant que premier auteur, j'ai été principalement responsable de la conception de l'expérience, la conduite des essais, la collecte et l'analyse des données, ainsi que de l'analyse expérimentale et statistique, tout en rédigeant l'article. Narges Omidi a supervisé l'analyse expérimentale et statistique des données et a contribué à la discussion, la révision et l'édition du manuscrit. Pedram Farhadipour et Asim Iltaf, ont assisté dans les tests mécaniques, en particulier pour la section du test de traction et les images de fractographie. Le professeur Noureddine Barka directeur principal, a défini le concept de la recherche et a supervisé l'orientation générale du projet. Professeur Abderrazak El Ouafi, second superviseur.

2.2 EXPLORING THE EFFECT OF PROCESSING PARAMETERS AND POST-PROCESSING HEAT TREATMENT ON THE MICROSTRUCTURE AND TENSILE BEHAVIOR OF 17-4 PH STEEL: AN EXPERIMENTAL STUDY WITH STATISTICAL INVESTIGATION

Yassmine Chedly, Narges Omidi*, Pedram Farhadipour, Asim Iltaf, Noureddine Barka, Abderrazak El Ouafi

Department of Mathematics, Computer Science and Engineering, University of Québec at Rimouski (UQAR), Rimouski, Québec G5L 3A1, Canada.

2.2.1 Abstract

This study analyzes the effects of LPBF processing parameters—laser power, scanning speed, and hatch spacing—and post-processing heat treatments (H900, H1025, and H1150) on the mechanical properties of 17-4 PH stainless steel. Microstructural observations revealed minimal changes in prior austenite grain size and martensite lath size across materials processed with different laser speeds, hatch spacing, and laser power but subjected to the same heat treatment temperature. These changes had negligible effects on UTS and YS, which were primarily governed by heat treatment due to its control over precipitation kinetics, size, and formation of strengthening phases—key mechanisms in 17-4 PH stainless steel. Statistical analysis showed that aging temperature contributed 96.20% to UTS and 94% to YS, highlighting the minimal influence of other variables. In contrast, elongation was more influenced by processing parameters, with 75.41% of the contribution coming from aging temperature, which is lower compared to UTS and YS. Elongation is closely linked to porosities, which initiate cracks and reduce elongation. This effect was particularly more pronounced at higher aging temperatures (e.g., 620°C), where defects caused abnormal dimples that, although small and difficult to detect with optical microscopy, affected elongation by around 2%. To avoid such abnormal dimples, a VED above 70 J/mm³ is recommended, as it results in fracture characteristics comparable to those of conventionally manufactured materials. Finally, predictive models for UTS, YS, and elongation were developed which recommended for VED ranges between 70 and 90 J/mm³, enable the prediction of material properties at any processing parameters and temperatures with high

precision, particularly in the elastic region, ensuring consistent material properties for precision applications.

Key words: 17-4 PH Stainless Steel, Laser Powder Bed Fusion, Aging Treatment, Tensile Behavior, Predictive Regression Model.

2.2.2 Introduction

Additive manufacturing (AM) has transformed materials processing and production through revolutionary techniques like as laser powder bed fusion (LPBF) [1], [2], [3]. 17-4 PH stainless steel is esteemed for its distinctive amalgamation of exceptional strength, corrosion resistance, and dimensional stability [4]. High weldability of this metal renders it appropriate for laser-based additive manufacturing such as LPBF [5].

LPBF offers several advantages over conventional manufacturing techniques, including high design flexibility, near-net-shape fabrication, reduced material waste, and the ability to produce complex geometries with refined microstructures due to rapid solidification. These features make LPBF particularly attractive for advanced engineering applications. However, despite these benefits, the process also introduces several challenges that can affect the performance and reliability of the fabricated components. Common issues include the presence of porosity (such as lack-of-fusion, keyhole, and gas pores) [6], elemental evaporation, and microstructural inhomogeneities resulting from rapid thermal cycling and the layer-by-layer nature of the process [7]. These effects can lead to retained austenite, grain structure variability, oxide formation, and contamination. Additionally, the as-built surface roughness is inherently high, acting as a critical factor in fatigue-sensitive applications due to its role in crack initiation. These surface and internal defects, influenced by process parameters and material behavior, significantly affect mechanical properties and fatigue performance. Therefore, optimization of processing conditions and post-processing treatments is essential [8], [9].

Several studies focus on the effect of gas atomization atmosphere on mechanical performance of 17-4 PH. Shaffer et al. [10] compared the mechanical characteristics of 17-4

PH steel produced through LPBF with nitrogen- and argon-atomized powders. Nitrogen-atomized materials retained up to 81% austenite, resulting in tensile strengths 200 MPa higher than argon-atomized materials, with a peak-aged strength of 1563 ± 13 MPa. In contrast, argon-atomized materials showed martensitic microstructures and properties like wrought steels. Stoudt et al. [11] explored the effects of retained nitrogen on the corrosion resistance. Their work showed that the nitrogen-atomized alloys had significantly enhanced pitting resistance as compared to the argon-atomized and wrought parts, especially in neutral pH. The enhanced performance was consequently attributed to residual nitrogen, which stabilized the passive oxide film and increased the critical pitting potential, affecting changes in ionic activity at the electrode surface.

Some researchers have focused on optimizing the processing parameters for attaining maximum mechanical properties, including laser scanning speed, laser power, and scanning spacing. Huang et al. [12] illustrated how processing parameters lead to material density and microstructural variations, with direct implications for mechanical performance. The results of their studies showed that the optimal set of parameters enhanced mechanical behavior above the specifications of ASTM, such that yield strength reached 1132 MPa, tensile strength was 1323 MPa, and elongation attained 16.6%. Ponnusamy et al. [13] reported that LPBF-manufactured components have a UTS of 1128 MPa, higher compared to that obtained from the wrought specimens, which is about 1028 MPa, while its ductility is 2% higher. On the other hand, LPBF parts have shown less yield strength than those from the wrought samples. Microstructural analysis showed that retained austenite content was high in the LPBF components, contributing to enhanced ductility, but predominantly martensitic in the wrought ones. The study by Irrinki et al. [14] showed that gas-atomized powders offered superior densification and mechanical properties at low energy densities, while water-atomized powders achieved comparable results at higher energy densities (104 J/mm^3), making them a cost-effective alternative for LPBF. Despite reaching 97% ± 1% theoretical density, mechanical properties varied widely, with tensile strength ranging from 500 to 1100 MPa and hardness from 25 to 39 HRC, influenced by powder and process parameters.

The mechanical properties of LPBF-manufactured 17-4 PH steel are affected by both processing factors and subsequent heat treatments. Li et al. [15] examined the impact of various aging temperatures on the microstructure and mechanical properties of 17-4 PH stainless steel. The highest mechanical properties, UTS of 1387 MPa and elongation of 7.3%, were given by solution treatment followed by aging at 450°C for 5 hours. This improved strength from the as-built condition was considered to be a consequence of precipitation of NbC and ε-Cu phase nanoparticles during aging, which created obstacles for dislocation movement and thus caused hardening. However, as the aging temperature was increased further, the precipitates coarsened, which decreased the strength but enhanced plasticity. The UTS of heat-treated samples showed a 25.2% increase compared to as-built samples.

Recent studies have examined the effects of both processing parameters and post-processing heat treatment temperatures on the mechanical behavior of PBF-manufactured 17-4 PH steel, with particular emphasis on the influence of build direction. Aripin et al. [16] show that The tensile properties varied significantly depending on both the heat treatment and the build orientation. The 90° build direction exhibited lower tensile properties compared to the 0° direction in both as-built and heat-treated conditions. For the 0° build direction, as-built samples exhibited a yield strength of 472 MPa, a UTS of 958 MPa, and an elongation of 26%. Following the H750 heat treatment, these values improved to a yield strength of 537 MPa, UTS of 1260 MPa, and elongation of 16%. In contrast, the H1100 treatment resulted in reduced yield strength and ductility, with the UTS slightly increasing to 984 MPa, but yield strength dropping to 375 MPa, and elongation decreasing to 11%.

Kim et al. [17] investigated the influence of different post-processing heat treatments such as HIP, solution treatment, and aging in vertical and horizontal build orientations. It was observed that HIP and aging was the best heat treatment that enhanced the yield strength by 118% to 986 MPa for the horizontally stacked components, while the tensile strength increased beyond 1159 MPa. The highest ductility value is 20.6% for the vertically oriented samples, after just aging, whereas it was severely knocked down by high-temperature treatments such as solution treatment.

The main purpose of this research is to investigate the effect of the different processing parameters and post-processing heat treatment on the microstructure mechanical behavior LPBF-d 17-4 PH stainless steel.

2.2.3 Material and methods

The material selected for this study was alloy 17-4 PH, a precipitation-hardened martensitic stainless steel. The argon gas-atomized powder used with sizes ranged 10 to 45 µm. Figure 2.1-(a) and Figure 2.1-(b) illustrate the morphology and size distribution, which are taken from the powder particles before manufacturing process. The nominal chemical composition, as provided by EOS, is outlined in Table 2.1.

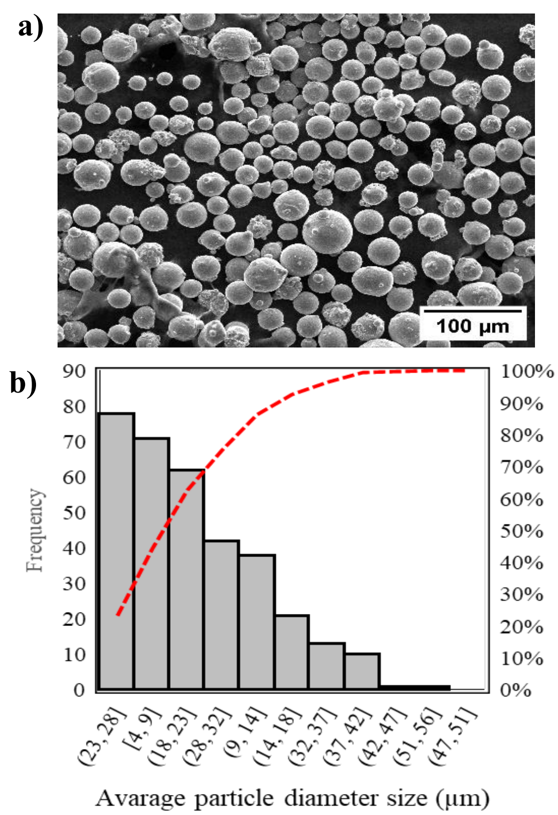

Figure 2.1: a) SEM image of the morphology of the 17-4 PH powder, b) size distribution of 17-4 PH particles.

The 17-4 PH stainless steel samples were fabricated using an EOS M290 LPBF system. The PBF process was performed under an inert argon atmosphere. The sample sizes were prepared in two sizes for microstructure/microhardness testing, and tensile testing, with dimensions of 10×10×15 mm³ and 100×5×14 mm³ respectively. The variables studied included laser power, laser speed, hatching distance, and three different parameter levels, with their variations presented in Table 2.2, with constant layer thickness of 40µm. The selected range of the variables was determined by applying a 10% variation from the optimal parameters provided by the manufacturer (P = 220 W, V = 755.5 mm/s, HD = 100 µm) in order to avoid issues such as balling effect, conduction, and keyhole mode [18], [19].

Table 2.1: Chemical composition of EOS 17-4 PH Stainless Steel powder for LPBF.

Element	**Fe**	**C**	**Mn**	**P**	**S**
Wt. %	Bal.	0.07 max	1.0 max	0.04 max	0.03 max
Element	**Si**	**Cr**	**Ni**	**Cu**	**Nb, Ta**
Wt. %	1.0 max	15.0-17.5	3.0-5.0	3.0-5.0	0.15-0.45

Following the LPBF procedure, heat treatments were applied as post-processing steps. Initially all samples subjected to a stress-relieving heat treatment for one hour at 650°C. Then underwent solution annealed at 1040°C for 30 minutes followed by air-cooling.
Finally, aging treatments were carried out for one hour at different temperatures: 480°C (H900), 565°C (H1025), and 620°C (H1150); presented in

Figure 2.2. These temperatures were selected in order to induce precipitation hardening, which is known to significantly improve the strength and hardness of 17-4 PH stainless steel by the controlled formation of precipitates rich in copper [20], [21], [22]. The heat treatment cycles are presented in .

Table 2.2: Process parameters and their levels.

Process parameters	**Symbol**	**Units**	**Levels**		
			1	**2**	**3**
Laser power	P	w	198	220	242
Scan speed	V	mm/s	679.95	755.5	831.05
Hatch distance	HD	µm	90	100	110
Aging temperature	T	°C	480	565	620

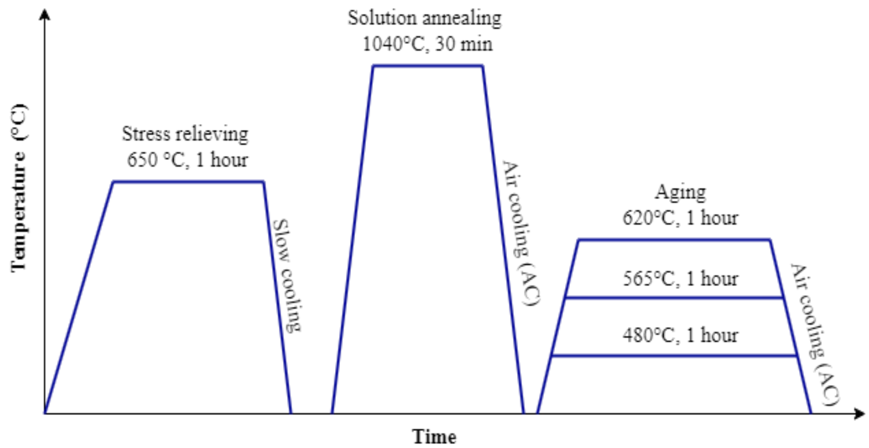

Figure 2.2: Heat treatment temperature diagram.

To study the combined effects of LPBF and post-processing heat treatment, a Taguchi L9 orthogonal design with four parameters at three levels (taken from Table 2.2) was implemented for DOE (given in Table 2.3). The VED in the table represents the volumetric energy density during the process. The VED ranged from 54.148 to 88.977 J/mm³ in this study and was calculated using the Equation (1). Where: P (w) is laser power, V (mm/s) is scan speed, LT (µm) is layer thickness, and HD (µm) is hatch distance.

$$VED = \frac{P}{V * LT * HD} \qquad \text{Equation (1)}$$

After the post-processing heat treatment, the tensile specimens were then machined to achieve the final geometry for tensile testing, with dimensions conforming to ASTM E8/M8 standards and sandblasted for surface finishing and the removal of rust or any other defects that could affect the geometry.

Table 2.3: Design of experiment.

NO	Laser Power P (w)	Scan Speed V (mm/s)	Hatch Distance HD (µm)	VED (J/mm3)	Aging temperature T (°C)
S1	198	679.95	90	80.888	480
S2	198	755.5	100	65.519	565
S3	198	831.05	110	54.148	620
S4	220	679.95	100	80.888	620
S5	220	755.5	110	66.181	480
S6	220	831.05	90	73.535	565
S7	242	679.95	110	80.888	565
S8	242	755.5	90	88.977	620
S9	242	831.05	100	72.799	480

Figure 2.3-(a) and Figure 2.3-(b), shows samples direction during the LPBF process and the dimension of the prepared tensile test.

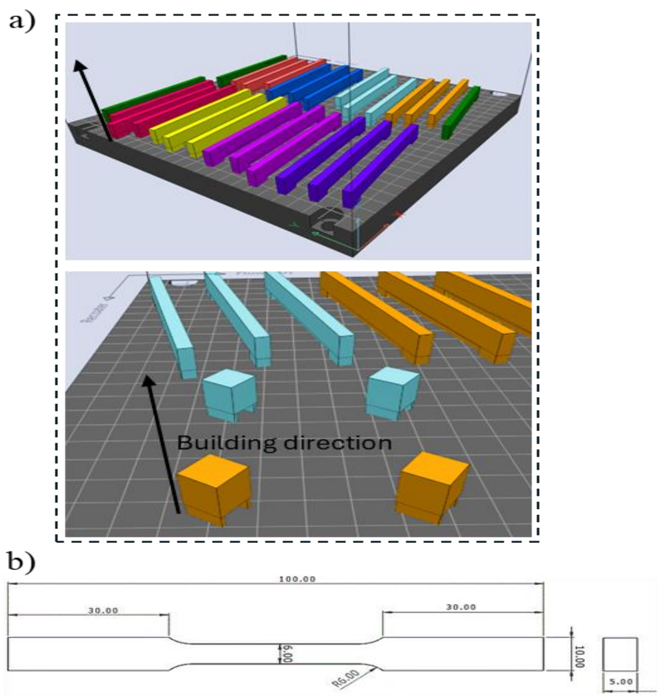

Figure 2.3: Schematics of the samples showing (a) the building direction and (b) the dimensions of the tensile test sample.

Microstructural observations were performed using optical microscopy, and microhardness testing was conducted with a 300 gf load and a dwell time of 10 seconds. Standard tensile tests were carried out on an MTS810 Material Tensile Test Machine at a strain rate of 0.6 mm/min under room temperature conditions. Fractography analysis of the material was performed using an SEM machine (SEM-FEI QUANTA 200F instrument). The results from the experimental part were later statistically analyzed. By applying the ANOVA method, the influence of Variables: P, V, HD, and T on response variables: Ultimate tensile strength (UTS), yield stress (YS), and elongation (EL).

2.2.4 Results and Discussion

2.2.4.1 Microstructure analysis

Figure 2.4, Figure 2.5 and Figure 2.6 represent the microstructure in the build direction after heat treatment at different temperatures (H900, H1025, and H1115) with variation in processing parameters. Due to the solution annealing at 1040°C , the microstructural inhomogeneities including laser pass, wave-shaped inclusions, and acicular martensite in the build direction, which were reported by Aripin et al. [23] are no longer present.

However, it is noted that for the same heat treatment condition but different processing parameters, there are slight differences in the microstructure. Figure 2.4 shows the microstructure of the material in condition H900. A very minimal difference in the microstructure may be related to a high percentage of retained austenite, as much as 16% in an as-built condition [24]. This is attributed to the high content of austenite stabilizers and cooling rates during the LPBF process. Nickel (Ni), manganese (Mn), and copper (Cu) lower the martensite start (Ms) and finish (Mf) temperatures, allowing for the retention of austenite in the microstructure [25]. The concentration of stabilizers remains consistent across the material, indicating that the content of retained austenite in the as-built condition is primarily influenced by the cooling rate. Slower cooling rates are associated with an increase in retained austenite, as stated by Vysotskiy et al. [26] and Hsu et al. [27].

Retained austenite in the as-built condition can be quite stable [28], and potentially affects the austenitization process during solution annealing at 1040°C for 1 hour. The stable retained austenite impedes complete transformation to a homogeneous austenitic structure, leaving regions with untransformed phases and preventing uniform microstructural evolution. That in turn influences the resultant H900 microstructure. Optical micrographs in Figure 2.4-(a) to (c) show the microstructure of the material processed at three different VED levels: 66.181, 72.799, and 80.888 J/mm³. It can be observed that with the increase in VED, there is more contrast in the microstructure, with clearer martensitic boundaries and distinct martensitic laths within the prior austenite grain size as seen from Figure 2.4-(c). This can be linked to the reduced percentage of retained austenite observed at elevated VED levels, which aligns with an increased cooling rate. Retained austenite develops along the martensitic laths, resulting in a bright phase in optical microscopy because of its resistance to the etching process. The reduced quantity of retained austenite makes the grain boundary distinctly apparent. Retained austenite resides along the grain boundaries and martensitic laths during aging, where the precipitates act to stabilize it, thus enhancing its retention[25]. This behavior again corroborates with Niraj Nayan et al. [25], since the grain boundary is not so distinct for the materials containing more retained austenite.

Notably, at higher temperature conditions, the effect of retained austenite becomes less pronounced, and the microstructure at different volumetric energy densities (VEDs) appears very similar. This is due to the thermal instability of retained austenite: retained austenite becomes thermodynamically unstable at higher temperatures (e.g., 640–700°C). The thermal energy at these temperatures forces the retained austenite to turn into martensite, which homogenizes the microstructure in various VEDs. When the percentage of retained austenite decreases to a minimum value, its effect on the microstructure becomes negligible. In the H1025 condition, grain boundaries are still not clear from Figure 2.5-(a) to (c), probably because of the higher percentage of retained austenite. According to Niraj Nayan et al. [25], retained austenite can increase up to approximately 25.1% at aging temperatures around 495°C compared to the solution-annealed condition. In contrast, at H1150 (Figure 2.6-(a) to (c)), the differences in microstructure become nearly indistinguishable at the optical microscopy scale. At these higher temperatures, the grain boundaries become very clear, as the retained austenite reduces to it**s minimum levels** due to its transformation into martensite, which occurs at aging temperatures between 640–700°C [29].

The average microhardness values are shown in Table 2.4, which also reflect the changes in microstructure discussed in the optical microscopy images. Increasing VED reduced the amount of retained austenite in all conditions, slightly increasing the microhardness. In the H900 condition, increasing VED from 66.181 J/mm³ to 80.888 J/mm³ raised the microhardness from 420 HV to 440.25 HV, which is about a 20 HRC increase. The same trend was shown also by H1025 and H1150. It can be seen that, with the rise in aging temperature, the microhardness increment with higher VED becomes less distinctive. In H1150 conditions, the microhardness difference is less than 1 HV, meaning that the effect of retained austenite is eliminated and aging outweighs the effect of the parameters.

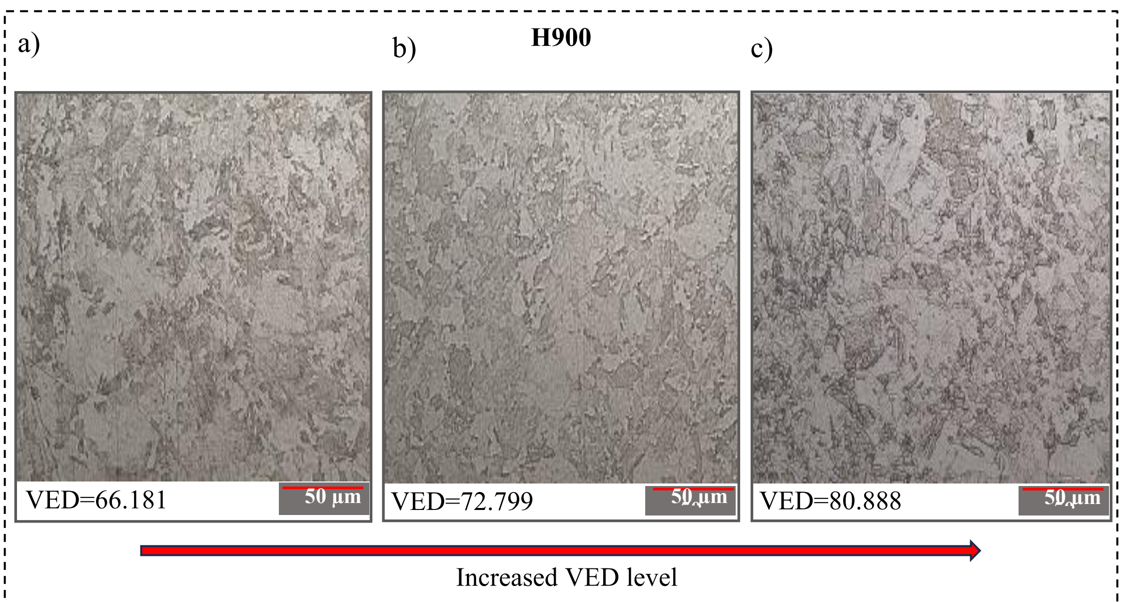

Figure 2.4: Optical microscopy images of the material under H900 heat treatment with different processing parameter conditions: a) at a VED of 66.181 J/mm³, b) at VED of 72.799 J/mm³, and c) at a VED of 80.888 J/mm³.

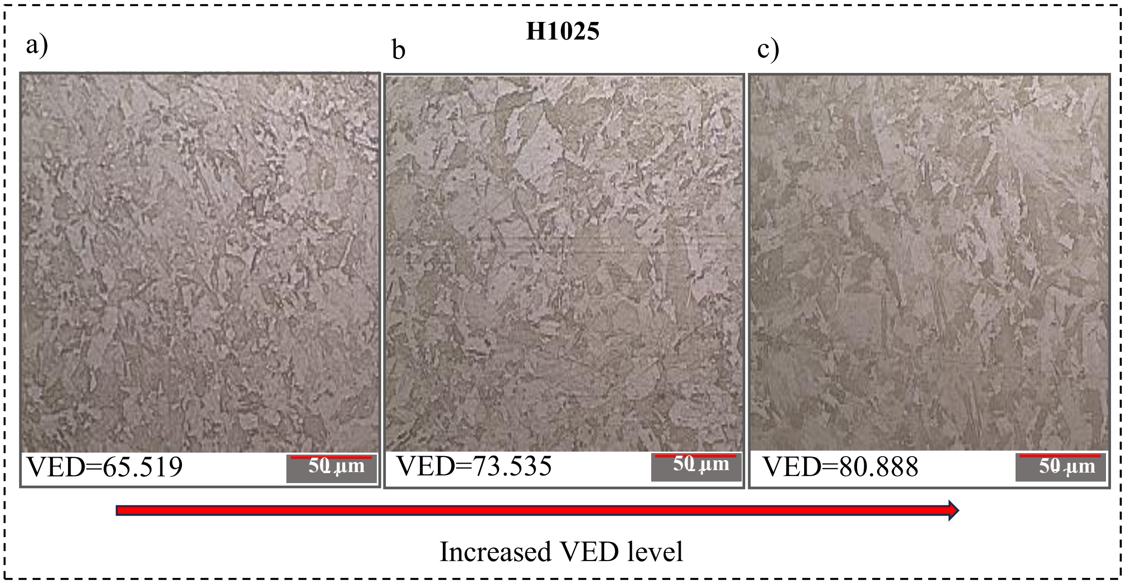

Figure 2.5: Optical microscopy images of the material under H1025 heat treatment with different processing parameter conditions: a) at a VED of 65.519 J/mm³, b) at a VED of 73.535 J/mm³, and c) at a VED of 80.888 J/mm.

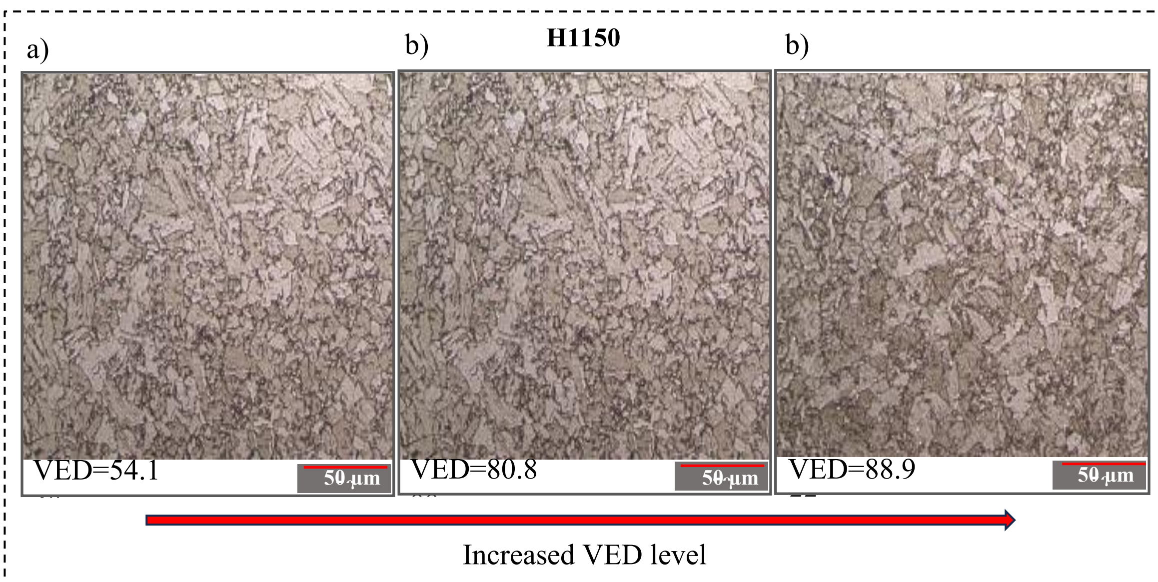

Figure 2.6: Optical microscopy images of the material under H1115 heat treatment with different processing parameter conditions (a) at a VED of 54.148 J/mm³, (b) at a VED of 80.888 J/mm³, and (c) at a VED of 88.977 J/mm³.

Table 2.4: Average value of the microhardness.

Aging condition	VED *(J/mm3)*	Microhardness (HV)
H900	66.181	423.44
	72.799	420
	8.0888	440.25
H1025	65.519	355.36
	73.535	368.45
	80.888	377.36
H1150	54.148	324.55
	80.888	324.36
	88.977	324.91

The higher magnification images of the microstructure after different aging conditions are shown in Figure 2.7. The microstructure of the material at the H900 condition in Figure 2.7-(a), with the lowest content of retained austenite, is predominantly martensitic, combined with retained austenite, possibly some reverted austenite, and precipitation. The martensitic structure exhibits clear martensite laths within the prior austenite grains. The aging treatment at this condition promotes the precipitation of M23C6 and NbC carbides, which predominantly nucleate at grain boundaries and martensitic laths. The formation of M23C6 carbides enhances Ni-enrichment in the regions adjacent to the carbides, stabilizing the retained austenite and improving the material's strength and hardness. In the same way, the reversed austenite forms by the diffusion of Ni and other elements during the aging process, building up the fraction of austenite in the microstructure. Three types of precipitates were observed: thin-plate carbide precipitates measuring between 50-150 nm in thickness, spherical carbides, and blocky-shaped carbides precipitating along grain boundaries or at triple points, which contribute to grain refinement and a pinning effect [24].

At the H1025 condition (Figure 2.7-(b)), the microstructure of 17-4 PH stainless steel exhibits a partially martensitic structure with an increasing fraction of retained austenite and exhibited coarser grain boundaries compared to H900 condition. The higher aging temperature promotes faster diffusion rates, leading to the coarsening of Cu-rich precipitates (CRPs) and Nb-rich precipitates, which nucleate at dislocations and grain boundaries. Where, at this temperature, the Cr-rich α′ precipitates are not important, in contrast to what happens at 480°C because the system is outside the miscibility gap of Fe and Cr. Aging at this temperature, instead, stabilizes and partially reverses austenite through Ni and Mn diffusion, thus increasing the fraction of retained austenite. The resulting microstructure is less complex; martensitic laths become indistinct, and grain boundaries are less evident with more retained austenite. Moreover, the coarsening of the precipitates, mainly CRPs, softens the material with time and reduces the effectiveness of hardening compared to the strong precipitation response at lower temperatures, such as H900. This microstructure, however, still possesses adequate strength and ductility through the contributions from both martensite and the dispersed precipitates [30].

Under the H1150 condition, as depicted in Figure 2.7-(c), the microstructure is a more fully developed with a tempered martensitic matrix compared to the lower aging conditions of H900 and H1025. In addition, it shows the coarsening of Cu-rich precipitates by increasing the aging temperature into larger sizes while reducing number density, which diminishes its effectiveness in dislocation pinning and precipitation strengthening. Other than that, M23C6 carbides nucleating at grain boundaries and the martensitic laths grow and coarsen to a large extent, thus stabilizing the grain boundary and improving toughness through stress relaxation, although with some reduction in its contribution towards hardening. NbC carbides show a trend for becoming larger and less uniformly distributed, with a further reduction in their strengthening effects. Compared with those minor precipitates which might generally present in lower temperatures, the Mn-Ni-Si-rich precipitates at this elevated temperature will either dissolve or become insignificant. H1150 shows higher grain boundary definition-clearer-which was attributed to the M23C6 stabilization effects and the transformation of most retained austenite into martensite [29].

Figure 2.8 shows the relationship between VED and relative density. VED values, greater than 70 J/mm^3, lead to relative densities close to 99%. In other studies—including work of Fri et al. [31]—a plateau in relative density is observed at higher VEDs. At higher

VED, the relative density of LPBF-manufactured material tends to stabilize due to the saturation of densification mechanisms. Initially, as VED increases, more energy is available to fully melt powder particles and eliminate lack-of-fusion (LOF) porosity, resulting in a sharp rise in relative density. However, beyond a critical threshold, this densification benefit diminishes.

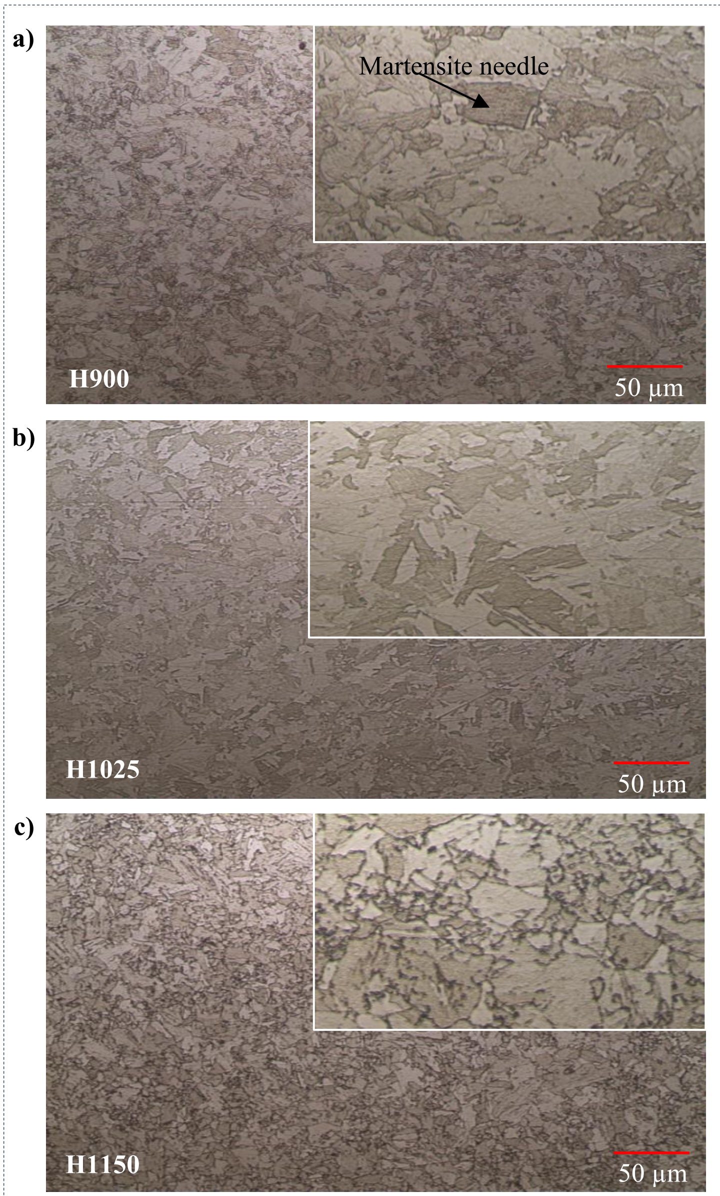

Figure 2.7: Optical microscopy images of the microstructure of the material after different aging treatment: (a) H900, (b) H1025, and (c) H1150.

The stabilization occurs primarily because the powder bed reaches a point where it is already fully melted and consolidated. Additional energy input no longer contributes to further pore elimination but can instead introduce new porosity types—especially keyhole porosity—due to vaporization and recoil pressure effects. In LPBF, when the energy input is too high, it creates deep, narrow keyholes that become unstable and trap gas bubbles, which solidify as porosity upon cooling. This behavior has been observed in our study, where samples processed above optimal VED ranges did not show significant improvement in relative density despite increased energy input.

Moreover, elevated VED leads to higher peak temperatures and larger melt pools, increasing thermal gradients and potentially causing unstable Marangoni convection. These thermal instabilities can promote pore formation by trapping gases or disturbing the melt pool solidification dynamics. Consequently, the process reaches a saturation point where relative density no longer improves and may even decrease due to defect formation.

In this study no plateau or decrease is observed, as all VED values remain within the optimal processing window, avoiding excessive thermal input. The absence of stabilization is attributed to the fact that the maximum VED used does not exceed the threshold where keyhole-mode melting, or vaporization-induced porosity typically occurs [32].

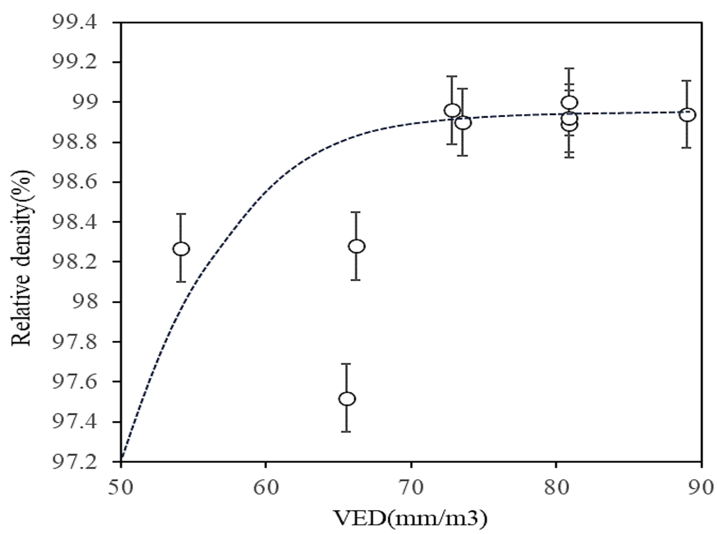

Figure 2.8: Relative density VS VED.

2.2.4.2 Mechanical properties

The experimental results, including UTS, YS, and El, are presented in Table 2.5. Increasing the aging temperature leads to a reduction in UTS and an increase in El, while YS remains relatively stable across all conditions. Specifically, for H900, UTS ranges from 1226.71 to 1314.61 MPa with El between 16.23% and 18.62%. At H1025, UTS decreases to 1058.89–1074.05 MPa and El increases to 19.56–21.12%. Under H1150, UTS further declines to 929.56–946.29 MPa, with El reaching the highest values, ranging from 20.55% to 23.13%. These trends are consistent with the known response of 17-4 PH to aging, where higher temperatures promote precipitate coarsening and softening, thereby reducing strength but enhancing ductility. Cu-rich and NbC precipitates, which form during aging, become less effective in dislocation pinning as they coarsen at elevated temperatures, particularly at 620 °C (H1150), leading to a softer matrix and improved plastic deformation capabilities [33].

Table 2.5: Tensile test results.

	UTS (MPa)	**YS (MPa)**	**Elongation (%)**
S1	1314.61±4.96	1082.9±23.73	18.615±0.365
S2	1058.893±5.355	949.4±16.77	19.56±0.32
S3	929.56±6.05	836.08±16.95	21.8±0.75
S4	936.053±2.452	842.407±13.666	23.133±1.045
S5	1226.71±4.995	1036.34±15.634	17.13±2.061
S6	1074.047±4.198	938.227±2.806	21.123±2.162
S7	1088.567±2.629	923.427±27.969	20.55±1.49
S8	946.293±0.75	832.963±16.142	22.837±1.376
S9	1226.97±3.109	1044.813±17.632	16.23±0.56

As shown in Figure 2.9, the tensile curves for each post-processing heat treatment condition (H900, H1025, H1150) exhibit distinct plastic deformation characteristics, most notably the presence of a plasticity plateau. This plateau, characterized by a nearly constant stress following the elastic limit, reflects the material's ability to undergo plastic deformation with minimal strain hardening.

The extent of the plateau varies with aging temperature. As seen in Figure 2.9-(a), at H900, the plateau is short or nearly absent, followed by a clear strain hardening region. In Figure 2.9-(b), corresponding to H1025, the plateau becomes more evident and extends over a longer strain range. Finally, in Figure 2.9-(c) (H1150), a pronounced and extended plateau is consistently observed across all three samples, indicating stable plastic flow. This trend strongly correlates with the microstructural observations. At H900, the microstructure consists of finely dispersed precipitates and a higher density of dislocations, which favor strain hardening and suppress plateau formation. In contrast, at H1150, the microstructure reveals significantly coarsened Cu-rich and NbC precipitates, as well as evidence of reversed austenite. These features reduce dislocation pinning and enable stress-assisted martensitic transformation, collectively promoting the extended plasticity plateau.

Notably, such plateau behavior has been extensively analyzed in LPBF 17-4 PH stainless steels, where a unique three-stage plastic deformation mechanism has been reported: (I) a yield plateau caused by local plastic instability, (II) rapid work hardening due to strain-induced martensitic transformation (SIMT), and (III) final necking [34]. The initial plateau arises due to limited strain hardening in the ultrafine dislocation cell structure, promoting Lüders band formation. These deformation bands advance until sufficient mechanical energy triggers SIMT, thereby increasing the hardening rate and delaying fracture. Although retained austenite from the as-built state is significantly reduced by solution annealing at 1040 °C, the role of reversed austenite—especially at H1150—should not be neglected. Recent work has shown that reversed austenite formed during aging can transform under applied stress and enhance ductility, consistent with transformation-induced plasticity (TRIP) mechanisms [35]. Hence, the observed plasticity plateau in this study likely results from a combination of precipitate coarsening, limited dislocation hardening, and stress-induced martensitic transformation of reversed austenite.

Each aging condition includes three samples processed under varying VED levels. While the mechanical properties are predominantly influenced by aging temperature, subtle differences in plateau behavior within each group suggest a secondary effect of VED. At H900, higher VED (e.g., S1) results in a sharper transition to plastic flow, while lower VED samples exhibit a more gradual yield. At H1025, increasing VED correlates with smoother plateau regions, potentially due to reduced porosity and a more homogeneous microstructure. For H1150, the plateau behavior appears less sensitive to VED, likely because thermal effects dominate microstructural evolution, homogenizing the mechanical response.

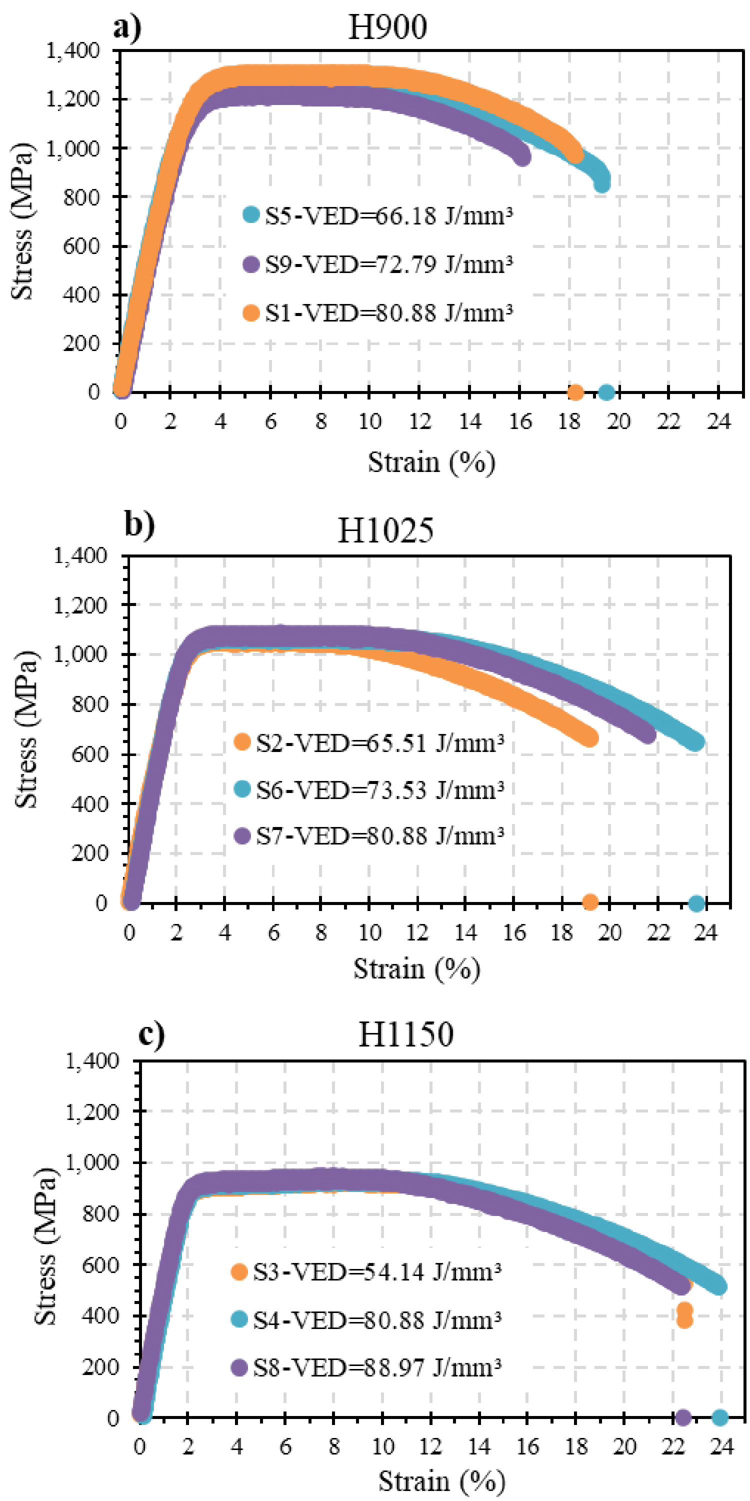

Figure 2.9: Tensile curve at 3 different conditions: a) H900, b) H1025, and c) H1150.

2.2.4.3 Fractography

The fractography analysis of 17-4 PH stainless steel samples subjected to different heat treatment conditions H900, H1025, and H1150 are given in Figure 2.10 to Figure 2.12 respectively. Figure 2.10 shows the fractured surface at the H900 condition for different VED levels, ranging from 66.18 J/mm³ in Figure 2.10-(a) to 80.88 J/mm³ in Figure 2.10-(c). Failure under tensile stress. This brittleness is closely associated with the fine precipitates formed during aging at the lower H900 condition, which increasing strength but loosing ductility. With higher magnification, while VED increased from 72.79 J/mm³ for S9 up to 80.88 J/mm³ for S1, the fractures were less sudden, and consequently, fracture surfaces were smoother. This may again be associated with the reduction in the content of either retained austenite or porosity. Fractography of S1 shows larger and more defined cleavage facets, indicating greater brittleness. S5 and S9 have slightly lower VED values, and their failure modes are also brittle with intergranular cracks; however, their mechanical properties are slightly lower compared to S1. The reduced VED may have introduced some microstructural defects; however, the H900 treatment still resulted in a primarily brittle behavior.

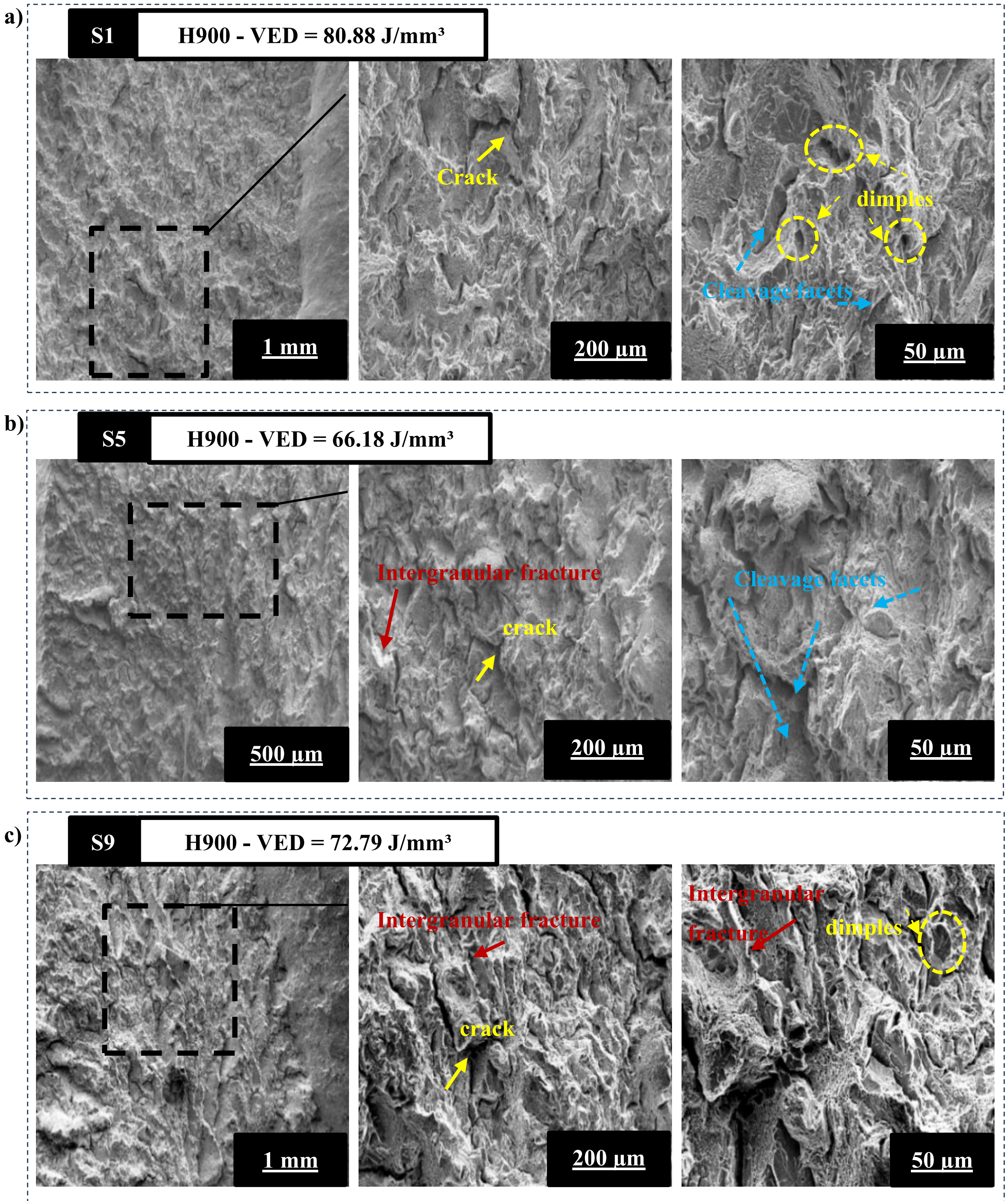

Figure 2.10: SEM images of the fracture surfaces of treated samples at H900.

The fracture surfaces of samples aged at H1025 condition is shown in Figure 2.11. Low magnification at all VED ranges in Figure 2.11-(a) to Figure 2.11-(c) show a combination of ductile and strength characteristics. This duality is demonstrated by the presence of both dimples and cleavage facets or intergranular fractures at lower magnifications, indicating a balanced mechanical performance with a relatively high UTS, YS, and HRC along with appropriate ductility. S2 displays a balanced fractography with a combination of dimples and cleavage facets. The moderate VED and intermediate aging temperature generally resulted in a refined microstructure that balances strength and ductility. S6 exhibits a more ductile fracture mode with larger dimples, most likely due to the reduced laser power and optimal scan speed, which encouraged sufficient fusion and a homogeneous microstructure. While exhibiting more brittle features such as intergranular fractures, the mechanical properties of S7 indicate a small bias toward strength over ductility, but without the degree of brittleness seen in H900-treated samples. This mix of fracture features in the H1025-treated samples represents a transitional state, where processing and heat treatment parameters are finely tuned to achieve a compromise between high strength and adequate ductility, making these conditions suitable for applications where both properties are required.

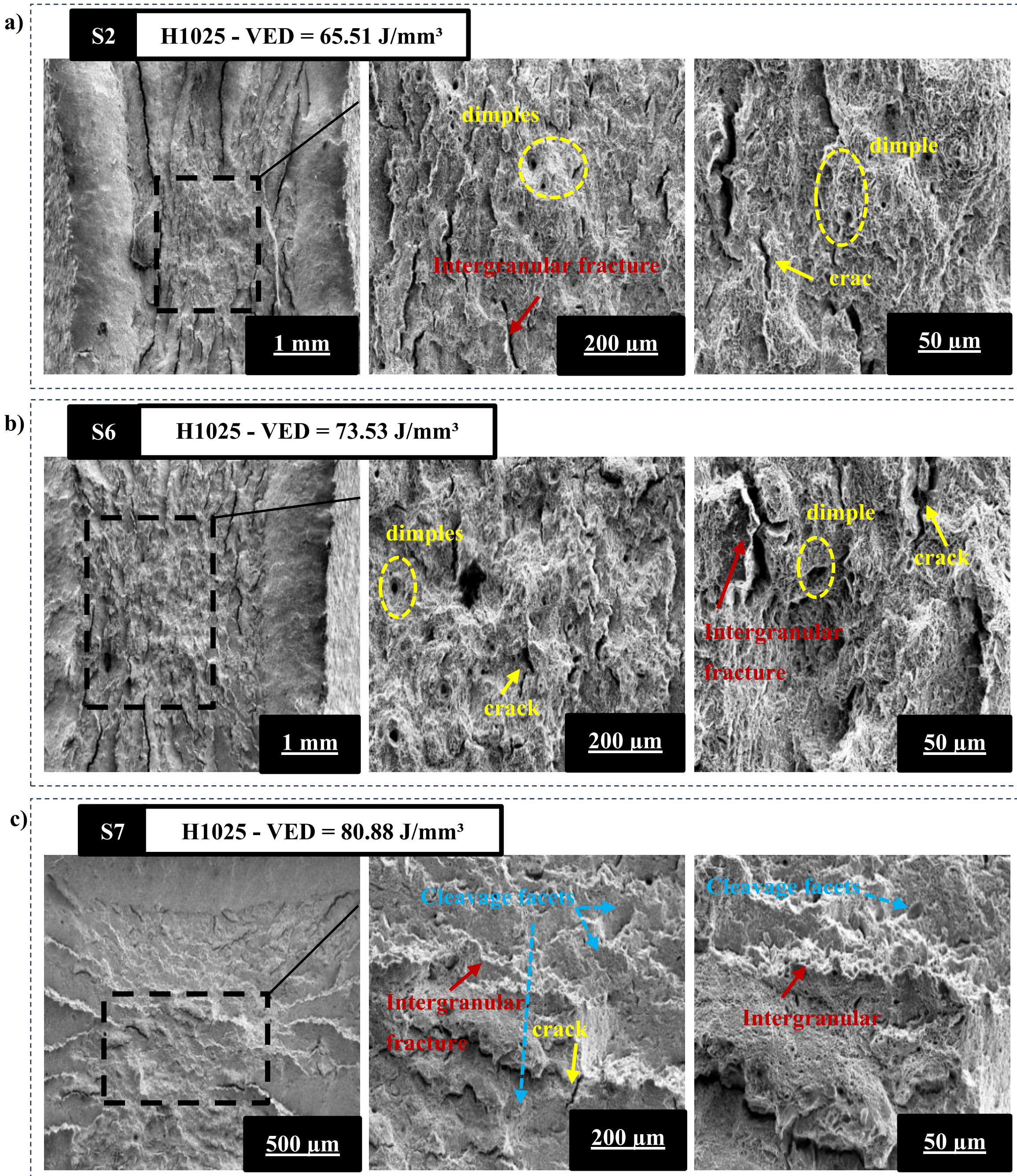

Figure 2.11: SEM images of the fracture surfaces of treated samples at H1025.

The fractures surfaces of samples aged at H1150 condition is given in Figure 2.12. A highly ductile fracture characteristics is observed at low magnification. The fracture surfaces have huge dimples with apparent gas porosities, which correspond to the lower UTS, YS, and HRC values.

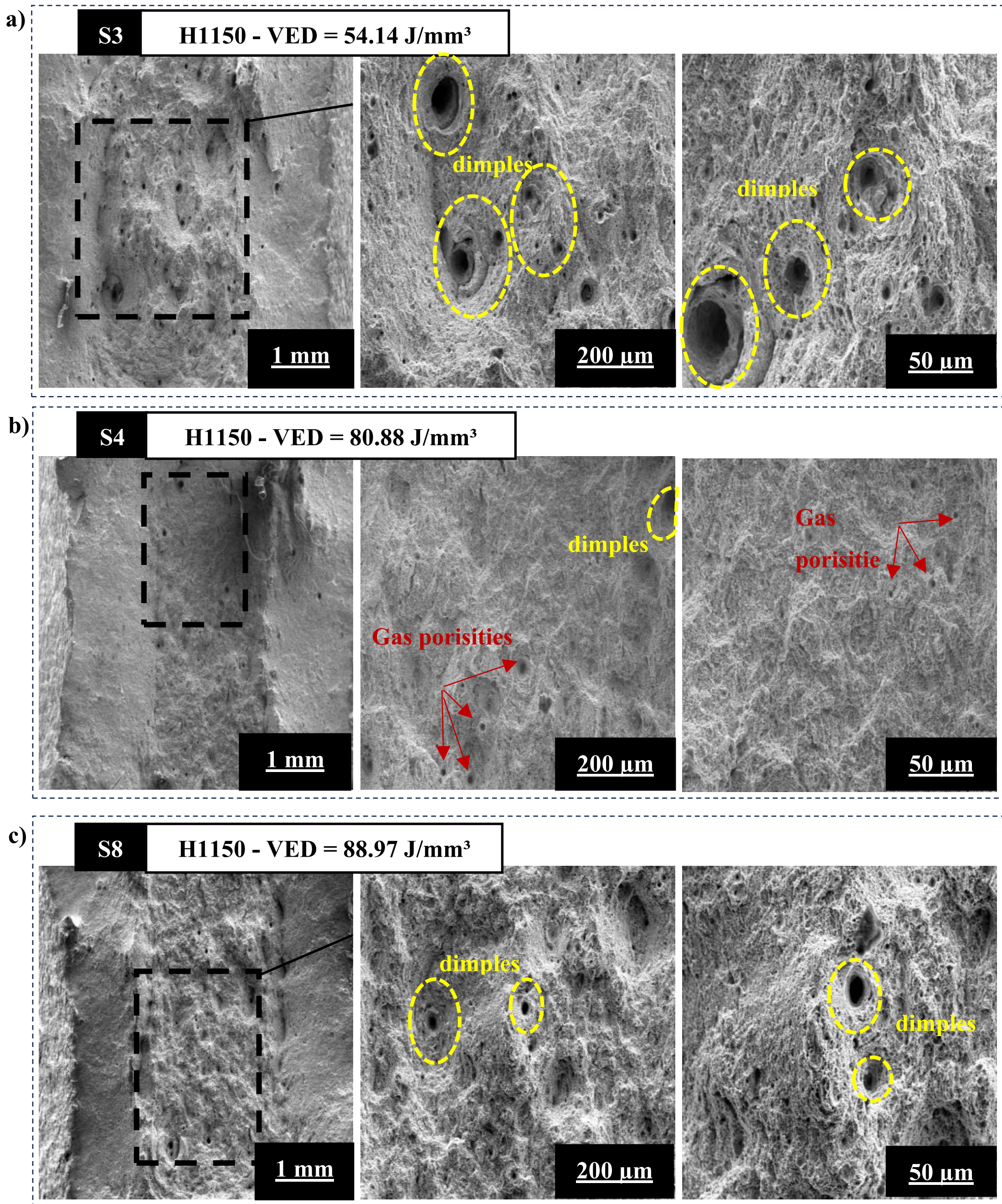

Figure 2.12: SEM images of the fracture surfaces of treated samples at H1150.

S3 exhibits prominent dimpled structures with obvious porosities, indicating a highly ductile fracture process. The low VED used in this sample resulted in a less cohesive microstructure, which is evident in its lower mechanical properties. S4 has high gas porosities and a significant decrease in mechanical strength. The high scan speed and extended hatch distance possibly resulted in insufficient energy input, increasing these effects.

S8 has a more balanced structure but still tends toward ductility, with apparent dimples reflecting its mechanical properties. These features are slightly better to S3 and S4, most likely due to more optimized LPBF parameters. The H1150 condition gives rise to a much more ductile material but reduces strength and hardness at the same time. Such is in correspondence with the microstructural alterations due to the high-temperature aging, such as the softening effect along grain boundaries and coarsening of the precipitates-which favored plastic deformation over resistance to fracture.

2.2.4.4 Statistical analysis

Main effect plots driven from ANOVA analysis is given in Figure 2.13, Figure 2.15 and Figure 2.14. Figure 2.13-a to Figure 2.13-d shows the individual effect of each parameter on the UTS value, shows the maximum effective parameters is aging temperature. Figure 2.15-a) to Figure 2.15-d), shows the individual effect of each parameter on the elongation.

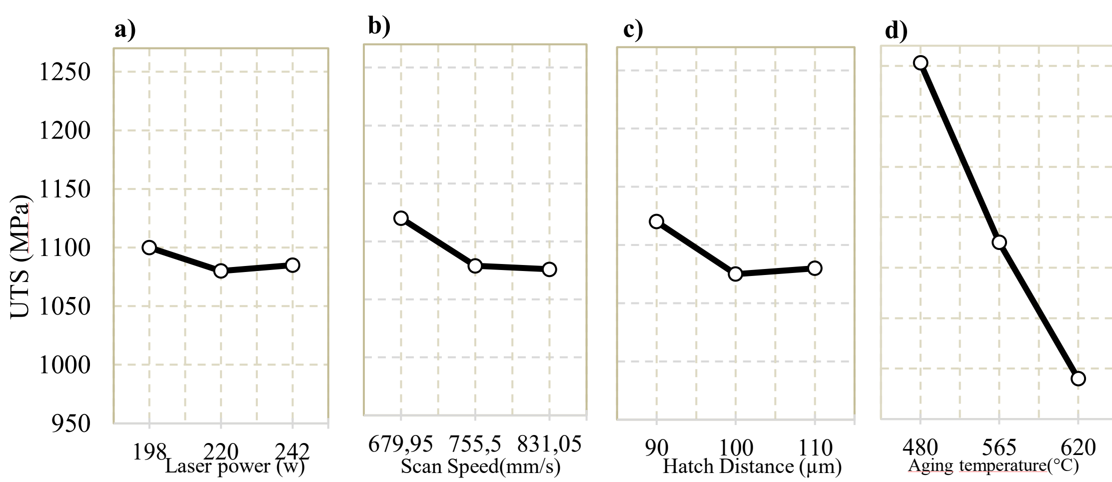

Figure 2.13: Effect of a) laser power, b) scan speed, c) hatch distance and d) aging temperature on UTS.

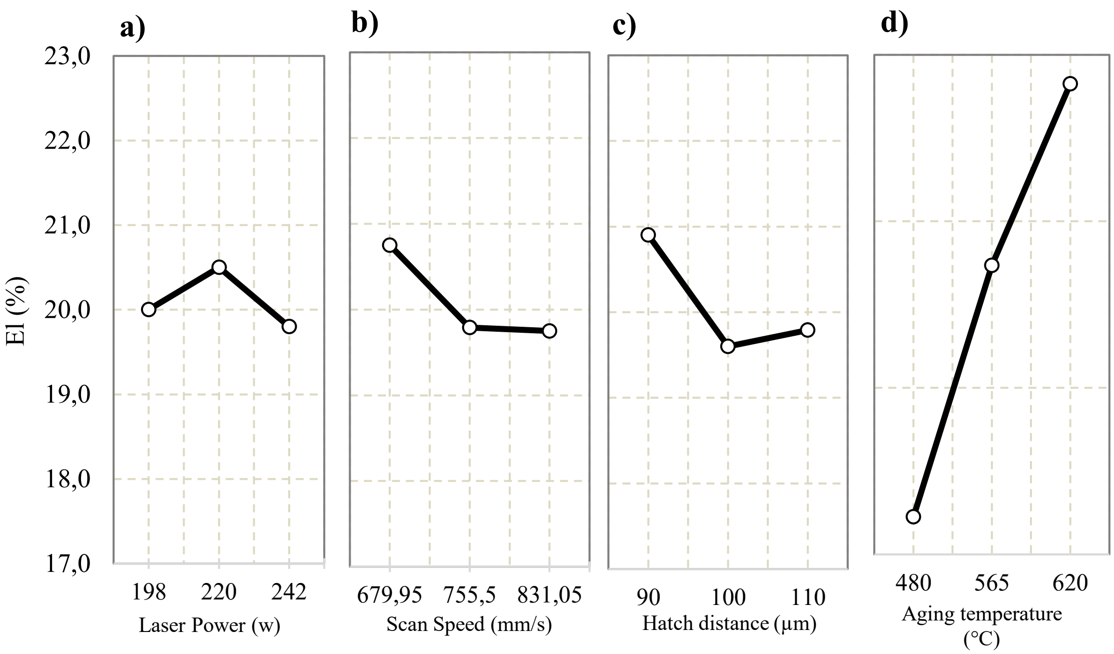

Figure 2.15: Effect of a) laser power, b) scan speed, c) hatch distance and d) aging temperature on Elongation.

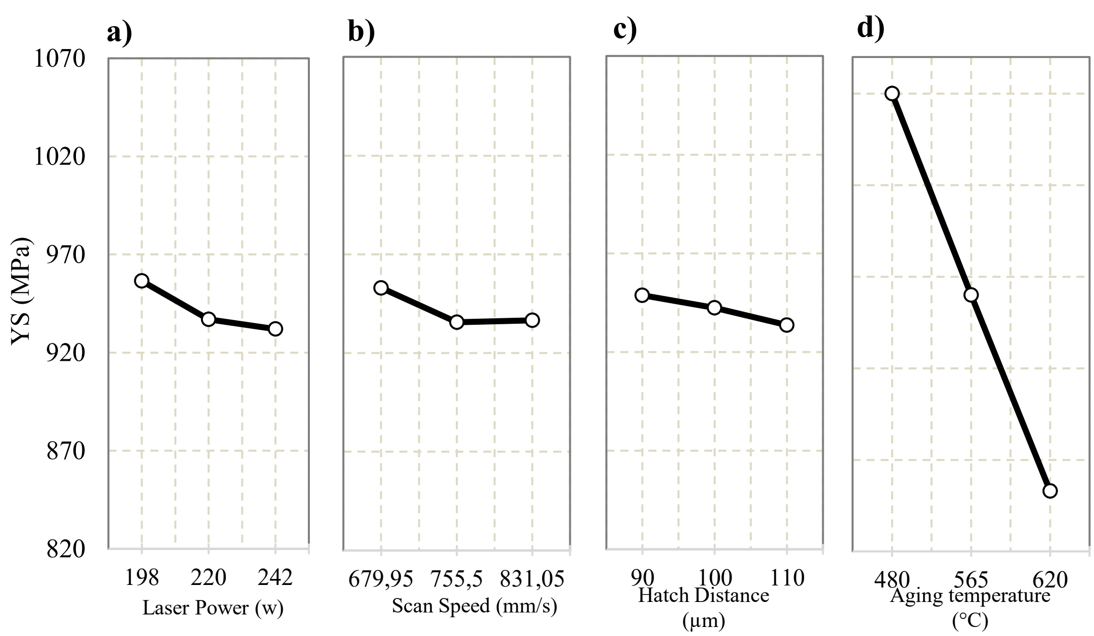

Figure 2.14: Effect of a) laser power, b) scan speed, c) hatch distance and d) aging temperature on YS.

In this case, the effect of the processing parameters is more pronounced compared to the UTS, indicating the elongation is strongly affected by manufacturing defects, which also has been presented in the experimental results. The analysis shows that the mid-range of the laser power 220W, minimum scanning speed, and minimum hatch space possibly results in higher elongation. Very low laser power results in weak bonding and very high laser power results in keyhole formation. Low levels of hatching space (90μm) and laser speed (679.95 mm/s) avoid weak bonding also. These manufacturing defects including keyhole, and weak bonding created stress concentration corners and makes material more susceptible for crack formation and propagation. Yet, the aging temperature is the most contributor factor in the elongation due to the pronounced effect of the carbide precipitates in this material.

Figure 2.14-a) to Figure 2.14-d) shows the individual effect of each parameter on the yield stress in which the effect of the processing parameters is approximately negligible. It could be concluded that YS is mainly controlled by the aging temperature and follows the same trend as the UTS.

The effect of each parameter, is calculated with ANOVA analysis and presented with percentage of the contribution in Table 2.6, Table 2.7 and Table 2.8. The results show the aging temperature contribute 96.20% and 94.04% on the UTS and YS respectively and 75.41% on the elongation.

To ensure consistency between statistical and visual analyses, the Mean Effects Charts (Figure 2.13–Figure 2.14) are interpreted alongside the corresponding ANOVA tables (Table 2.6–Table 2.8). This comparison highlights how each processing parameter affects mechanical properties and confirms the dominant role of aging temperature.

For UTS, the Mean Effects Chart (Figure 2.13) clearly demonstrates that aging temperature has the most pronounced influence, with a sharp increasing trend. The other parameters—laser power, scan speed, and hatch distance—show relatively flat curves, indicating minimal impact. This visual interpretation aligns well with the ANOVA results in Table 2.6, where aging temperature accounts for 96.20% of the total contribution and is highly significant ($p < 0.001$). Although scan speed (1.17%, $p = 0.001$) and hatch distance (0.79%, $p = 0.004$) show minor but statistically significant effects, laser power contributes only 0.17% and is not statistically significant ($p = 0.152$). The agreement between the visual trend and statistical data confirms that UTS is primarily governed by the aging temperature.

A similar trend is observed for YS. In Figure 2.14, aging temperature shows the steepest curve among all variables, indicating its dominant effect. This is supported by the ANOVA in Table 2.7, where it contributes 94.04% to the variation and is statistically significant ($p < 0.001$). Laser power contributes 1.38% and reaches significance ($p = 0.010$), whereas scan speed (0.14%, $p = 0.372$) and hatch distance (0.65%, $p = 0.064$) do not exhibit statistically meaningful effects. These findings reinforce that, as with UTS, aging temperature is the primary factor controlling YS, with a minor secondary role for laser power. In the case of elongation, the Mean Effects Chart (Figure 2.15) suggests more noticeable variability across multiple parameters compared to UTS and YS. Specifically, laser power, scan speed, and hatch distance all show slight fluctuations, suggesting a potential influence on ductility. However, Table 2.8 shows that statistically, aging temperature still dominates, contributing 75.41% with a highly significant p-value ($p < 0.001$). The other parameters contribute between 0.05% and 2.11% and are not statistically significant (p-values ranging from 0.145 to 0.817). This apparent mismatch between the chart and statistical significance may result from the greater sensitivity of elongation to microstructural inhomogeneities and manufacturing defects—such as porosity, lack of fusion, or residual stress—which are more likely to influence ductility than strength. These localized defects can introduce scatter in the experimental results that may not be well captured by the model. Nevertheless, the results confirm that aging temperature remains the most influential factor for elongation, although its dominance is somewhat reduced compared to UTS and YS.

Table 2.6: Regression analysis for UTS.

Source	DF	Seq SS	Contribution	Adj SS	Adj MS	F-Value	P-Value
Regression	4	467165	98.33%	467165	116791	323.33	0.000
Laser power	1	797	0.17%	797	797	2.21	0.152
Scan speed	1	5543	1.17%	5543	5543	15.35	0.001
Hatch distance	1	3763	0.79%	3763	3763	10.42	0.004
Aging temperature	1	457061	96.20%	457061	457061	1265.37	0.000
Error	22	7947	1.67%	7947	361		
Lack of fit	4	7536	1.59%	7536	1884	82.55	0.000
Pure Error	18	411	0.09%	411	23		
Total	26	475112	100.00%				

Table 2.7: Regression analysis for YS.

Source	DF	Seq SS	Contribution	Adj SS	Adj MS	F-Value	P-Value
Regression	4	213698	96.21%	213698	53424	139.76	0.000
Laser power	1	3071	1.38%	3071	3071	8.03	0.010
Scan speed	1	317	0.14%	317	317	0.83	0.372
Hatch distance	1	1448	0.65%	1448	1448	3.79	0.064
Aging temperature	1	208861	94.04%	208861	208861	546.37	0.000
Error	22	8410	3.79%	8410	382		
Lack-of-Fit	4	2138	0.96%	2138	535	1.53	0.235
Pure Error	18	6272	2.82%	6272	348		
Total	26	222108	100.00%				

Table 2.8: Regression analysis for Elongation.

Source	DF	Seq SS	Contribution	Adj SS	Adj MS	F-Value	P-Value
Regression	4	0.014034	79.61%	0.014034	0.003509	21.47	0.000
Laser power	1	0.000009	0.05%	0.000009	0.000009	0.05	0.817
Scan speed	1	0.000373	2.11%	0.000373	0.000373	2.28	0.145
Hatch distance	1	0.000359	2.04%	0.000359	0.000359	2.20	0.152
Aging temperature	1	0.013293	75.41%	0.013293	0.013293	81.35	0.000
Error	22	0.003595	20.39%	0.003595	0.000163		
Lack of fit	4	0.000482	2.73%	0.000482	0.000120	0.70	0.605
Pure Error	18	0.003113	17.66%	0.003113	0.000173		
Total	26	0.017629	100.00%				

Regression modes are driven from the ANOVA analysis. Equation (2) shows the regression model for UTS, YS and El respectively elongation. To evaluate the predictive performance and reliability of these models, correlation plots comparing the experimental and predicted values are shown in Figure 2.16-(a–c). These plots demonstrate a strong alignment of data points along the 45° reference line, indicating a high level of predictive accuracy. The coefficients of determination were found to be $R^2 = 0.985$ for UTS, $R^2 = 0.9919$ for YS, and $R^2 = 0.9294$ for elongation, highlighting the strength of the model fits. Additionally, residual errors for each property are summarized in Figure 2.16-(d), showing low and randomly distributed deviations, which confirms the appropriateness of the linear regression approach.

$$\begin{bmatrix} \text{UTS (MPa)} \\ \text{YS (MPa)} \\ \text{El(\%)} \end{bmatrix} = \begin{bmatrix} 2729.4 & -0.303 & -0.2323 & -1.446 & -2.2592 \\ 2054.1 & -0.594 & -0.0556 & -0.897 & -1.5272 \\ 0.0845 & -0.000032 & -0.00006 & -0.000447 & 0.000385 \end{bmatrix} \times \begin{bmatrix} 1 \\ \text{Laser power} \\ \text{Scan speed} \\ \text{Hatch distance} \\ \text{Aging temperature} \end{bmatrix}$$

Equation (2)

For UTS, the regression coefficient was statistically significant ($p < 0.001$), and comparable significance is expected for YS and EL given their high R^2 values and consistent residual behavior. These statistical indicators collectively confirm the robustness and reliability of the developed models, consistent with widely accepted practices for assessing predictive performance in materials modeling, as exemplified in recent literature [36].

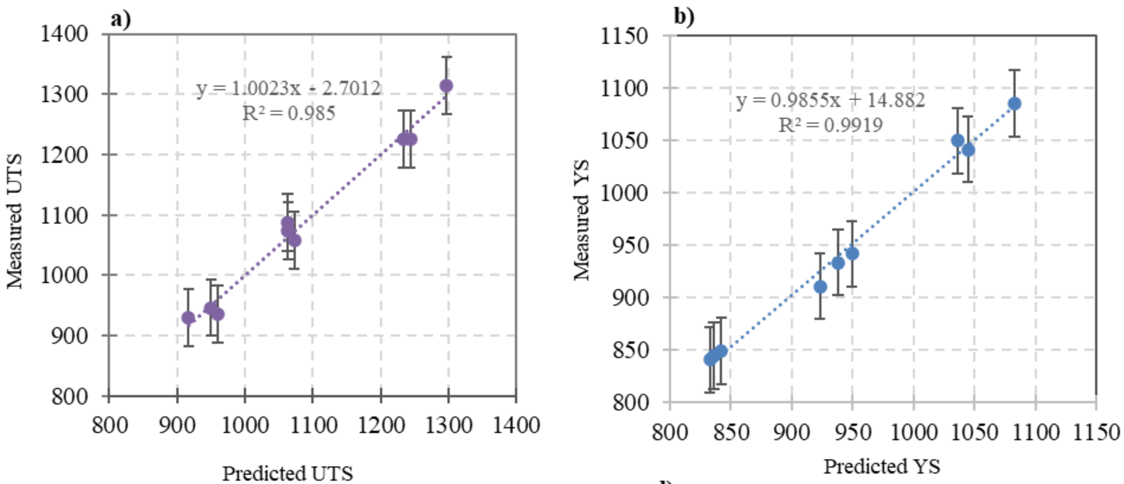

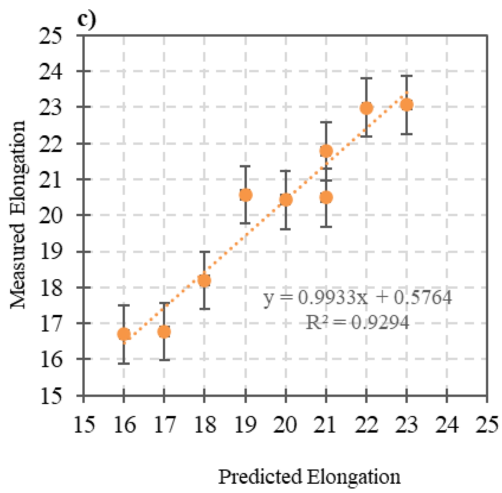

d)

sample	Residual Error (UTS)	Residual Error (YS)	Residual Error (Elongation)
1	1.30	0.18	1.08
2	1.40	0.79	8.24
3	1.34	1.04	3.73
4	2.51	0.79	0.29
5	1.45	1.29	1.32
6	1.01	0.49	2.43
7	2.33	1.34	2.16
8	0.39	0.94	4.50
9	0.65	0.33	4.37

Figure 2.16: Correlation between Predicted and Measured Mechanical Properties (a) Ultimate Tensile Strength (UTS), (b) Yield Strength (YS), (c) Elongation and (d) residual error.

2.2.5 Conclusion

This study examines how LPBF processing parameters—laser power, scanning speed, hatch distance, and volumetric energy density (VED)—as well as aging temperature, affect the microstructure and mechanical properties of 17-4 PH stainless steel. The results show that solution treatment at 1040°C helps to make the microstructure more uniform and eliminates inhomogeneities in the as-built condition. After aging under different conditions (H900, H1025, H1150), the microstructure remains similar, with only small changes observed in response to different processing parameter combinations. These changes are small enough not to significantly affect the tensile properties like UTS and YS. However, processing parameters have a greater impact on elongation by controlling manufacturing defects.

Overall, the study concludes that within a VED range of 70 – 90 J/mm^3, manufacturing defects are minimal, and the processing parameters have little effect on UTS, YS, or elongation. Within this VED range, the material is reliable for manufacturing, and its mechanical properties can be accurately predicted using the regression models presented.

2.2.6 Declaration Statements

a. Funding: Not applicable
b. Conflicts of interest/Competing interests: The authors declare that there are no conflicts of interest/competing interests regarding the publication of this manuscript.
c. Availability of data and material: Not applicable.
d. Code availability: Not applicable.
e. Ethics approval: Not applicable.
f. Authors' contributions:
g. Consent to participate: Not applicable.
h. Consent for publication: Not applicable

2.2.7 References

[1] H. R. Lashgari, M. Ferry, and S. Li, 'Additive manufacturing of bulk metallic glasses: Fundamental principle, current/future developments and applications', *Journal of Materials Science & Technology*, vol. 119, pp. 131–149, Aug. 2022, doi: 10.1016/j.jmst.2021.09.068.

[2] M. Srivastava and S. Rathee, 'Additive manufacturing: recent trends, applications and future outlooks', *Prog Addit Manuf*, vol. 7, no. 2, pp. 261–287, Apr. 2022, doi: 10.1007/s40964-021-00229-8.

[3] C. Meier, R. W. Penny, Y. Zou, J. S. Gibbs, and A. J. Hart, 'THERMOPHYSICAL PHENOMENA IN METAL ADDITIVE MANUFACTURING BY SELECTIVE LASER MELTING: FUNDAMENTALS, MODELING, SIMULATION, AND EXPERIMENTATION', *Annual Rev Heat Transfer*, vol. 20, no. 1, pp. 241–316, 2017, doi: 10.1615/AnnualRevHeatTransfer.2018019042.

[4] S. Sabooni *et al.*, 'Laser powder bed fusion of 17–4 PH stainless steel: A comparative study on the effect of heat treatment on the microstructure evolution and mechanical

properties', *Additive Manufacturing*, vol. 46, p. 102176, Oct. 2021, doi: 10.1016/j.addma.2021.102176.

[5] A. Ozsoy, E. B. Tureyen, M. Baskan, and E. Yasa, 'Microstructure and mechanical properties of hybrid additive manufactured dissimilar 17-4 PH and 316L stainless steels', *Materials Today Communications*, vol. 28, p. 102561, Sep. 2021, doi: 10.1016/j.mtcomm.2021.102561.

[6] N. Omidi, M. Houria, M. M. Monjez, M. Jahazi, N. Barka, and A. E. Ouafi, 'Processing parameters optimization for enhanced mechanical strength in PBF-ed H13 tool steel: minimizing manufacturing defects including microstructural inhomogeneity, sub-surface porosities, and oxide formation', *Int J Adv Manuf Technol*, vol. 136, no. 5–6, pp. 2681–2706, Jan. 2025, doi: 10.1007/s00170-024-14951-4.

[7] C. Kisraoui *et al.*, 'Effect of Printing Strategies on Mechanical Properties of Tool Steel in Laser Powder Bed Fusion Process', *Lasers Manuf. Mater. Process.*, vol. 12, no. 1, pp. 147–173, Mar. 2025, doi: 10.1007/s40516-025-00275-y.

[8] N. C. Igwe, I. Akhrif, M. El Jai, and B. El Fahime, 'An experimental investigation of the influence of SLM input factors on the as-built AlSi10Mg surface quality', *Int J Adv Manuf Technol*, vol. 136, no. 2, pp. 619–674, Jan. 2025, doi: 10.1007/s00170-024-14657-7.

[9] N. C. Igwe, I. Akhrif, and M. E. Jai, 'Failure modes analysis and assessment of aluminum-based metallic matrix composites printed with LPBF technology', *Int J Adv Manuf Technol*, vol. 138, no. 7–8, pp. 3621–3647, Jun. 2025, doi: 10.1007/s00170-025-15722-5.

[10] D. J. Shaffer, A. E. Wilson-Heid, J. S. Keist, A. M. Beese, and T. A. Palmer, 'Impact of retained austenite on the aging response of additively manufactured 17-4 PH grade stainless steel', *Materials Science and Engineering: A*, vol. 817, p. 141363, Jun. 2021, doi: 10.1016/j.msea.2021.141363.

[11] M. R. Stoudt, C. E. Campbell, and R. E. Ricker, 'Examining the Relationship Between Post-Build Microstructure and the Corrosion Resistance of Additively Manufactured 17-4PH Stainless Steel', *Materialia*, vol. 22, p. 101435, May 2022, doi: 10.1016/j.mtla.2022.101435.

[12] L. Huang, Y. Cao, H. Zhao, Y. Li, Y. Wang, and L. Wei, 'Effect of process parameters on density and mechanical behaviour of a selective laser melted 17-4PH stainless steel alloy', *Open Physics*, vol. 20, no. 1, pp. 66–77, Feb. 2022, doi: 10.1515/phys-2022-0008.

[13] P. Ponnusamy *et al.*, 'A study of tensile behavior of SLM processed 17-4 PH stainless steel', *Materials Today: Proceedings*, vol. 45, pp. 4531–4534, 2021, doi: 10.1016/j.matpr.2020.12.1104.

[14] H. Irrinki *et al.*, 'Effects of Powder Attributes and Laser Powder Bed Fusion (L-PBF) Process Conditions on the Densification and Mechanical Properties of 17-4 PH Stainless Steel', *JOM*, vol. 68, no. 3, pp. 860–868, Mar. 2016, doi: 10.1007/s11837-015-1770-4.

[15] C. Li, Y. Chen, X. Zhang, T. Liu, Y. Peng, and K. Wang, 'Effect of heat treatment on microstructure and mechanical properties of 17-4PH stainless steel manufactured by

laser-powder bed fusion', *Journal of Materials Research and Technology*, vol. 26, pp. 5707–5715, Sep. 2023, doi: 10.1016/j.jmrt.2023.08.283.
[16] M. A. Aripin *et al.*, 'Microstructure and mechanical properties of selective laser melted 17–4 PH stainless steel; Build direction and heat treatment processes', *Materials Today Communications*, vol. 36, p. 106479, Aug. 2023, doi: 10.1016/j.mtcomm.2023.106479.
[17] Y. H. Kim, M. K. Kim, J. Suhr, T. Lee, and M. K. Kim, 'Exploring the Effect of Heat Treatment on the Mechanical Performance of 17-4PH Stainless Steel Specimens Fabricated by Metal Additive Manufacturing', *Exp Mech*, vol. 64, no. 8, pp. 1333–1342, Oct. 2024, doi: 10.1007/s11340-024-01089-3.
[18] D. Basu, Z. Wu, J. L. L. Meyer, E. Larson, R. Kuo, and A. Rollett, 'Entrapped Gas and Process Parameter-Induced Porosity Formation in Additively Manufactured 17-4 PH Stainless Steel', *J. of Materi Eng and Perform*, vol. 30, no. 7, pp. 5195–5202, Jul. 2021, doi: 10.1007/s11665-021-05695-3.
[19] A. K. Dutt, G. K. Bansal, S. Tripathy, K. Gopala Krishna, V. C. Srivastava, and S. Ghosh Chowdhury, 'Optimization of Selective Laser Melting (SLM) Additive Manufacturing Process Parameters of 316L Austenitic Stainless Steel', *Trans Indian Inst Met*, Jul. 2022, doi: 10.1007/s12666-022-02687-2.
[20] H. K. Rafi, D. Pal, N. Patil, T. L. Starr, and B. E. Stucker, 'Microstructure and Mechanical Behavior of 17-4 Precipitation Hardenable Steel Processed by Selective Laser Melting', *J. of Materi Eng and Perform*, vol. 23, no. 12, pp. 4421–4428, Dec. 2014, doi: 10.1007/s11665-014-1226-y.
[21] D. Gonzalez-Nino, T. Strasser, and G. S. Prinz, 'Ultra Low-Cycle Fatigue Behavior Comparison between Additively Manufactured and Rolled 17-4 PH (AISI 630) Stainless Steels', *Metals*, vol. 11, no. 11, p. 1726, Oct. 2021, doi: 10.3390/met11111726.
[22] V. Alfieri, V. Giannella, F. Caiazzo, and R. Sepe, 'Influence of position and building orientation on the static properties of LPBF specimens in 17-4 PH stainless steel', *Forces in Mechanics*, vol. 8, p. 100108, Aug. 2022, doi: 10.1016/j.finmec.2022.100108.
[23] M. A. Aripin *et al.*, 'Microstructure and mechanical properties of selective laser melted 17–4 PH stainless steel; Build direction and heat treatment processes', *Materials Today Communications*, vol. 36, p. 106479, Aug. 2023, doi: 10.1016/j.mtcomm.2023.106479.
[24] H. R. Lashgari, C. Kong, E. Adabifiroozjaei, and S. Li, 'Microstructure, post thermal treatment response, and tribological properties of 3D printed 17-4 PH stainless steel', *Wear*, vol. 456–457, p. 203367, Sep. 2020, doi: 10.1016/j.wear.2020.203367.
[25] N. Nayan *et al.*, 'Metallurgical Analysis of Lower Mechanical Property in 17-4PH Steel: A Comprehensive Study', *J Fail. Anal. and Preven.*, vol. 24, no. 3, pp. 1221–1229, Jun. 2024, doi: 10.1007/s11668-024-01910-0.
[26] I. Vysotskiy, S. Malopheyev, I. Zuiko, S. Mironov, and R. Kaibyshev, 'Crystallographic aspects of 17–4 PH martensitic steel produced by laser-powder bed fusion', *Materials Characterization*, vol. 194, p. 112405, Dec. 2022, doi: 10.1016/j.matchar.2022.112405.
[27] T.-H. Hsu *et al.*, 'Effect of processing parameters on the fractions of martensite in 17-4 PH stainless steel fabricated by selective laser melting', *Journal of Alloys and Compounds*, vol. 859, p. 157758, Apr. 2021, doi: 10.1016/j.jallcom.2020.157758.

[28] D. J. Shaffer, A. E. Wilson-Heid, J. S. Keist, A. M. Beese, and T. A. Palmer, ‘Impact of retained austenite on the aging response of additively manufactured 17-4 PH grade stainless steel’, *Materials Science and Engineering: A*, vol. 817, p. 141363, Jun. 2021, doi: 10.1016/j.msea.2021.141363.

[29] H. Chae *et al.*, ‘Optimization of Aging Temperature and Heat-Treatment Pathways in Additively Manufactured 17-4PH Stainless Steel’, *Materials*, vol. 16, no. 24, p. 7557, Dec. 2023, doi: 10.3390/ma16247557.

[30] G. Yeli, M. A. Auger, K. Wilford, G. D. W. Smith, P. A. J. Bagot, and M. P. Moody, ‘Sequential nucleation of phases in a 17-4PH steel: Microstructural characterisation and mechanical properties’, *Acta Materialia*, vol. 125, pp. 38–49, Feb. 2017, doi: 10.1016/j.actamat.2016.11.052.

[31] K. Fri, I. Akhrif, A. Laazizi, M. El Jai, M. Bensada, and A. Ouannou, ‘Experimental investigation of the effects of processing parameters and heat treatment on SS 316L manufactured by laser powder bed fusion’, *Prog Addit Manuf*, vol. 9, no. 6, pp. 1787–1809, Dec. 2024, doi: 10.1007/s40964-023-00538-0.

[32] K. Fri *et al.*, ‘Microstructural and heat treatment analysis of 316L elaborated by SLM additive manufacturing process’, *Int J Adv Manuf Technol*, vol. 124, no. 7–8, pp. 2289–2297, Feb. 2023, doi: 10.1007/s00170-022-10622-4.

[33] D. Dong *et al.*, ‘Influence of Aging Treatment Regimes on Microstructure and Mechanical Properties of Selective Laser Melted 17-4 PH Steel’, *Micromachines*, vol. 14, no. 4, p. 871, Apr. 2023, doi: 10.3390/mi14040871.

[34] D. Zhao *et al.*, ‘Abnormal three-stage plastic deformation in a 17-4 PH stainless steel fabricated by laser powder bed fusion’, *Materials Science and Engineering: A*, vol. 858, p. 144160, Nov. 2022, doi: 10.1016/j.msea.2022.144160.

[35] H. Chae *et al.*, ‘Optimization of Aging Temperature and Heat-Treatment Pathways in Additively Manufactured 17-4PH Stainless Steel’, *Materials*, vol. 16, no. 24, p. 7557, Dec. 2023, doi: 10.3390/ma16247557.

[36] K. Ouazzani, I. Akhrif, N. Rihani, M. El Jai, M. Radouani, and B. El Fahime, ‘Processing Parameters, Heat-Treatment, and Testing Speed influence on Mechanical properties of Additively Manufactured ABS copolymer’, *Moroccan Journal of Chemistry*, vol. 12, no. 4, pp. 1621–1663, Sep. 2024, doi: 10.48317/IMIST.PRSM/MORJCHEM-V12I4.50175.

CHAPITRE 3
ÉTUDE DES PROPRIÉTÉS AUX CHOCS DE L'ACIER INOXYDABLE 17-4 PH FABRIQUÉ PAR FABRICATION ADDITIVE VIA DES ESSAIS CHARPY

3.1 RÉSUMÉ EN FRANÇAIS DU TROISIÈME ARTICLE

Ce chapitre vise à déterminer l'influence des paramètres du procédé de fusion laser sur lit de poudre (LPBF) et des traitements thermiques sur la ténacité de l'acier inoxydable 17-4 PH produit par fabrication additive. Trois températures de vieillissement (480°C - H900, 565°C - H1025, et 620°C - H1150) et plusieurs combinaisons optimisées de paramètres de fabrication (puissance laser, vitesse de balayage, espacement entre passes) ont été évaluées afin d'identifier leur effet sur la résistance à l'impact mesurée par l'essai Charpy. Les résultats obtenus montrent que, bien que les paramètres LPBF affectent significativement la densité, les défauts de fabrication et la cinétique de précipitation du matériau, l'effet du traitement thermique demeure prédominant sur la ténacité finale. Le meilleur compromis entre ténacité et ductilité a été atteint avec un traitement thermique H1150 (620°C), où l'énergie absorbée maximale était de 120 J. Les paramètres optimisés, correspondant à une densité d'énergie volumique (VED) entre 80 et 88,98 J/mm³, permettent d'obtenir une microstructure homogène et une ténacité élevée, comparable aux spécifications recommandées par le fabricant EOS. Cette étude apporte une contribution originale en établissant explicitement le lien entre les mécanismes de fracture observés et les conditions précises de fabrication et de traitement thermique, comblant ainsi une lacune importante dans la littérature scientifique sur le comportement à la rupture de l'acier 17-4 PH fabriqué par LPBF.

Mots clés : Fabrication additive, Test d'impact Charpy, Résistance aux chocs, 17-4 PH.

3.2 INVESTIGATION OF IMPACT PROPERTIES OF 17-4 PH PRODUCED WITH ADDITIVE MANUFACTURING UNDER CHARPY TEST

Yassmine Chedly [1], Narges Omidi [1], Noureddine Barka [1]
[1] Department of Mathematics, Computer Science and Engineering, University of Québec at Rimouski (UQAR), Rimouski, Québec G5L 3A1, Canada.

3.2.1 Abstract

The aging treatment plays a major role in controlling the precipitation kinetics of 17-4 PH stainless steel, significantly influencing its toughness behavior by favoring the formation of the beneficial phases. Additionally, it is needed to optimize processing parameters before the heat treatment in order to influence the microstructure of the material with a good balance between strength and ductility achieved by controlled solidification and phase transformations. This study investigates the effect of LPBF parameters, including laser power, scanning speed, hatch distance and heat treatments (H900, H1025, H1150) on toughness, assessed by Charpy impact testing. Three sets of processing parameters are applied at each aging temperature to investigate their effect on the toughness behavior of the LPBF-process material. The results indicate that LPBF parameters affect the material's density, manufacturing defects, and the kinetics of precipitation, which, in turn, influence its microstructure and toughness, even when the aging treatment is conducted at the same temperature. While solution annealing at 1040°C eliminates microstructural inhomogeneity caused by the LPBF process, the microstructure after heat treatment still remains influenced by the processing parameters. In all cases, the aging treatment at 620°C yielded the highest toughness of 120J, with the effect of aging treatment outweighing that of the processing parameters. Optimized processing parameters, with an energy density (VED) between 80-88.98 J/mm^3 and an aging temperature of 620°C, are recommended based on the EOS machine company's specifications for achieving superior toughness. This research provides novel insights by systematically correlating specific LPBF process parameters and aging

conditions to fracture mechanisms and toughness behavior, filling a critical gap in the existing literature.

Keywords: Additive Manufacturing, 17-4 PH SS, Charpy impact test, heat treatment, toughness, LPBF.

3.2.2 Introduction

Additive manufacturing (AM), or 3D printing, has undergone tremendous advancement in recent years, resulting in paradigm shifts in conventional production processes. Among the numerous additive manufacturing processes, powder bed fusion (PBF) processes have been recognized as pivotal technologies for the production of high-performance metallic components [1]. These technologies are highly beneficial as they can produce complex geometries with high accuracy and low material loss, hence being highly suited for industries such as aerospace, automotive, and medicine [2]. PBF processes, using layer-by-layer, provide high design freedom, lower production time, and the ability to provide customized manufacturing with efficient use of resources and high sustainability [3]. These characteristics collectively unveil AM as a revolutionary intervention for meeting increasingly important requirements of modern industrial applications [4].

17-4 PH stainless steel is a martensitic precipitation-hardening steel alloy well known for its excellent mechanical properties of high strength, excellent corrosion resistance, and superior fatigue resistance [5]. These properties make it eminently suitable for rigorous applications in the aerospace, automotive, and tooling industries [6]. Particularly with PBF technology, in metal additive manufacturing, its properties can be improved even more by properly controlling the heat treatment temperatures and process parameters [2][3]. Investigating the energy-absorbing capacity of 17-4 PH stainless steel under dynamic loading conditions calls especially for Charpy impact testing, a vital technique for evaluating material toughness. Knowing the impact behavior under diverse LPBF parameters and heat treatment for 17-4 PH, is crucial for its utilization in safety-critical components, where resilience to unexpected shocks is essential. This work seeks to elucidate the impact properties of PBF-manufactured 17-4-PH stainless steel, consequently enhancing the optimization of additive manufacturing parameters for high-performance applications.

Further extensive research is required to achieve a complete understanding of the toughness behavior of the 17-4 PH and the fracture and failure mechanisms of LPBF components subjected to Charpy impact energy assessments. This understanding is crucial for precisely estimating, predicting, and optimizing the energy absorption capacity of various components. Given the important importance of toughness in determining the dependability and performance of materials in dynamic and safety-sensitive applications, it is imperative to examine the complex interplay between PBF process parameters, heat treatment conditions, and the resulting mechanical properties. Addressing these knowledge gaps would enhance our ability to predict material performance under impact loading and promote the broader implementation of PBF technology in industries requiring high reliability and performance.

Sarkar et al. [9] investigated the effect of heat treatments on the impact toughness of LPBF 15-5 PH stainless steel. Three heat treatment conditions, namely solution annealing, aging (H900), and over aging (H1150), were examined. Impact toughness was minimum in the aged condition (H900) at about 15 J due to the fine copper precipitates that increased hardness but decreased ductility. Conversely, the overaging condition (H1150) led to a substantial enhancement in impact toughness, reaching up to 40 J, attributed to the coarsening of copper precipitates and an increase in retained austenite, which enhanced ductility. The findings indicated that LPBF-manufactured components are expected to exhibit worse impact toughness relative to cold-rolled equivalents, suggesting the necessity for appropriate heat treatments to improve mechanical properties and minimize anisotropy. Also, Ty et al. [10] tested the suitability of Charpy impact testing as a means to detect process faults in Ni-based superalloy parts produced through LPBF. With reduced-sample sizes, the Charpy impact test was found within the research to detect local defects, e.g., absence of fusion which reduced resilience values by approximately 10% compared to defect-free material. The force-displacement curves showed large divergence in the propagation regime, consistent with the established defect sensitivity of Charpy testing. The results suggest that impact testing represents a viable quality control pathway for identifying production defects in LPBF-produced components. Sagar et al. [11] examined the temperature-dependent Charpy impact characteristics of 3D-printed 15-5 PH stainless steel at low (77 K), ambient (298 K), and elevated temperatures (723 K). The impact energy measurements were 0.01 J/cm² at low temperature, 6.78 ± 4.07 J/cm² at room temperature, and 50.84 ± 3.39 J/cm² at high temperature. The research demonstrated brittle behavior at low and ambient temperatures, marked by transgranular fracture, while elevated temperatures resulted in a more ductile response via micro void coalescence. The findings demonstrate a distinct shift from brittle to ductile failure with increased temperature, underlining the effect of temperature on the impact toughness of 3D-printed 15-5 PH stainless steel. Kovacs et al. [12] researched the effect of printing direction on mechanical properties of LPBF 17-4 PH stainless steel for aerospace application. Research showed that tensile strength, yield strength, and impact toughness were significantly impacted by build orientation. Samples produced in a horizontal direction exhibited the best mechanical properties with a Charpy impact energy of 75 J in the H1150 heat-treated condition. These findings suggest that the enhancement of build orientation can enhance the mechanical properties of LPBF-produced 17-4 PH stainless steel and render it a suitable candidate for high-stakes aerospace components, such as fuselage and wing parts. Kedziora et al. [1] analyzed the tensile, fatigue, and impact characteristics of 316L and 17-4 PH stainless steels fabricated using two distinct additive manufacturing techniques: Selective Laser Melting (SLM) and Metal Fused Filament Fabrication (FFF). The research indicated that SLM specimens demonstrated markedly superior mechanical qualities relative to FFF specimens. Charpy impact strength for SLM-made 17-4 PH was 75 J while that for the FFF samples was 45 J, which proves the superiority of the SLM process for structural applications. During the study, it was determined that although FFF can be utilized for lightweight non-critical components, SLM is the better process for producing high-performance stainless-steel components.

In this context, this study makes a novel contribution by investigating the effects of heat treatments and PBF printing parameters (laser power, scanning speed and hatch distance) on the toughness of LPBF 17-4 PH stainless steel, a topic that has not been extensively studied in the existing literature.

3.2.3 Material and method

3.2.3.1 The selected material and machine

Alloy 17-4 PH (AISI 630, ASTM A564, DIN 1.4542) belongs to the family of precipitation-hardened martensitic stainless steels, characterized by the presence of chromium, nickel and copper (Table 3.1). Its strength is due to the formation of copper particles within the martensitic matrix. The alloy boasts excellent mechanical properties, including high tensile strength, high impact resistance and toughness [6].

Table 3.1: Chemical composition (in %) of 17-4 PH stainless steel powder used for LPBF.

Element	**Fe**	**C**	**Mn**	**P**	**S**	**Si**	**Cr**	**Ni**	**Cu**	**Nb, Ta**
Volume (wt. %)	Bal.	0.07 max	1.0 max	0.04 max	0.03 max	1.0 max	15.0-17.5	3.0-5.0	3.0-5.0	0.15-0.45

The samples were created using the laser powder bed fusion (LPBF) technology with an EOSM290 equipment from EOS GmbH Germany shown in Figure 3.1. This modern machine is equipped with a maximum power 400 W fiber laser and with a 250 × 250 × 325 mm^3 of manufacturing area, which ensures precision and quality in the fabrication process.

In this study, experiments to optimize process parameters were planned using the Design of Experiments (DOE) method. Laser power (W) [198-220-242], scan speed (mm/s) [679.95-755.5-831.05], hatch distance (μm) [90-100-110], and tempering temperature (°C) [480-565-620] for heat treatment, were identified as four critical process parameters in 3D printing using powder bed melting and the layer thickness is fixed to 40 μm. These intervals were defined by applying a ±10% variation around the optimal parameter values recommended by the EOS manufacturer, to systematically evaluate the sensitivity of material properties to slight deviations in process conditions.

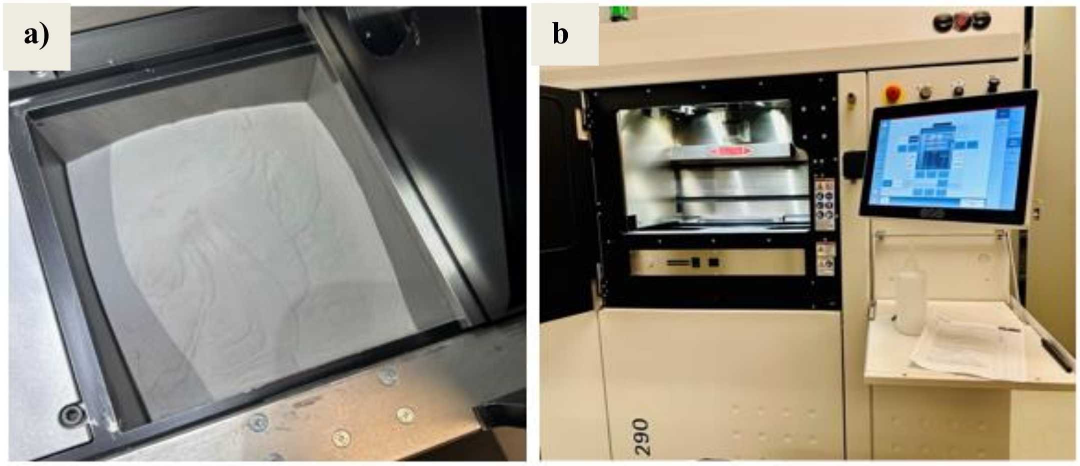

Figure 3.1: (a) Powder bed of the LPBF, showing the distribution of the powder; (b) Overview of the LPBF machine with control interface during the fabrication process.

Charpy impact tests were carried out on a total of 27 specimens. Three samples for each combination of the DOE for the repeatability of the impact energy test, were created using a horizontal construction orientation (0°) relative to the build plate, meaning that the axis of the samples was parallel to the construction plate. The supports used for printing the specimens were solid and 4 mm in thickness.

Impact resistance, or the ability to withstand impact, is a valuable characteristic and an efficient measurement for manufacturers of materials, critical to product design as well as quality control [6].

3.2.3.2 Charpy impact test method

The test configuration used in the Charpy impact test (Figure 3.2) comprises three major components: a notched test specimen, anvils that hold the specimen firmly in place and a pendulum. The pendulum, whose weight is predetermined, is mounted on a shaft that turns over a pivot fixed to the machine body. As it is in free fall, the pendulum follows a circular trajectory, striking the specimen at its precise center. This motion causes the conversion of kinetic energy to the test specimen. The amount of energy that the material absorbs during this test can be determined by comparing the original height of the pendulum and its final height after it strikes against the specimen, providing useful information about the impact resistance characteristics of the material. The test was set up in accordance with ASTM A370 [13] and ASTM E23 [14].

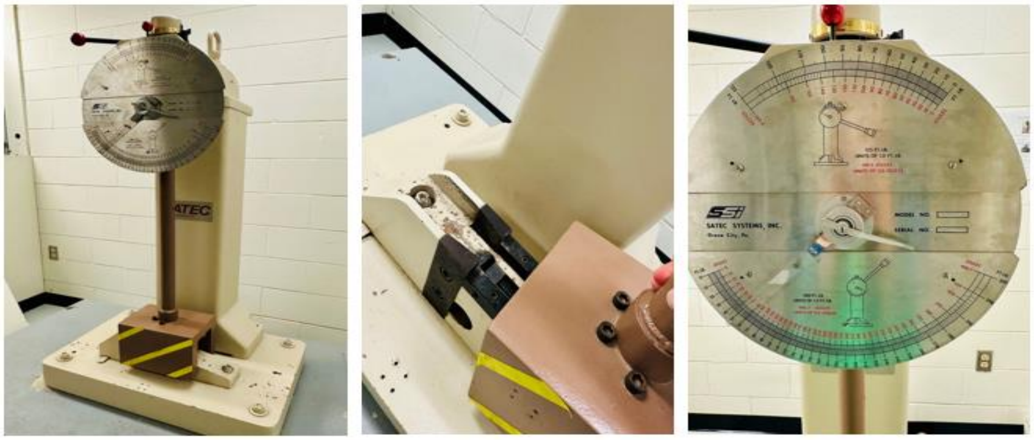

Figure 3.2: Charpy impact testing machine.

The dimensional and geometric feature of the specimens produced for the mechanical test is depicted in Figure 3.3. It shows a representative selection of the different kinds of specimens manufactured.

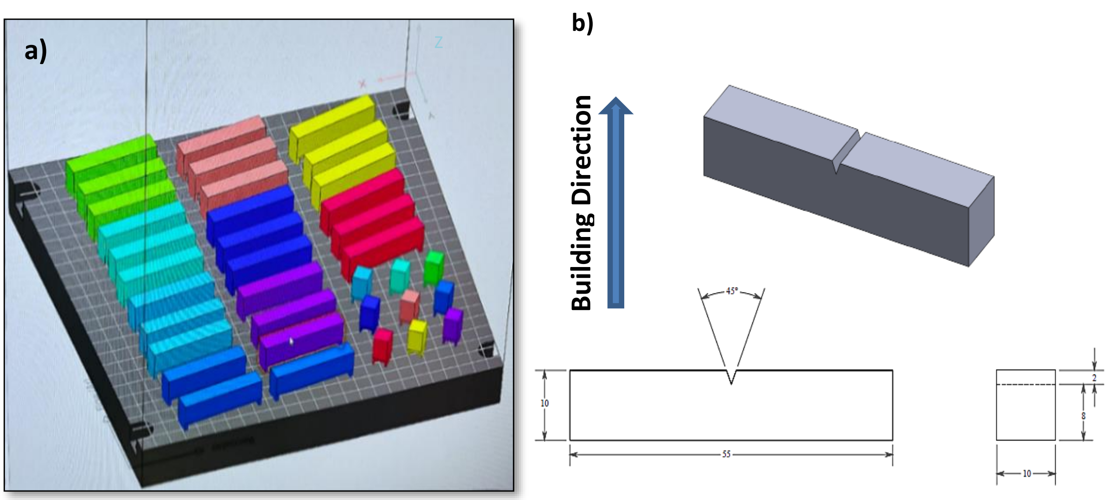

Figure 3.3: Design and layout of the charpy test specimens: (a) CAD layout of the specimens in the build chamber for the LPBF process; (b) Geometric details of the impact test specimen with notch dimensions.

3.2.4 Results and discussion

3.2.4.1 Toughness results and discussion

The impact test was designed to obtain information about how well a material can tolerate unexpected failure under situations of rapid stress escalation or internal flaws. This test entailed assessing the toughness of the material by measuring the amount of energy absorbed by the specimen when struck in the middle by a hammer attached to the end of a pendulum. The amount of energy absorbed during this process has a considerable impact on the degree of deformation and final breaking point of the specimen, providing an indication of the material's resilience under impact [15], [16].

Table 3.2: Manufacturing process parameters with impact test results.

	Laser power (w)	Scanning speed (mm/s)	Hatch distance (µm)	VED (J/mm³)	Aging temperature (°C)	Absorbed Energy (J)
S1	198	679.95	90	80.88	480	20
S2	198	755.5	100	65.52	565	72.66
S3	198	831.05	110	54.15	620	95.33
S4	220	679.95	100	80.88	620	120
S5	220	755.5	110	66.18	480	16.66
S6	220	831.05	90	73.53	565	72.66
S7	242	679.95	110	80.88	565	72.66
S8	242	755.5	90	88.98	620	121
S9	242	831.05	100	72.79	480	18

The impact test was carried out to provide knowledge about the resistance of a material to abrupt failure when there is a rapid increase in stress or defect within the material. The toughness of the material was determined by measuring the energy absorbed by the specimen when it is struck with a single blow in the middle by a hammer located at the end of a pendulum. Impact toughness features depend on both strength and ductility, which are usually inversely proportional, as well as grain size and dislocation density. Thus, this property could be influenced by microstructure and defects, which are very important process-related factors in materials produced by 3D printing. The values of the absorbed energy resulting from the dynamic impact tests are presented in Table 3.2 and Figure 3.4-(a).

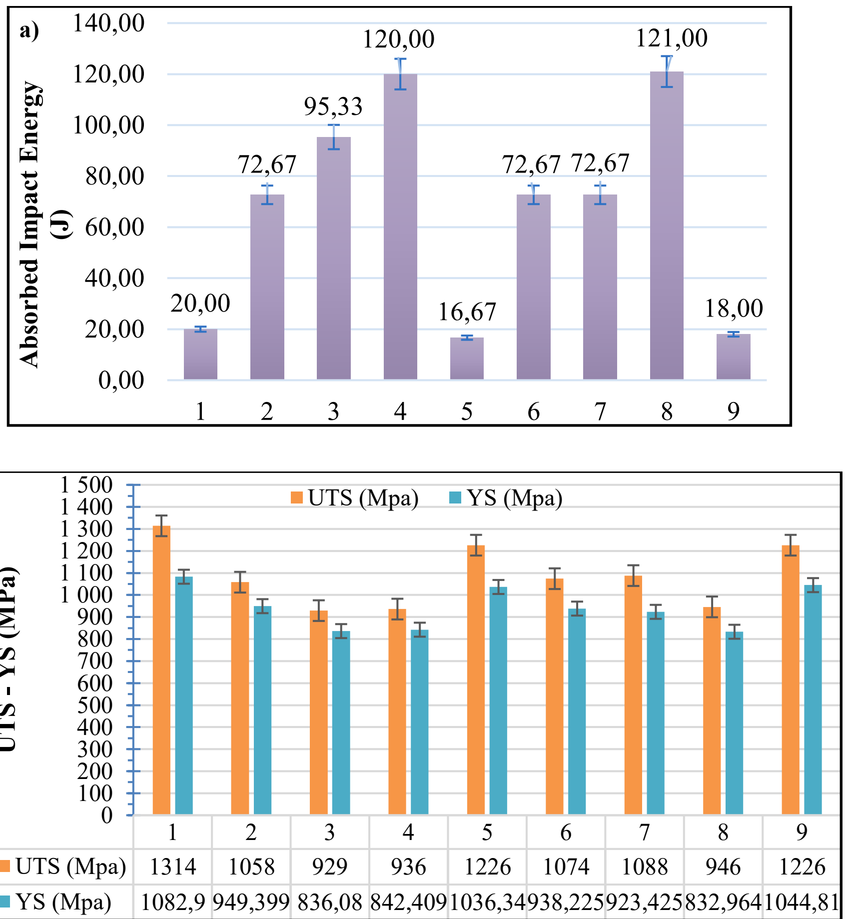

Figure 3.4: Mechanical properties of 17-4 PH stainless steel specimens after LPBF and heat treatment: a) Absorbed impact energy measured for each experimental condition; (b) Ultimate Tensile Strength (UTS) and Yield Strength (YS) for different conditions.

The results confirmed the outcomes obtained from tensile tests (Figure 3.4-(b)). As a consequence of the heat treatment, toughness and ductility are increased by increasing the aging temperature and this is for the set number 3, 4 and 8; and the set 8 had the superior value of absorbed energy. While having the higher ultimate tensile strength and yield strength values, the set 1, 5 and 9 had the less resilience values.

The impact toughness, as average absorbed energy, is found to increase with higher aging temperatures. Toughness is minimum at 480°C with values of absorbed energy of 20 J. The higher hardness at this temperature results in lower plastic deformation capability and increased susceptibility to brittle fracture. When the temperature is raised to 565°C and 620°C, the absorbed energy increases substantially, to 72.6 J at 565°C, and up to a maximum of 120 J at 620°C. Toughness improves with the formation of coarse precipitates, which reduce internal stresses and increase the material's ability for plastic deformation on impact loading.

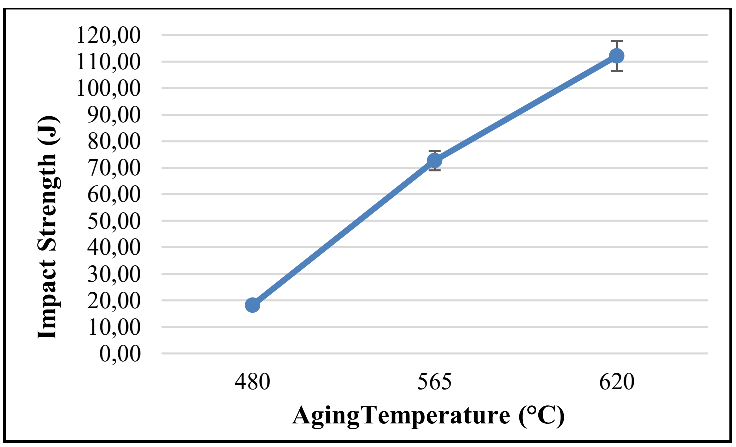

Figure 3.5: Variation of impact strength with aging temperature for 17-4 PH stainless steel specimens.

A clear inverse correlation of hardness to toughness can be observed under all heat treatment conditions, as indicated in Figure 3.5 and Figure 3.6. The highest hardness is achieved with the H900 condition (480°C) through the precipitation of small copper-rich precipitates, which limits dislocation mobility [17]. This significantly decreases toughness with brittle fracture behavior, as indicated by the reduced absorbed impact energy. A gain in impact resistance was observed by raising the aging temperature to 565°C (H1025 condition), with a slight reduction in hardness. The H1150 condition (620°C) strongly decreases hardness while improving toughness, promoting ductile fracture behavior. These results are explained from the coarsening of precipitates, which reduces internal stress concentrations and promotes more plastic deformation, hence enabling the material to absorb more energy during impact [18].

The microstructure is the cause of this interaction. The fine precipitates that form with lower temperature aging create a hard but brittle microstructure, while higher temperature aging creates the coarser precipitates that can sustain a greater amount of dislocation glide and energy absorption, thus creating greater toughness [19]. Precipitate coarsening reduces the barrier to dislocation glide and decreases hardness but increases the capacity of the material for plastic deformation. This is significant in adapting 17-4 PH stainless steel to a specific need. Increased hardness has advantages in application where wear resistance is a need, such as in tooling or in bearing parts. In applications where impact resistance and energy absorption are critical, such as structural components exposed to dynamic stress, reduced hardness and increased toughness are preferable. The H1025 condition provides an optimal blend of both features, making it a versatile option for components necessitating moderate levels of both hardness and toughness.

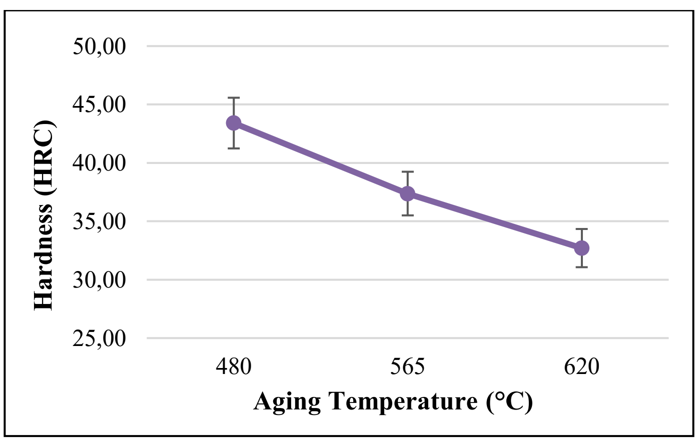

Figure 3.6: Hardness variation with aging temperature for 17-4 PH stainless steel specimens.

3.2.4.2 Microstructure and porosity analysis

The porosity introduced during the LPBF process has a direct impact on both hardness and toughness. Specimens with higher levels of porosity, as observed in sample S5 (H900) (Figure 3.7), exhibit lower toughness due to the presence of defects like lack of fusion and gas porosities. These defects act as stress concentrators, which initiate cracks and reduce the energy absorption capacity, contributing to brittle fracture. Conversely, the reduction in porosity, seen in specimens like S2 (H1025) (Figure 3.8), correlates with an improvement in toughness, albeit with some reduction in hardness. The lower porosity allows for better load distribution, enhancing the material's ability to absorb energy during fracture.

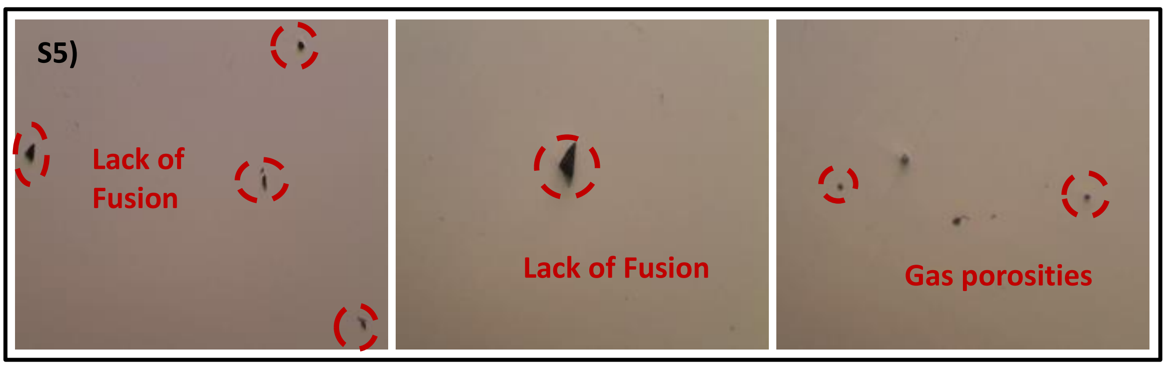

Figure 3.7: Optical micrographs showing defects in 17-4 PH stainless steel specimen S5 fabricated by LPBF and treated with H900 condition.

Figure 3.8: Optical micrographs showing defects in 17-4 PH stainless steel specimen S2 fabricated by LPBF and treated with H1025 condition.

3.2.4.3 Fractography analysis

The fractographic analysis of Charpy impact-tested specimens allows an in-depth comprehension of the fracture behavior of 17-4 PH stainless steel produced with LPBF and then subjected to various heat treatments (H900, H1025, H1150). The specimens are classified according to their heat treatment conditions, and visual observations, supported by SEM imaging, show particular fracture morphologies, enabling interactions between microstructural evolution and mechanical behavior. We present a comprehensive analysis that links these findings to the LPBF parameters and heat treatment conditions to clarify the fracture mechanisms in these materials.

Specimens treated under the H900 condition were aged at a moderately low temperature that had the tendency to initiate fine copper precipitation and thus increase the 17-4 PH hardness. As a side effect, major softening resulted that decreased the level of ductility and toughness shown by a comparatively low mean value of the absorbed energy (E = 20 J). The morphologies of the fracture in S1, S5, and S9 specimens exhibit predominantly brittle features, highlighting the low ductility and poor energy absorption capacity of this state.
The shear zones possess relatively smooth and unremarkable zones, exhibiting a largely brittle fracture mechanism with little energy absorption. The fine copper precipitates generated during the H900 treatment enhance microhardness; however, these results in lower ductility, rendering the material subject to brittle fracture [20], as shown in Figure 3.9.
The fracture zones of these specimens display a refined morphology with distinct cleavage facets, reflecting brittle fracture characteristics. The lack of significant plastic deformation characteristics, such as micro-void coalescence, supports the conclusion that these specimens failed in a brittle way. The increased hardness achieved with the H900 treatment leads to enhanced brittleness, reducing the capacity for plastic deformation before to fracture [21].

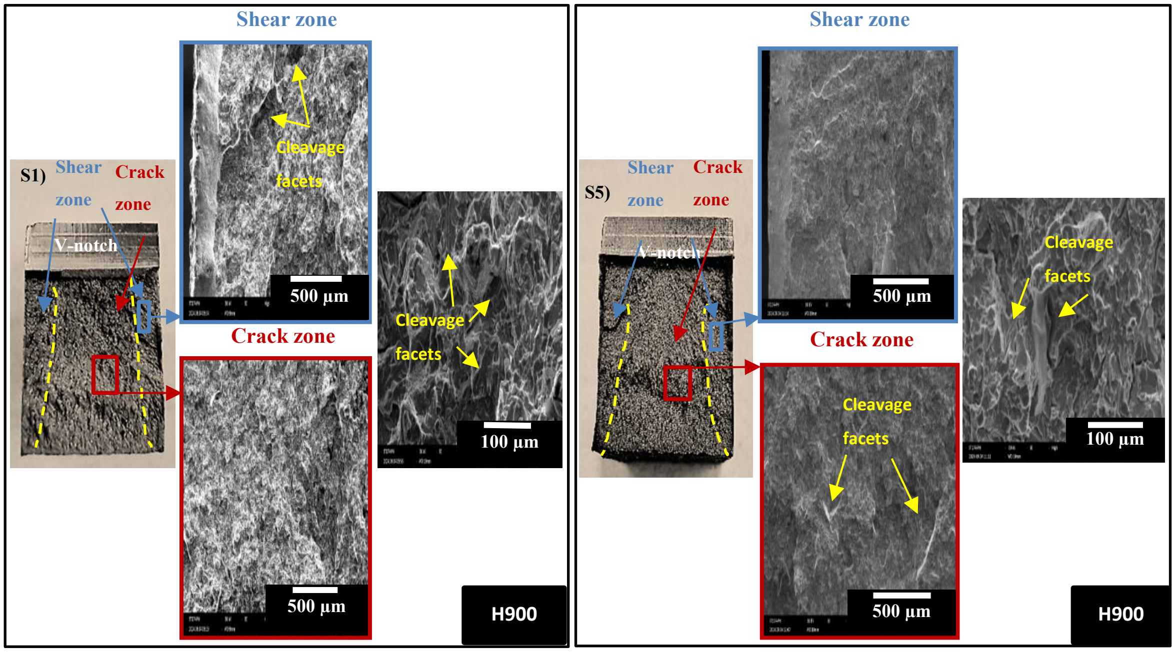

Figure 3.9: SEM fractography of Charpy impact fracture surfaces of 17-4 PH stainless steel specimens aged at H900. (a) Specimen S1, (b) specimen S5.

The specimens exposed to the H1025 condition, characterized by aging at an intermediate temperature, exhibit distinct fracture characteristics that illustrate the balance between ductility and strength obtained through this heat treatment. This condition promotes precipitate formation and growth, resulting in lower internal stresses and improved toughness.

The SEM analysis of the shear zones for S2, S6, and S7 samples reveals a more consistent dimple distribution with a larger average dimple size. This indicates greater ductility, since the larger precipitates that form at higher aging temperatures assist in reducing residual stresses and enabling easy movement of dislocations. The fractographs reinforce this observation by presenting sharp dimple structures, validating the material's ability for extensive plastic deformation. Passive characteristics detection emphasizes the material's capacity to effectively absorb energy from impact.

The crack zones (Figure 3.10) point to a less brittle character compared to the samples treated at H900. The fracture surfaces show greater irregularity, displaying micro-fractures and secondary cracks that suggest crack deflection, enabling energy dissipation during fracture.

The fractographs presented in Figure 3.10 exhibit less prominent cleavage facets and increased signs of ductile tearing, reflecting enhanced energy absorption capacity. The H1025 treatment achieves an optimal balance between hardness and toughness, enhancing impact resistance and reducing the possibility of brittle fracture.

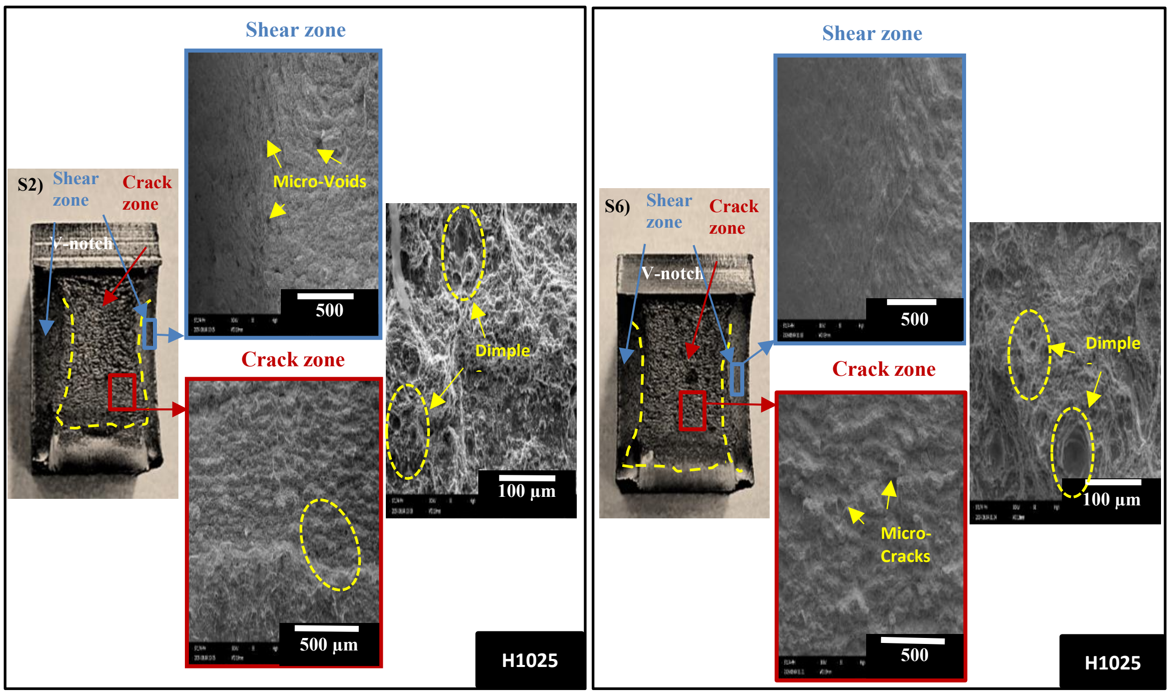

Figure 3.10: SEM fractography of Charpy impact fracture surfaces of 17-4 PH stainless steel specimens aged at H1025. (a) Specimen S2, (b) specimen S6.

The H1150 heat treatment condition, defined by high temperature aging, leads to the development of coarse precipitates, a reduction in hardness, and an increase in toughness. The fracture surfaces of specimens S3, S4, and S8 demonstrate the influence of microstructural changes on the material's fracture behavior.

The shear zones of the H1150-treated samples (Figure 3.11) show a significant plastic deformation with deep and well-defined dimples on the fracture surface. The presence of these dimples indicates a highly ductile fracture mechanism since the coarse precipitates that develop during the H1150 aging process actually reduce internal stresses and enhance energy absorption during impact. The decrease in hardness, along with enhanced ductility and higher toughness, leads to a more evident ductile fracture mode. The fractographs highlight the significant ductility, since the wider and deeper dimples indicate considerable plastic deformation before fracture, affirming the material's capacity to absorb substantial impact energy.

The crack areas in the above-mentioned specimens are characterized by very high levels of irregular fracture surfaces, high levels of micro-void coalescence indicators, and crack branching. The fractographs reveal highly meandering crack paths with very high levels of crack deflection, showing high resistance to crack propagation and energy absorption. The H1150 treatment yields the highest toughness of the three conditions, as demonstrated by the extensive shear zones and absence of features of brittle fracture in the crack zones (Figure 3.11). The average absorption energy (E = 120 J) also supports the enhanced toughness obtained under the H1150 condition, which is preferable in service with high impact strength and lower hardness.

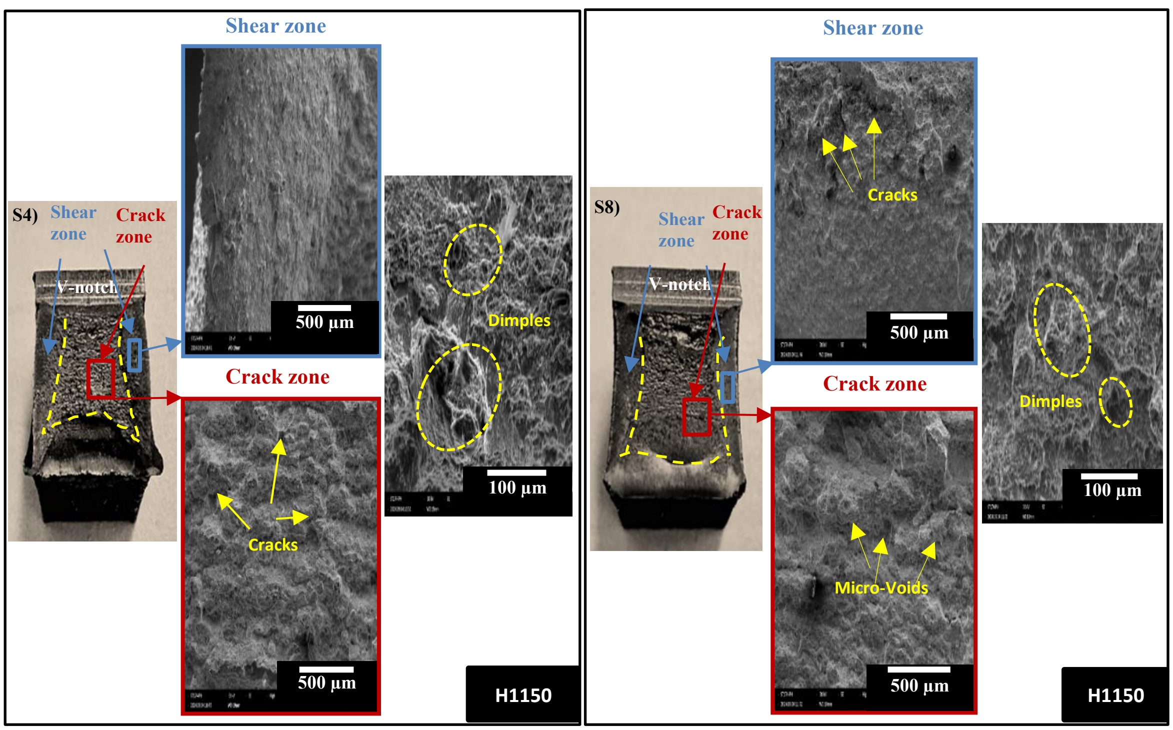

Figure 3.11: SEM fractography of Charpy impact fracture surfaces of 17-4 PH stainless steel specimens aged H1150. (a) Specimen S4, (b) specimen S8.

The fracture behavior of the samples can be directly correlated with LPBF parameters and heat treatments. The laser power, scanning speed, and hatch distance parameters play a crucial role in determining the as-start microstructure of the material and thereby its response to heat treatment.

The rapid cooling rates inherent in the LPBF process produce a fine martensitic microstructure highly susceptible to additional aging treatment [22]. The H900 treatment with the lower aging temperature forms fine precipitates that harden through strengthening but also cause brittle fracture behavior, as revealed in the crack zones of samples S1, S5, and S9. On the other hand, H1025 and H1150 treatments promote the development of more coarse precipitates, reducing internal stresses and improving ductility, as indicated by the larger range of ductile shear zones in these specimens.

The ability to balance toughness and hardness is the key to 17-4 PH stainless steel high-performance applications. The H900-treated specimens possess higher hardness, which at the cost of higher brittleness, is suitable for wear resistance. The H1025 treatment is a balance of strength and toughness and therefore suitable for applications where moderate impact resistance is required. The H1150 treatment, being a toughness-oriented treatment, is suitable for applications where catastrophic failure resistance and energy absorption are crucial.

3.2.5 Conclusion

This study highlights the significant influence of LPBF process parameters and heat treatment conditions in controlling the toughness of additively manufactured 17-4 PH stainless steel. It is clear from the findings that aging temperature raised to 620°C (H1150 condition) enhances the toughness through coarse precipitate formation and thus improving the ductility and energy absorption capacity up to an optimum Charpy absorbed energy of 120 J. In addition, this research emphasizes the significance of LPBF process parameters—laser power, scanning speed, and hatch distance—in controlling defect formation, microstructure integrity, and thus mechanical properties.

By bridging the gap in the existing literature regarding LPBF-produced 17-4 PH stainless steel, the study provides concrete recommendations for material property tailoring to suit the particular requirements of high-impact resistance applications, such as aerospace and automotive components.

3.2.6 References

[1] S. Kedziora *et al.*, 'Strength Properties of 316L and 17-4 PH Stainless Steel Produced with Additive Manufacturing', *Materials*, vol. 15, no. 18, p. 6278, Sep. 2022, doi: 10.3390/ma15186278.

[2] R. Singh *et al.*, 'Powder bed fusion process in additive manufacturing: An overview', *Materials Today: Proceedings*, vol. 26, pp. 3058–3070, 2020, doi: 10.1016/j.matpr.2020.02.635.

[3] P. K. Gokuldoss, S. Kolla, and J. Eckert, 'Additive Manufacturing Processes: Selective Laser Melting, Electron Beam Melting and Binder Jetting—Selection Guidelines', *Materials*, vol. 10, no. 6, p. 672, Jun. 2017, doi: 10.3390/ma10060672.

[4] D. Basu, Z. Wu, J. L. L. Meyer, E. Larson, R. Kuo, and A. Rollett, 'Entrapped Gas and Process Parameter-Induced Porosity Formation in Additively Manufactured 17-4 PH Stainless Steel', *J. of Materi Eng and Perform*, vol. 30, no. 7, pp. 5195–5202, Jul. 2021, doi: 10.1007/s11665-021-05695-3.

[5] S. E. Kovacs *et al.*, 'Additive Manufacturing of 17-4PH Alloy: Tailoring the Printing Orientation for Enhanced Aerospace Application Performance', *Aerospace*, vol. 10, no. 7, p. 619, Jul. 2023, doi: 10.3390/aerospace10070619.

[6] F. R. Andreacola, I. Capasso, A. Langella, and G. Brando, '3D-printed metals: Process parameters effects on mechanical properties of 17-4 P H stainless steel', *Heliyon*, vol. 9, no. 7, p. e17698, Jul. 2023, doi: 10.1016/j.heliyon.2023.e17698.

[7] T. Muslim, T. Karagoz, S. Kurama, P. Sezer, O. F. Yazici, and R. Ozkok, 'Laser metal deposition of 17–4 PH stainless steel: Geometrical, microstructural, and mechanical properties investigation for structural applications', *CIRP Journal of Manufacturing Science and Technology*, vol. 41, pp. 69–79, Apr. 2023, doi: 10.1016/j.cirpj.2022.12.010.

[8] L. J. Vendra, A. Achanta, and E. Sullivan, 'Fatigue Behavior of Laser Metal Deposited 17-4 PH Stainless Steel', in *Structural Integrity of Additive Manufactured Parts*, N. Shamsaei, S. Daniewicz, N. Hrabe, S. Beretta, J. Waller, and M. Seifi, Eds., 100 Barr Harbor Drive, PO Box C700, West Conshohocken, PA 19428-2959: ASTM International, 2020, pp. 399–414. doi: 10.1520/STP162020180138.

[9] S. Sarkar, S. Dubey, and A. K. Nath, 'Effect of Heat Treatment on Impact Toughness of Selective Laser Melted Stainless Steel Parts', in *Volume 1: Additive Manufacturing; Bio and Sustainable Manufacturing*, College Station, Texas, USA: American Society of Mechanical Engineers, Jun. 2018, p. V001T01A005. doi: 10.1115/MSEC2018-6418.

[10] A. Ty, M. Mokhtari, Y. Balcaen, A. Votié, J.-M. Cloué, and J. Alexis, 'Performance evaluation of Charpy impact tests to investigate and detect process defects of a Ni-based superalloy elaborated by laser powder bed fusion', *Journal of Materials Research and Technology*, vol. 25, pp. 6644–6659, Jul. 2023, doi: 10.1016/j.jmrt.2023.07.064.

[11] S. Sagar, Y. Zhang, H.-H. Choi, Y.-G. Jung, and J. Zhang, 'Temperature-dependent Charpy impact property of 3D printed 15-5 PH stainless steel', *Materials Science and Technology*, vol. 37, no. 2, pp. 190–201, Jan. 2021, doi: 10.1080/02670836.2021.1885094.

[12] S. E. Kovacs *et al.*, 'Additive Manufacturing of 17-4PH Alloy: Tailoring the Printing Orientation for Enhanced Aerospace Application Performance', *Aerospace*, vol. 10, no. 7, p. 619, Jul. 2023, doi: 10.3390/aerospace10070619.

[13] A01 Committee, 'Test Methods and Definitions for Mechanical Testing of Steel Products', ASTM International. doi: 10.1520/A0370-20.

[14] E28 Committee, 'Test Methods for Notched Bar Impact Testing of Metallic Materials', ASTM International. doi: 10.1520/E0023-16B.

[15] J. J. Wang *et al.*, 'IMPACT AND FATIGUE CHARACTERISTICS OF ADDITIVELY MANUFACTURED STEEL MATERIALS: A REVIEW'.

[16] E. Yasa, J. Deckers, J.-P. Kruth, M. Rombouts, and J. Luyten, 'Charpy impact testing of metallic selective laser melting parts', *Virtual and Physical Prototyping*, vol. 5, no. 2, pp. 89–98, Jun. 2010, doi: 10.1080/17452751003703894.

[17] L. Zai *et al.*, 'Laser Powder Bed Fusion of Precipitation-Hardened Martensitic Stainless Steels: A Review', *Metals*, vol. 10, no. 2, p. 255, Feb. 2020, doi: 10.3390/met10020255.

[18] B. Bai, R. Hu, C. Zhang, J. Xue, and W. Yang, 'Effect of precipitates on hardening of 17-4PH martensitic stainless steel serviced at 300 °C in nuclear power plant', *Annals of Nuclear Energy*, vol. 154, p. 108123, May 2021, doi: 10.1016/j.anucene.2020.108123.

[19] S. Spigarelli, M. Cabibbo, A. Santoni, and E. Santecchia, 'Short-term creep approach to redefining the role of 17-4PH stainless steel for high-temperature applications', *Sci Rep*, vol. 14, no. 1, p. 8306, Apr. 2024, doi: 10.1038/s41598-024-58273-7.

[20] Y.-H. Cho, S.-Y. Park, J.-Y. Kim, and K.-A. Lee, '17-4PH stainless steel with excellent strength–elongation combination developed via material extrusion additive manufacturing', *Journal of Materials Research and Technology*, vol. 24, pp. 3284–3299, May 2023, doi: 10.1016/j.jmrt.2023.03.228.

[21] P. Suri, B. P. Smarslok, and R. M. German, 'Impact properties of sintered and wrought 17–4 PH stainless steel', *Powder Metallurgy*, vol. 49, no. 1, pp. 40–47, Mar. 2006, doi: 10.1179/174329006X89317.

[22] M. S. Moyle *et al.*, 'Correlation of microstructure, mechanical properties, and residual stress of 17-4 PH stainless steel fabricated by laser powder bed fusion', *Journal of Materials Science & Technology*, vol. 198, pp. 83–97, Nov. 2024, doi: 10.1016/j.jmst.2024.01.080.

CHAPITRE 4
ANALYSE DU COMPORTEMENT EN FATIGUE ET DE LA FRACTOGRAPHIE DE L'ACIER INOXYDABLE 17-4 PH FABRIQUÉ PAR LPBF : INFLUENCE DE L'ORIENTATION DE FABRICATION SOUS DES CONDITIONS OPTIMISÉES

4.1 RÉSUMÉ EN FRANÇAIS DU QUATRIÈME ARTICLE

Dans ce chapitre, l'influence de l'orientation de fabrication sur le comportement en fatigue de l'acier inoxydable 17-4 PH fabriqué par fusion laser sur lit de poudre (LPBF) est étudiée sous des conditions de fabrication optimisées (densité obtenue ~98,9 % et faible porosité). Des éprouvettes de fatigue imprimées selon deux orientations distinctes (horizontale à 0° et inclinée à 45° par rapport à la plateforme) ont subi un traitement thermique standard H1025 (vieillissement à 565 °C pendant 1 heure). Ces paramètres de fabrication utilisés correspondent aux conditions optimisées identifiées lors des études précédentes. Afin d'isoler l'effet de l'orientation, seule la direction a été considérée dans cette analyse. Les résultats des essais de fatigue montrent que, malgré une limite d'endurance similaire pour les deux orientations (~355 MPa à 0° et ~350 MPa à 45°), les éprouvettes à 45° présentent une durée de vie nettement plus élevée, particulièrement dans les régimes de fatigue faible à moyen nombre de cycles (LCF à moyen cycle). À contrainte équivalente, la durée de vie des échantillons inclinés était approximativement doublée par rapport aux horizontaux. L'analyse fractographique réalisée en microscopie électronique à balayage (MEB) confirme ces observations en révélant des mécanismes de propagation des fissures différents selon l'orientation : une propagation plane parallèle aux couches de fabrication pour les éprouvettes horizontales, et un trajet de fissure plus sinueux, avec davantage de stries et une rupture finale plus ductile pour les éprouvettes inclinées. Cette recherche comble ainsi un manque critique de connaissances sur l'impact des orientations intermédiaires (notamment à 45°) sur les performances en fatigue, offrant aux concepteurs des recommandations pratiques pour l'optimisation des propriétés mécaniques et la durabilité en fatigue des composants produits par fabrication additive dans les secteurs industriel et aéronautique.

Mots clés : LPBF, Direction d’impression, Comportement en fatigue, 17-4 PH, Paramètres optimum.

4.2 FATIGUE BEHAVIOR AND FRACTOGRAPHIC ANALYSIS OF LPBF 17-4 PH STAINLESS STEEL: INFLUENCE OF BUILD ORIENTATION UNDER OPTIMIZED PROCESSING CONDITIONS

Yassmine Chedly[1], Noureddine Barka[1]

[1] Department of Mathematics, Computer Science and Engineering, University of Québec at Rimouski (UQAR), Rimouski, Québec, Canada, G5L 3A1

4.2.1 Abstract

This research investigates the effect of build orientation on fatigue properties of 17-4 PH stainless steel manufactured via Laser Powder Bed Fusion (LPBF). Fatigue samples were created with optimized processing conditions from the previous study and underwent a H1025 heat treatment, resulting in high densification (~98.9%) and reduced porosity. The only variable considered was the build orientation—horizontal (0°) and angle (45°)—to test its effect on fatigue behavior.

Fatigue tests at stress-controlled conditions were performed. Test results indicated that although endurance limits for both orientations were comparable (~ 350 MPa and 355 MPa), inclined specimens of all orientations tend to have longer life in both low-cycle and mid-cycle regimes of fatigue compared to horizontal ones. At the same stress amplitudes, the 45° specimens had twice the life.

These findings were corroborated by fractographic analysis: horizontal fractures showed planar crack growth simultaneously with layer deposition, while inclined fractures showed wavier crack path, more closely spaced striations, and increased ductility of terminal rupture areas.

This work addresses a critical research gap by systematically comparing fatigue behavior at an intermediate build orientation (45°), demonstrating distinct crack propagation mechanisms and enhanced fatigue performance compared to the conventional horizontal orientation under optimized LPBF processing conditions.

Key words: Additive manufacturing, LPBF, 17-4 PH, build orientation, fatigue behavior.

4.2.2 Introduction

Additive manufacturing (AM) has progressed from being used as a prototyping method to being used as an industrial production method, presenting new engineering and materials research opportunities. In contrast to the traditional subtractive approach of material removal to construct a component, additive manufacturing (AM) allows for the construction of a part through sequential layer-by-layer addition, with unparalleled design flexibility, minimized material waste, and highly tailored mechanical characteristics [1].
Among the numerous additive manufacturing processes, Laser Powder Bed Fusion (LPBF) is an excellent method for the production of high-performance metallic components [2]. LPBF employs a high-power laser to melt metal powder of small size selectively and form dense, near-net-shape components with complex geometries. LPBF technology is specifically useful in such applications that are related to lightweight, strong, and geometrically complex components, including aerospace, biomedical implants, and high-performance vehicle components [3].

17-4 PH stainless steel, can be the most highly anticipated material produced by LPBF, is a martensitic precipitation-hardening alloy famous for its high strength, corrosion resistance, and heat treatment response. All of these properties make it a critical material in high-performance uses as varied as aircraft structural components to offshore drilling rigs and implants. However, in spite of the numerous advantages of LPBF, there are still lingering issues, particularly in relation to the fatigue resistance of printed components—a factor that dictates the long-term reliability of load-bearing structures.
Fatigue failure remains the most unpredictable and disastrous failure mode in engineering parts. Unlike static loading, where failure occurs after some definite stress threshold, fatigue is insidious—it builds up unnoticeably through thousands or even millions of loading cycles, often without warning, before total failure [4]. Fatigue resistance in industries such as aerospace, energy, and automotive manufacturing is not merely a performance problem—it is a matter of safety, long-term integrity, and economic sustainability.

For instance, in aerospace use, turbine blades and structural components are exposed to repeated cyclic loading by aerodynamic loads and thermal cycles. Catastrophic failure can occur due to even a very minor fatigue crack in a jet engine component [5]. Fatigue controls the life of engine mounts, transmission gears, and suspension systems in automotive powertrains, where materials must withstand long-duration cyclic loading in various environments.

In additively processed metals, the fatigue response is more complex than in conventionally processed parts. LPBF's layer-by-layer build results in microstructural anisotropy, residual stresses, and processing defects, all of which are sites for fatigue crack initiation [6]. Among the most influential factors on fatigue performance in LPBF parts are: Porosity and lack of fusion defects, providing stress concentration sites. Furthermore, surface roughness, promoting early crack nucleation.

One of the most fundamental among these is the effect of printing direction on fatigue resistance. The manner in which the layers are deposited during manufacture dictates grain growth, defect distribution, and residual stress patterns, which influence the response of the part to cyclic loading [7].

Over the last ten years, considerable work has been aimed at characterizing the mechanical properties of LPBF-processed metallic alloys, particularly with respect to residual stresses, porosity, and microstructural anisotropy. While some works have investigated post-processing treatments and the influence on strength and ductility, fewer articles have systematically evaluated the fatigue response of 17-4 PH stainless steel to cyclic loading. Moreover, the role of build orientation in influencing the fatigue performance is also an area that should be researched more. The following section provides an overview of the relevant studies that have investigated these critical areas.

Recently, Alhajeri et al. [8] conducted a comprehensive statistical analysis to investigate the influence of build orientation, surface finish, and loading conditions on the fatigue life of LPBF-fabricated 17-4 PH stainless steel. Their findings highlighted the profound influence of build orientation on fatigue life, where vertically printed specimens had lower endurance limit due to layer-induced defects that acted as crack initiation sites. In addition to this, they demonstrated that machined and polished conditions significantly increase fatigue strength, highlighting the importance of orientation and post-processing in fatigue-intensive applications.

Moyle et al. [9] provided a comprehensive description of LPBF-processed 17-4 PH stainless steel with details on the manner in which build orientation, laser power, and scanning strategy directly influence mechanical properties and residual stress distributions. They confirmed that tensile strength and ductility of horizontally printed specimens are higher than specimens built vertically due to the fact that primarily reduced porosity and enhanced layer cohesion are the dominant phenomena. Besides, their neutron diffraction measurements revealed how scanning patterns may induce high internal stresses, affecting part integrity and fatigue performance.

Zhang [10] provided a comprehensive review of corrosion and stress corrosion cracking mechanisms in both wrought and additively manufactured 17-4 PH stainless steel. The study emphasized the critical role played by microstructural inhomogeneities, surface roughness, and build orientation in initiating fatigue cracks and corrosion pits. The findings underscore the significance of controlling orientation and post-processing to enhance fatigue and corrosion resistance in AM parts for extreme industrial applications.

Sepe et al. [11] investigated the static and fatigue behaviour of laser-welded 17-4 PH steel plates produced by LPBF, demonstrating that high-quality laser welding preserves mechanical properties and provides an endurance limit of approximately 270 MPa. Their results highlighted that all fatigue failures occurred within the heat-affected zone, underscoring the critical role of microstructural discontinuities and localized stress concentrations in fatigue life, paralleling the layer-induced weaknesses observed in additively manufactured structures.

Kalita and Jayaganthan [12] investigated mechanical and microstructure response of wrought and LPBF-manufactured 17-4 PH stainless steel, stressing the dominant impact of build direction and inherent porosity on ultra-low cycle fatigue life. In their study, they found horizontally printed samples have higher tensile strength and endurance to fatigue due to reduced porosity and interlayer bonding and vertical builds still vulnerable to premature failure. These findings highlight the critical significance of orientation control in fatigue-critical additive manufacturing processes.

In summary, despite significant research having been devoted to understanding the mechanical and fatigue behavior of LPBF-fabricated 17-4 PH stainless steel, literature continually suggests that build orientation is one of the most influential factors governing fatigue life. Different studies have concluded that vertically oriented specimens demonstrate worse fatigue performance due to layer-boundary defects and stress raisers aligned in the direction of the load axis. However, even though horizontal orientations are commonly held to be ideal, the in-plane behavior of components produced at intermediate angles and particularly at 45° still remains poorly examined. This comes into play especially under optimized process and post-process conditions, when minor variations of microstructural anisotropy and defect topology can significantly influence crack initiation directions and propagation channels. The absence of systematic comparisons of 45-degree and horizontal orientations leaves a gap in component design recommendations for structures subjected to complex multi-axial loading. Hence, the current study is driven by the need to critically analyze and compare the 17-4 PH stainless steel samples' fatigue life, S-N behavior, and fracture characteristics produced at horizontal and 45° build orientations. By this focused endeavor, the research aims to yield distinct, experimentally validated results that can help designers and producers in the development of fatigue-resistant AM parts for high-performance industrial applications.

4.2.3 Material and methods

In this work, the material of interest is 17-4 PH stainless steel, a precipitation-hardening martensitic alloy with wide usage in aerospace, automotive, and energy sectors due to its excellent strength, exceptional corrosion resistance, and good weldability. Choosing such material is in accordance with the aim of studying fatigue behaviour in parts for application in load-bearing structures where mechanical integrity and environmental durability are simultaneously essential.

Samples were produced by LPBF process using optimized process parameters sequence established by previous optimization aimed at maximizing density, microstructural homogeneity, and mechanical performance, with reduced porosity, ensuring that fatigue life variations are primarily attributed to build orientation effects. The processing was conducted at the provided parameters in the Table 4.1. These conditions were selected specifically to promote best layer bonding, uniform microstructure, and reduced defect density, so that fatigue properties would be controlled by build direction and not by process-induced variation.

Table 4.1: Summary of the LPBF processing parameters and post-processing heat treatment conditions applied to all specimens.

Laser Power (W)	242 W
Scan Speed (mm/s)	679.95 mm/s
Hatch Distance (µm)	110 µm
Layer Thickness (µm)	40 µm
Solution treatment	1040 °C (30 min)
Aging temperature	565 °C (1h)

Two build orientations were selected for this study: 0° (horizontal) and 45° relative to the build platform. The 45° orientation was specifically selected to address an important gap in the literature, where most fatigue analyses have been limited to horizontal and vertical orientations at the expense of intermediate angles that are frequently encountered in complex part geometries. The design and orientation of the specimen were optimized with building preparation software to minimize support interference and thermal distortions (Figure 4.1). Fatigue specimens adopted standard geometries according to ASTM E466 as presented in Figure 4.2.

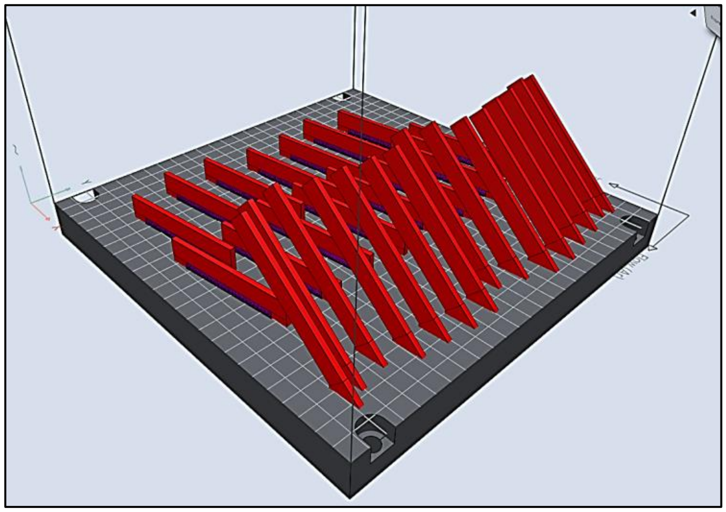

Figure 4.1: CAD layout of the LPBF build platform showing fatigue specimens printed at two different orientations: horizontal (0°) and inclined (45°).

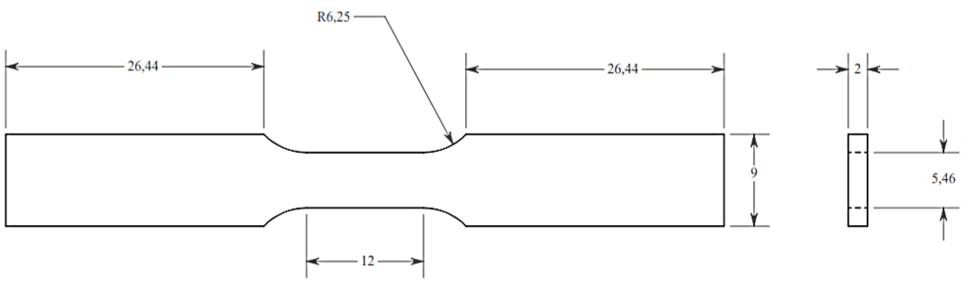

Figure 4.2: Specimen geometry for axial fatigue testing.

All the samples were printed in a single batch on a rectangular build plate to ensure process condition uniformity and minimize inter-batch variation.

Following fabrication, solution annealing at 1040 °C for 30 min was carried out on all specimens, followed by aging treatment for 1h at 565 °C. These optimal parameters are adopted from previous research to achieve ultimate mechanical performance. The treatment is performed here to homogenize the microstructures, precipitate strengthening phases, and remove residual stresses which otherwise cause results of fatigue tests to be skewed [13].

To properly assess the effect of build orientation on fatigue life, all the specimens were tested under cyclic fatigue with a stress ratio of R = 0.05, imitating tension-tension loading conditions common in-service application. The testing was performed using a servohydraulic testing machine at a frequency of 20 Hz, trading off test duration and reducing thermal effects or dynamic loading artifacts [14].

The applied load amplitudes were carefully defined to capture both the high-cycle fatigue regime (HCF) and the transition zone, allowing the construction of comprehensive S–N curves. Each test was carried out up to 10^6 cycles, or until specimen failure occurred. The endurance limit was defined as the maximum stress level at which specimens survived beyond 10^6 cycles without failure.

In addition, to ensure that observed fatigue failures were governed by internal microstructural and orientation-related phenomena rather than surface irregularities, all specimens underwent sandblasting following the aging heat treatment. This surface preparation step significantly reduced residual roughness and eliminated surface artifacts, which could otherwise serve as premature crack initiation sites [15]. Careful attention was also paid to specimen alignment and test setup to avoid bending-induced stresses.

4.2.4 Results and Discussion

4.2.4.1 Static Mechanical Performance

Tensile behavior of LPBF-printed 17-4 PH stainless steel processed under the process parameters optimized previously (VED = 80.88 J/mm³, laser power = 242 W, scan speed = 679.95 mm/s, hatch distance = 110 µm, and 40 µm layer thickness) and subsequently heat treated following H1025 protocol (solution annealing at 1040°C for 30 minutes and aging at 565°C for 1 hour) was examined under horizontal (0°) and inclined (45°) build orientations. These conditions, which were found to produce near-optimal part integrity with measured density of 98.92% and microhardness of 38.51 HRC, ensured that the observed mechanical behavior was significantly representative of intrinsic orientation effects and not processing defects.

The engineering stress-strain curves (Figure 4.3) exhibit classic behavior for precipitation-hardened stainless steel, featuring a distinct elastic zone, a yielding plateau, and pronounced strain hardening before necking occurs. Both orientations demonstrated stable plastic deformation without indications of early fracture or brittleness. The horizontal orientation exhibited slightly superior yield strength and elongation, while the inclined (45°) orientation exhibited slightly lower strength and ductility.

Quantitative findings (Figure 4.4) reveal that horizontal specimens exhibited yield strength (YS) of 1032 MPa, ultimate tensile strength (UTS) of 1122 MPa, and elongation of 23.2%, whereas inclined specimens exhibited YS of 1012 MPa, UTS of 1111 MPa, and elongation of 21.6%. These small differences reveal the subtle influence of build orientation on static mechanical properties even for the case of optimized conditions with low porosity and good layer cohesion.

This is because the load path alignment is favorable in the direction parallel to layer interfaces for better interlayer bonding and lesser sensitivity to stress concentrations [16]. However, the 45° orientation, is a more complex loading situation in which applied stress interacts with the sloping layer boundaries, potentially causing premature micro-slip or local decohesion at interlayer interfaces and creating a marginal reduction in strength and ductility [17].

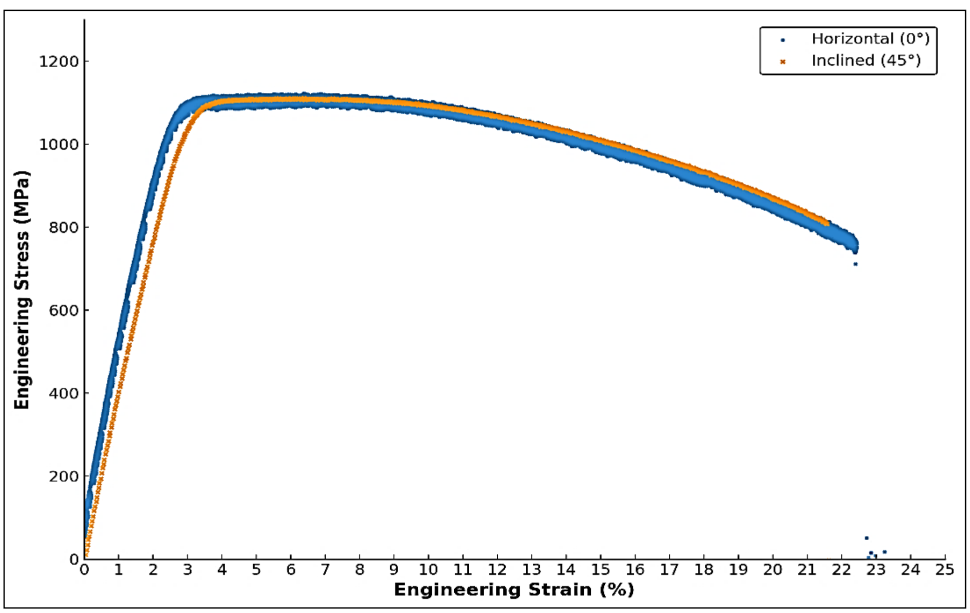

Figure 4.3: Engineering stress–strain curves obtained from tensile tests of LPBF 17-4 PH stainless steel specimens built at horizontal (0°) and inclined (45°) orientations.

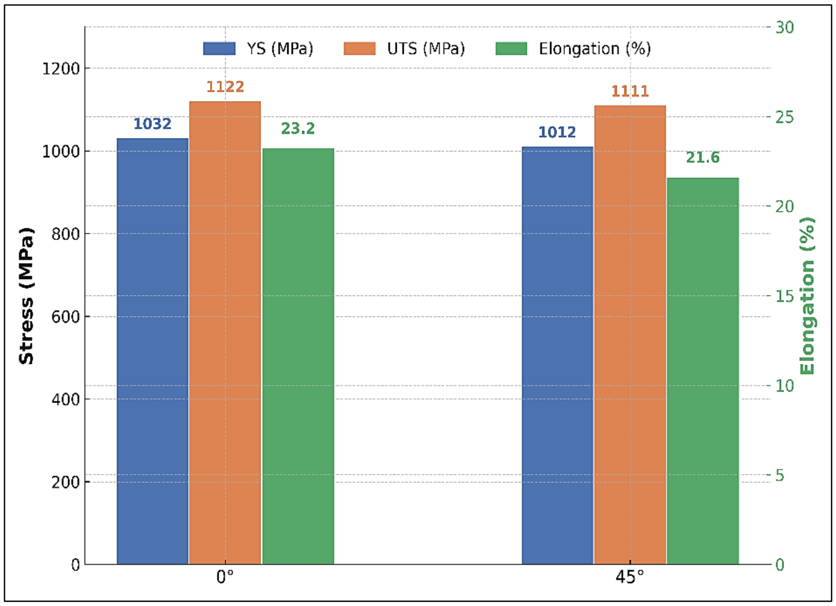

Figure 4.4: Comparison of tensile mechanical properties: yield strength (YS), ultimate tensile strength (UTS), and elongation at break of LPBF 17-4 PH specimens built at 0° and 45° orientations.

These findings are consistent with prior reports in the literature. Moyle et al. [9] attributed corresponding orientation-dependent behavior to residual stress concentrations and grain boundary misorientations, and assigned lower tensile strength in inclined orientations. Peng et al. [18] similarly observed that horizontally printed 17-4 PH showed better yield strength and ductility compared to off-axis orientations, owing to improved layer-to-layer fusion and decreased pore density parallel to the axis of loading.

Furthermore, the high elongation values obtained in both directions (more than 21%) reflect the success of the selected H1025 heat treatment cycle, which promotes a fine-grained martensite matrix with fine precipitation and controlled residual austenite fraction, resulting in strain-hardening and necking delay. The synergy of optimized process parameters, high density, and fine-grained microstructure minimized large clusters of defects that are typically the early sites for crack nucleation in LPBF components [19].

In summary, while both orientations have good mechanical properties suitable for structural application, the modestly greater static strength and ductility of the horizontal orientation reflect the beneficial effect of aligned interfaces between layers and uniform stress distribution. These orientation-induced variations, while modest under static loading, are likely to have a larger effect on fatigue behaviour, as discussed in the next section.

4.2.4.2 Fatigue behaviour

The fatigue tests were performed under **stress-controlled conditions**, enabling the characterization of both low-cycle fatigue (LCF) and high-cycle fatigue (HCF) regimes. Extensive microstructural observations and fractographic examinations, are presented in this section relative to the effect of build direction on the cyclic response of LPBF 17-4 PH stainless steel under optimized processing conditions.

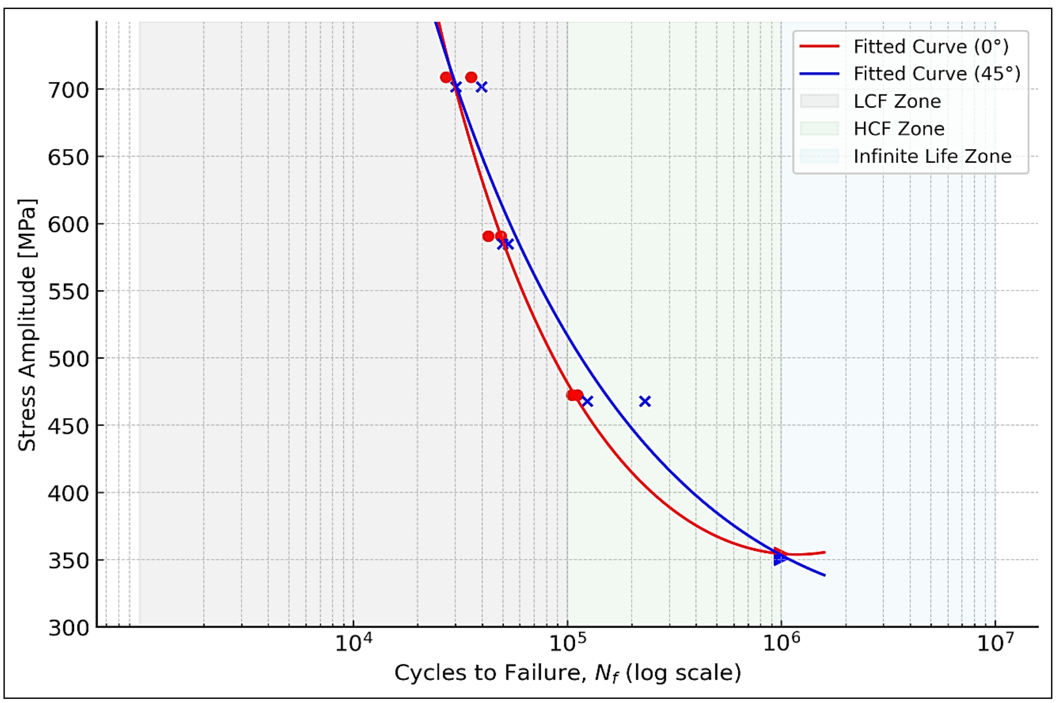

Figure 4.5:Stress–life (S–N) curves comparing the fatigue performance of LPBF 17-4 PH specimens built at 0° and 45° orientations under optimal processing parameters.

The experimentally obtained S–N curves (Figure 4.5 and Table 4.2) show clear differences between the two orientations. Specimens built horizontally exhibited superior fatigue resistance across the entire range of applied stress amplitudes. The fitted curves clearly indicate that the horizontal orientation gave a greater endurance limit, estimated at approximately 355 MPa (as defined at 10^6 cycles), whereas the 45° orientation had showed a close but slightly lower value of ~351 MPa, a reduction of approximately 1.5%. However, in low- and middle-cycle regimes (LCF and transition zones), 45° specimens always sustained more cycles to failure. At stress amplitudes of ~470 MPa, for instance, inclined samples survived up to 230,000 cycles while horizontal ones failed at about 105,000 cycles.

Table 4.2: Fatigue life cycles for both specimen orientation 0° and 45° printed under optimum processing parameters.

Orientation	Cycles	Stress (MPa)
0°	27 027	708.7
	35 516	708.7
	48 943	590.58
	42 625	590.58
	105 054	472.46
	111 084	472.46
	1 000 001	354.35
	1 000 000	354.35
45°	30 142	701.75
	39 611	701.75
	49 938	584.8
	52 756	584.8
	123 747	467.83
	230 000	467.83
	1 000 000	350.88
	1 000 000	350.88

This difference in fatigue behavior is attributed to the defect distribution and microstructural anisotropy dependent on the orientation of the LPBF process. Horizontally oriented specimens benefit from the alignment of layers along the load direction, which reduces the influence of layer-boundary defects and lack-of-fusion pores as stress concentrators [20]. For the inclined (45°) orientation, inclined layer interfaces and partially misaligned pores are subjected to the applied cyclic loading, allowing premature crack initiation [21].

The spread of the fatigue data in both orientations corresponds to the randomness of the porosity distribution and surface micro-defects. However, it must be noted that the optimized processing parameters, which provided a measured density of 98.92% and very low porosity, significantly reduced this spread compared to values reported in the literature for LPBF components made under less constrained parameters [8], [22].

In parallel, the assessed decrease of the fatigue strength difference between inclined and horizontal planes is in harmony with Sepe et al. [11], which illustrated that orientation-forming stress concentration zones allow prevenient locations of crack initiation when subjected to cyclic loading. Lower interlayer misfit and a more uniformly spread load transfer during the horizontal orientation result in superior resistance against the premature onset of cracks and crack propagation rates and, thus, higher fatigue durability.

The inclination of the fitted S–N curve also indicates that the inclined orientation has a stronger decline in fatigue strength with reducing cycles, suggesting that short-life failures are more dependent on localized defects and layer misorientation. This is particularly the case at the transition from LCF to HCF regimes where microstructural integrity becomes increasingly important.

Overall, the findings justify that even under optimized conditions of low porosity and well-controlled heat treatment, build orientation remains an important factor governing fatigue performance. The horizontal orientation surpasses the 45° build orientation in all cases, and the lead of the former increases with the increase in cyclic life. These findings validate the significance of careful planning of orientation strategies in LPBF-produced components destined to operate under fatigue-critical conditions.

4.2.4.3 Fractographic analysis

To support the fatigue performance results, SEM fractographic analysis was carried out on selected specimens from both orientations, tested at two different stress amplitudes. Figure 4.6 presents representative SEM images of the fracture surfaces at a high applied stress level. For the horizontal orientation, cracks initiated at surface-adjacent defects, likely pores, and propagated along planar paths consistent with the build layers. High magnification images revealed striations radiating from these initiation sites and regions of ductile rupture characterized by dimples.

In the 45° inclined orientation, cracks exhibited more irregular propagation fronts. The presence of oblique striations suggested interaction with angled melt pool boundaries. The rupture surface showed broader plastic zones, indicating a more energy-dissipative failure mechanism. These observations confirm the enhanced fatigue life observed in S–N results, likely driven by crack deflection and increased resistance to propagation.

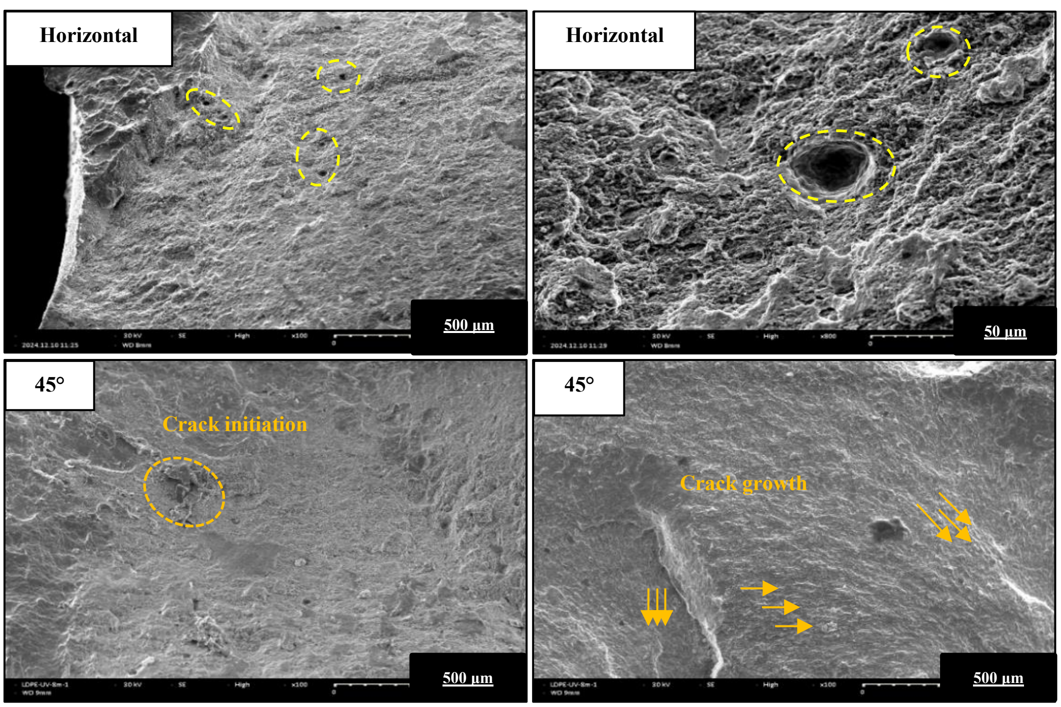

Figure 4.6: SEM fractographic images of LPBF 17-4 PH specimens tested under fatigue loading at high stress amplitude: a)-b): horizontal build specimen, c)-d): 45° build specimen.

Figure 4.7 provides additional micrographs for the specimens tested at a stress, characteristic of the high-cycle fatigue regime.

In horizontal fractures, the fracture initiation was at the outer surface and extended along periodic, layer-normal planes. Rounding pores observed in high magnification images promoted fatigue crack growth. The final fracture area showed signs of ductile overload, with classic dimple morphology due to micro void coalescence.

In the 45° builds, cracks again initiated sub-surface, but the crack front followed a deflected path with denser striations. The final rupture surface appeared rougher and more heterogeneous, confirming that crack growth was more complex and delayed — consistent with the improved fatigue life observed in S–N analysis.

This performance is consistent with literature suggesting that inclined orientations induce more tortuous crack paths, as the crack propagates across oblique melt pool boundaries rather than parallel to them. As reported by Yadollahi et al. [22] and Foti et al. [23], this increased tortuosity requires more energy for crack advancement and contributes to delayed failure. The crack propagation in 0° specimens, being more aligned with the layer structure, progresses more easily and fails earlier under the same loading conditions.

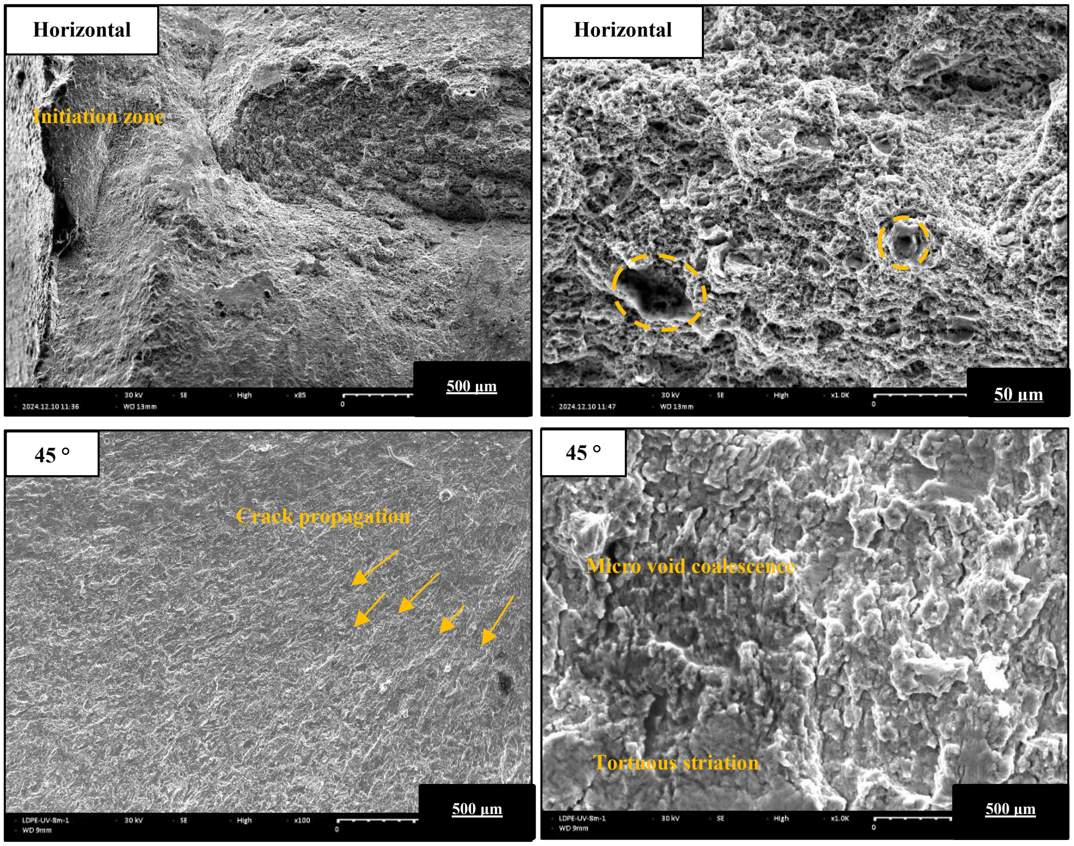

Figure 4.7: Fractographic SEM images of LPBF 17-4 PH specimens fractured under lower fatigue stress amplitude: a)-b): horizontal build specimen, c)-d): 45° build specimen.

In summary, fractographic findings corroborated mechanical findings and underscored the effect of build orientation on fatigue crack behavior. Horizontal samples tended to develop and propagate cracks more readily along layer-parallel directions, often aided by internal defects. More complex crack development was noted for inclined samples, with failure postponed through deflection, energy absorption along melt pool boundaries, and ductile tearing.

These findings confirm that in spite of optimized process conditions, microstructural anisotropy and geometrical layering inherent in LPBF have a significant influence on fatigue performance and fracture morphology.

4.2.5 Conclusion

In this study, the effect of the build orientation on the fatigue behavior of LPBF 17-4 PH stainless steel under optimal process and post-processing condition was assessed. Although with the similar endurance limit (~355 MPa for 0° and ~351 MPa for 45°), inclined specimens exhibited longer fatigue life in the low- and middle-cycle regimes, which confirmed the beneficial role of oblique orientations to slow down the crack growth.

- Horizontal (0°) samples showed planar crack growth along layer deposition, often initiated by surface near pores.

- 45° specimens inclined revealed more tortuous growth paths and larger ductility in terminal rupture regions, consistent with larger resistance to fatigue failure.

- Fractographic examination confirmed these trends, revealing obvious microstructural processes behind orientation-controlled fatigue behavior.

These findings indicate that building direction remains a significant design parameter even when optimized processing conditions are employed. The conclusions drawn here are of specific interest for the qualification and fatigue optimization of AM parts in industrial applications where high cycle longevity and directional integrity are necessary.

4.2.6 References

[1] S. A. M. Tofail, E. P. Koumoulos, A. Bandyopadhyay, S. Bose, L. O'Donoghue, and C. Charitidis, 'Additive manufacturing: scientific and technological challenges, market uptake and opportunities', *Materials Today*, vol. 21, no. 1, pp. 22–37, Jan. 2018, doi: 10.1016/j.mattod.2017.07.001.

[2] R. Rahmani, B. Bashiri, S. I. Lopes, A. Hussain, H. S. Maurya, and R. Vilu, 'Sustainable Additive Manufacturing: An Overview on Life Cycle Impacts and Cost Efficiency of Laser Powder Bed Fusion', *JMMP*, vol. 9, no. 1, p. 18, Jan. 2025, doi: 10.3390/jmmp9010018.

[3] S. R. Narasimharaju *et al.*, 'A comprehensive review on laser powder bed fusion of steels: Processing, microstructure, defects and control methods, mechanical properties, current challenges and future trends', *Journal of Manufacturing Processes*, vol. 75, pp. 375–414, Mar. 2022, doi: 10.1016/j.jmapro.2021.12.033.

[4] N. Hou *et al.*, ‘Failure modes, mechanisms and causes of shafts in mechanical equipment’, *Engineering Failure Analysis*, vol. 136, p. 106216, Jun. 2022, doi: 10.1016/j.engfailanal.2022.106216.

[5] F. Xue, Z.-X. Wang, W.-S. Zhao, X.-L. Zhang, B.-P. Qu, and L. Wei, ‘Fretting fatigue crack analysis of the turbine blade from nuclear power plant’, *Engineering Failure Analysis*, vol. 44, pp. 299–305, Sep. 2014, doi: 10.1016/j.engfailanal.2014.05.006.

[6] T. H. Becker, P. Kumar, and U. Ramamurty, ‘Fracture and fatigue in additively manufactured metals’, *Acta Materialia*, vol. 219, p. 117240, Oct. 2021, doi: 10.1016/j.actamat.2021.117240.

[7] H. Bakhtiari, M. Aamir, and M. Tolouei-Rad, ‘Effect of 3D Printing Parameters on the Fatigue Properties of Parts Manufactured by Fused Filament Fabrication: A Review’, *Applied Sciences*, vol. 13, no. 2, p. 904, Jan. 2023, doi: 10.3390/app13020904.

[8] A. Alhajeri, O. Aremu, M. Almutahhar, M. Yousif, J. Albinmousa, and U. Ali, ‘On the effect of loading and printing parameters that influence the fatigue behavior of laser powder-bed fusion additively manufactured steels’, *Heliyon*, vol. 10, no. 9, p. e29229, May 2024, doi: 10.1016/j.heliyon.2024.e29229.

[9] M. S. Moyle *et al.*, ‘Correlation of microstructure, mechanical properties, and residual stress of 17-4 PH stainless steel fabricated by laser powder bed fusion’, *Journal of Materials Science & Technology*, vol. 198, pp. 83–97, Nov. 2024, doi: 10.1016/j.jmst.2024.01.080.

[10] Y. Zhang, ‘Review: corrosion and stress corrosion cracking of wrought and additively manufactured 17-4 PH stainless steel’, National Physical Laboratory, Feb. 2022. doi: 10.47120/npl.MAT100.

[11] R. Sepe, V. Giannella, V. Alfieri, and F. Caiazzo, ‘Static and fatigue behavior of laser welded additively manufactured 17-4 PH steel plates’, *Procedia Structural Integrity*, vol. 34, pp. 172–177, 2021, doi: 10.1016/j.prostr.2021.12.025.

[12] L. Haas, ‘Reprints available directly from the publisher Photocopying permitted by license only’, *Review of Education, Pedagogy, and Cultural Studies*, vol. 17, no. 1, pp. 1–6, Jan. 1995, doi: 10.1080/1071441950170102.

[13] Y. Sun, R. J. Hebert, and M. Aindow, ‘Effect of heat treatments on microstructural evolution of additively manufactured and wrought 17-4PH stainless steel’, *Materials & Design*, vol. 156, pp. 429–440, Oct. 2018, doi: 10.1016/j.matdes.2018.07.015.

[14] P. Costa, M. Vieira, L. Reis, A. Ribeiro, and M. De Freitas, ‘New specimen and horn design for combined tension and torsion ultrasonic fatigue testing in the very high cycle fatigue regime’, *International Journal of Fatigue*, vol. 103, pp. 248–257, Oct. 2017, doi: 10.1016/j.ijfatigue.2017.05.022.

[15] C. Ye, C. Zhang, J. Zhao, and Y. Dong, ‘Effects of Post-processing on the Surface Finish, Porosity, Residual Stresses, and Fatigue Performance of Additive Manufactured Metals: A Review’, *J. of Materi Eng and Perform*, vol. 30, no. 9, pp. 6407–6425, Sep. 2021, doi: 10.1007/s11665-021-06021-7.

[16] C. Wei *et al.*, ‘Optimization for achieving robust metallurgical bonding interfaces in the integrated laser additive manufacturing of extremely property-mismatched materials’, *Materials Characterization*, vol. 223, p. 114975, May 2025, doi: 10.1016/j.matchar.2025.114975.

[17] D. Lunt *et al.*, 'The effect of loading direction on strain localisation in wire arc additively manufactured Ti–6Al–4V', *Materials Science and Engineering: A*, vol. 788, p. 139608, Jun. 2020, doi: 10.1016/j.msea.2020.139608.
[18] X. Peng, L. Kong, H. An, and G. Dong, 'A Review of *In Situ* Defect Detection and Monitoring Technologies in Selective Laser Melting', *3D Printing and Additive Manufacturing*, vol. 10, no. 3, pp. 438–466, Jun. 2023, doi: 10.1089/3dp.2021.0114.
[19] M.-K. Kim *et al.*, 'Strategies and Outlook on Metal Matrix Composites Produced Using Laser Powder Bed Fusion: A Review', *Metals*, vol. 13, no. 10, p. 1658, Sep. 2023, doi: 10.3390/met13101658.
[20] E. Eimer *et al.*, 'Effect of inter layer cold work on 2024 aluminium alloy produced by wire directed energy deposition', *Materials Science and Engineering: A*, vol. 880, p. 145272, Jul. 2023, doi: 10.1016/j.msea.2023.145272.
[21] S. Raghavendra, 'Metallurgical and Mechanical Properties of Additively Manufactured Cellular Structures', Mar. 2021, doi: 10.15168/11572_296507.
[22] A. Yadollahi, M. Mahmoudi, A. Elwany, H. Doude, L. Bian, and J. C. Newman, 'Fatigue-life prediction of additively manufactured material: Effects of heat treatment and build orientation', *Fatigue Fract Eng Mat Struct*, vol. 43, no. 4, pp. 831–844, Apr. 2020, doi: 10.1111/ffe.13200.
[23] P. Foti, N. Razavi, A. Fatemi, and F. Berto, 'Multiaxial fatigue of additively manufactured metallic components: A review of the failure mechanisms and fatigue life prediction methodologies', *Progress in Materials Science*, vol. 137, p. 101126, Aug. 2023, doi: 10.1016/j.pmatsci.2023.101126.

CONCLUSION GÉNÉRALE

Ce travail de recherche avait pour objectif principal d'optimiser les propriétés mécaniques, microstructurales et de durabilité en fatigue de l'acier inoxydable martensitique 17-4 PH produit par fusion laser sur lit de poudre (LPBF). L'approche méthodologique adoptée, à la fois systématique et expérimentale, a permis d'atteindre efficacement les objectifs spécifiques de cette étude : l'évaluation expérimentale et statistique de l'effet combiné des paramètres du procédé LPBF et des traitements thermiques sur la microstructure et la microdureté, l'analyse comparative de leurs effets sur les propriétés mécaniques en traction, l'investigation de la ténacité aux chocs via des essais Charpy, et l'étude approfondie du comportement en fatigue selon l'orientation d'impression.

Sur le plan microstructural et de la microdureté, les résultats ont clairement démontré que, bien que les paramètres LPBF influencent la porosité des pièces, c'est principalement la température de vieillissement qui détermine la microstructure finale et les performances mécaniques associées. Le traitement thermique H1150 (620 °C) s'est avéré particulièrement efficace pour améliorer la ductilité et offrir une excellente résistance aux chocs (120 J), tandis que H900 (480 °C) favorise une augmentation de la dureté et de la résistance mécanique, mais au détriment de la ductilité. Ces résultats apportent une compréhension plus fine des mécanismes de précipitation et constituent un guide opérationnel pour choisir les conditions de traitement en fonction des besoins industriels.

En traction, l'étude a mis en lumière l'importance cruciale du contrôle de la densité d'énergie volumique (VED). Une VED trop élevée, bien que favorable à une densité accrue, peut accroître la fragilité du matériau, surtout lorsqu'elle est combinée à un vieillissement à basse température. À l'inverse, la condition H1025 est apparue comme une solution optimale pour obtenir un compromis équilibré entre résistance, dureté et ductilité. Ce résultat a une portée pratique importante, car il fournit aux concepteurs un levier stratégique pour adapter les performances des pièces aux exigences spécifiques de leur domaine d'application.

L'investigation de la ténacité aux chocs a confirmé que le traitement thermique H1150 favorise la formation de précipités grossiers et améliore considérablement la capacité d'absorption d'énergie, avec des valeurs atteignant 120 J. Ces observations soulignent le rôle déterminant des conditions de vieillissement dans la maîtrise de la résilience, et permettent de proposer des recommandations concrètes pour les industries critiques telles que l'aéronautique et l'automobile, où la résistance aux chocs demeure un critère déterminant pour la sécurité.

Enfin, l'étude du comportement en fatigue selon l'orientation d'impression (0° et 45°) a révélé que, malgré des limites d'endurance similaires, les éprouvettes inclinées à 45° présentent une durée de vie plus longue dans les régimes à faible et moyen nombre de cycles. Cette amélioration est attribuée à des chemins de fissuration plus tortueux, ralentissant la propagation des fissures et favorisant une ductilité terminale accrue. Ces résultats renforcent l'idée que l'orientation d'impression est un paramètre clé à considérer spécifiquement pour les applications soumises à des chargements cycliques, et complètent les travaux antérieurs qui portaient davantage sur la traction et l'impact.

Dans l'ensemble, ce travail apporte donc une contribution significative à la maîtrise du procédé LPBF appliqué à l'acier 17-4 PH, en fournissant des corrélations quantitatives et des recommandations précises directement applicables dans un cadre industriel exigeant. Au-delà des résultats expérimentaux, il propose également une démarche méthodologique qui peut être généralisée à d'autres alliages utilisés en fabrication additive.

Toutefois, malgré ces avancées importantes, plusieurs perspectives de recherche future méritent d'être explorées :

- L'étude plus approfondie de l'impact des porosités résiduelles sur les performances mécaniques locales et globales.

- L’utilisation d’approches avancées comme l’apprentissage automatique et les simulations numériques multiphysiques pour affiner la prédiction et l’optimisation des paramètres du procédé.
- L’évaluation à long terme de la stabilité microstructurale et mécanique sous conditions de service réelles, notamment dans des environnements agressifs ou à haute température.
- L’analyse économique et énergétique du procédé LPBF pour en faciliter l’adoption à grande échelle par l’industrie.

En définitive, cette recherche ouvre des perspectives prometteuses pour une intégration accrue de la technologie LPBF dans les industries de pointe. Elle souligne l’importance d’une approche multidisciplinaire, combinant métallurgie, mécanique des matériaux, modélisation numérique et ingénierie de la production, afin de relever les défis restants et d’exploiter pleinement le potentiel exceptionnel de la fabrication additive métallique.

ANNEXES

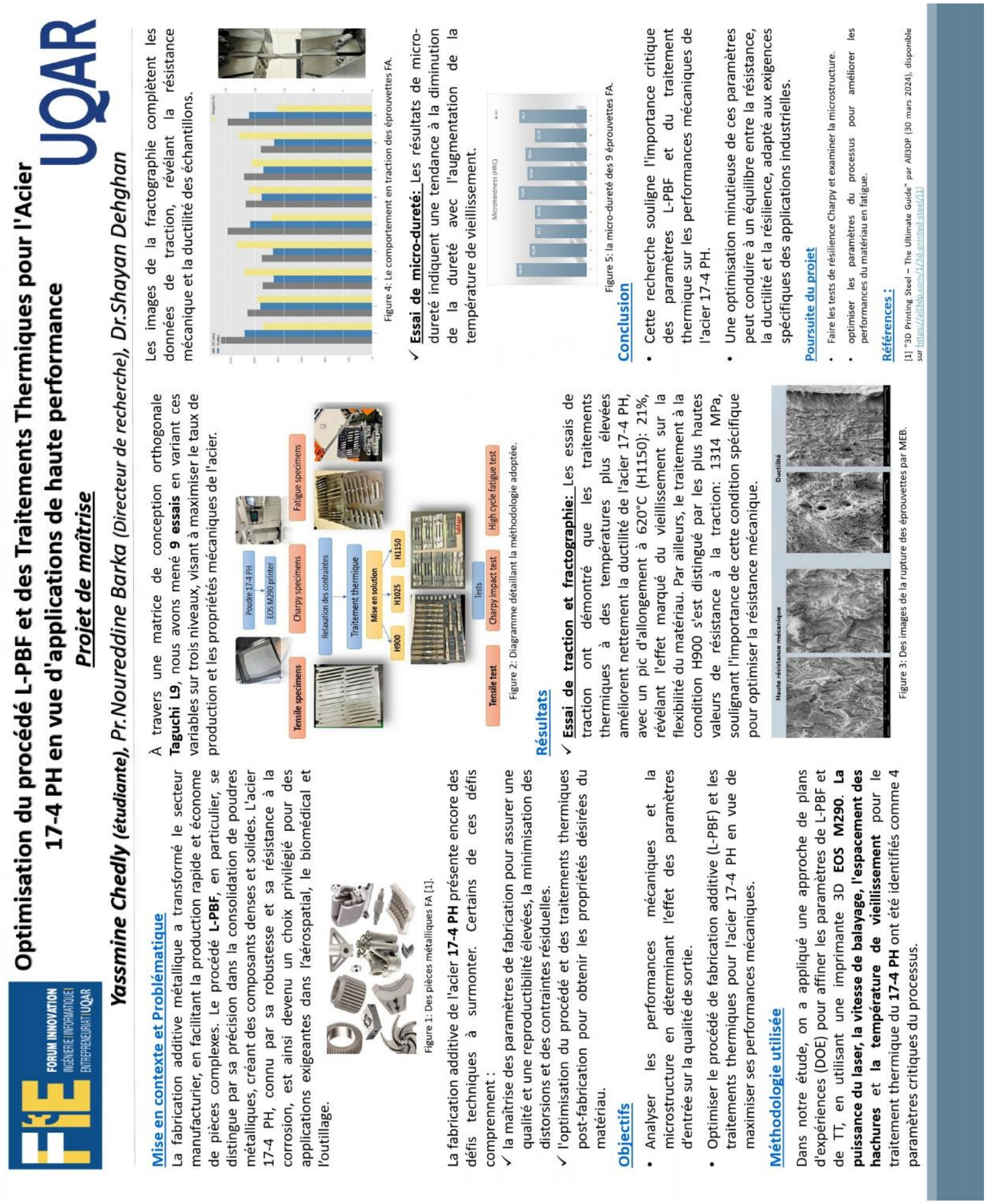

Annexe I : **Affiche scientifique – 2e Prix au Forum FI3E (Innovation–Ingénierie–Informatique–Entrepreneuriat), UQAR – Avril 2024**

<u>Optimisation du procédé LPBF et des Traitements Thermiques pour l'Acier 17-4 PH - Université du Québec à Rimouski</u>

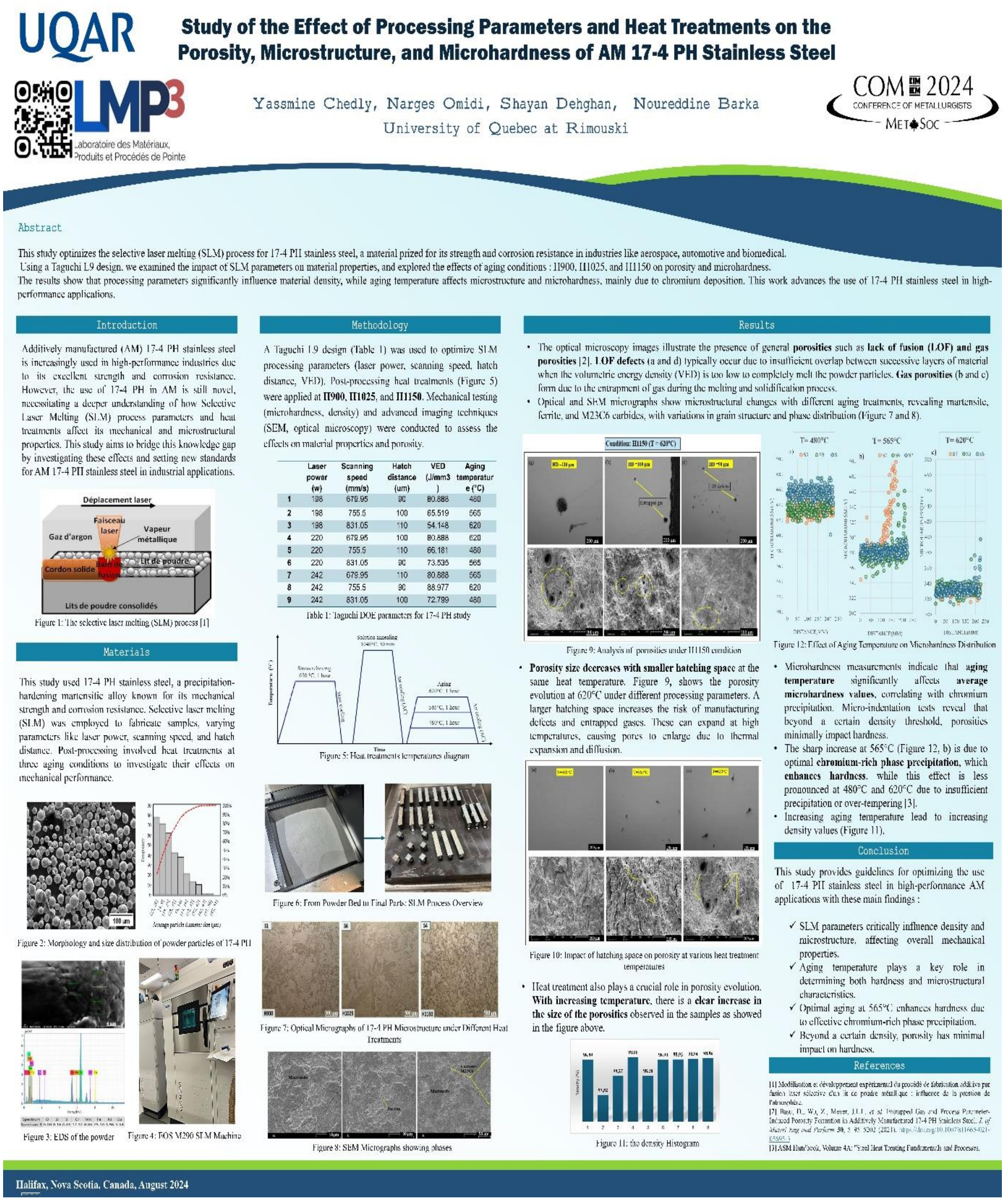

Annexe II : **Affiche scientifique – Prix de la meilleure présentation étudiante à la conférence COM 2024 (63e Conférence annuelle des métallurgistes, MetSoc – CIM) – Août 2024**

Optimisation des performances mécaniques de l'acier inoxydable 17-4 PH fabriqué par fabrication additive

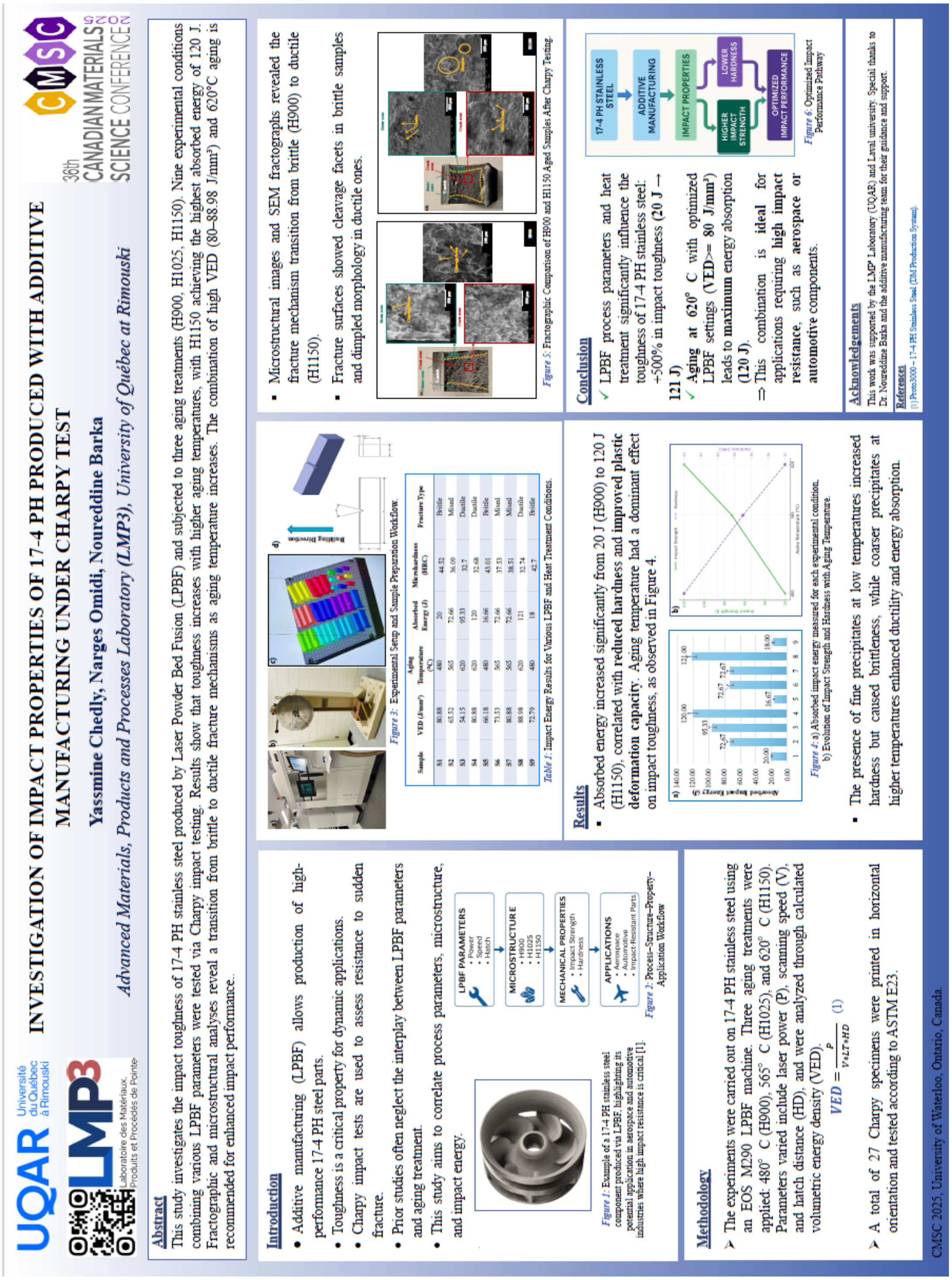

Annexe III : **Affiche scientifique au conférence CMSC 2025 « The 36th Canadian Materials Science Conference », Université de Waterloo – Mai 2025**

RÉFÉRENCES BIBLIOGRAPHIQUES

[1] P. Lesage, ‘Etude et caractérisation sous sollicitations dynamiques de structures mécaniques en fabrication additive et soustractive’.

[2] J.-C. André, *De la fabrication additive à l’impression 3D/4D 1*. ISTE Group, 2018. doi: 10.51926/ISTE.9781784053949.

[3] C. Galy, ‘Etude des interactions matériau/procédé en vue d’une optimisation des conditions opératoires du procédé de fabrication additive SLM sur des alliages d’aluminium pour des applications aéronautiques.’

[4] L. Jiao, Z. Y. Chua, S. K. Moon, J. Song, G. Bi, and H. Zheng, ‘Femtosecond Laser Produced Hydrophobic Hierarchical Structures on Additive Manufacturing Parts’, *Nanomaterials*, vol. 8, no. 8, p. 601, Aug. 2018, doi: 10.3390/nano8080601.

[5] A. Baumard, ‘Prédiction des structures de grain d’un composant en acier 316L élaboré par fabrication additive fusion laser sur lit de poudre’.

[6] M. Lelievre, ‘Elaboration de l’alliage Ni 20 wt. % Cr par fusion sélective laser : effet des paramètres de fabrication sur la microstructure, le comportement mécanique en traction et la stabilité thermique.’, matériaux, Normandie Université, 2021.

[7] O. Andreau, ‘Nocivité en fatigue et contrôle de défauts produits par fabrication additive’.

[8] S. E. Brika, M. Letenneur, C. A. Dion, and V. Brailovski, ‘Influence of particle morphology and size distribution on the powder flowability and laser powder bed fusion manufacturability of Ti-6Al-4V alloy’, *Additive Manufacturing*, vol. 31, p. 100929, Jan. 2020, doi: 10.1016/j.addma.2019.100929.

[9] W. Chen *et al.*, ‘Effect of heat treatment on microstructure and performances of additively manufactured 15-5PH stainless steel’, *Optics & Laser Technology*, vol. 157, p. 108711, Jan. 2023, doi: 10.1016/j.optlastec.2022.108711.

[10] P. Nyamekye, R. Lakshmanan, V. Tepponen, and S. Westman, ‘Sustainability aspects of additive manufacturing: Leveraging resource efficiency via product design optimization and laser powder bed fusion’, *Heliyon*, vol. 10, no. 1, p. e23152, Jan. 2024, doi: 10.1016/j.heliyon.2023.e23152.

[11] J. Bae, M. Kim, E. Oh, K.-T. Yang, and J. Suhr, ‘Experimental and numerical investigation of 17–4PH stainless steel fabricated by laser powder bed fusion and hot isostatic pressing’, *Mater. Res. Express*, vol. 8, no. 10, p. 106512, Oct. 2021, doi: 10.1088/2053-1591/ac2b55.

[12] P. Sahadevan, C. P. Selvan, A. Bhaumik, and A. Lakshmikantha, ‘Selective Laser Melting Parametric Optimization for Microhardness of 17-4 PH Stainless Steel’, *jmmf*, pp. 2512–2519, Dec. 2023, doi: 10.18311/jmmf/2023/35128.

[13] Y. Otsuka, Y. Kondo, T. T. Duong, E. Mitsuhashi, and Y. Miyashita, ‘Synergistic effect of defects and microstructure on fatigue strength of additively manufactured precipitation hardening 17-4PH stainless steel’, *Engineering Failure Analysis*, vol. 163, p. 108541, Sep. 2024, doi: 10.1016/j.engfailanal.2024.108541.

[14] C. Li, Y. Chen, X. Zhang, T. Liu, Y. Peng, and K. Wang, ‘Effect of heat treatment on microstructure and mechanical properties of 17-4PH stainless steel manufactured by laser-powder bed fusion’, *Journal of Materials Research and Technology*, vol. 26, pp. 5707–5715, Sep. 2023, doi: 10.1016/j.jmrt.2023.08.283.

[15] S. Afkhami, M. Dabiri, H. Piili, and T. Björk, ‘Effects of manufacturing parameters and mechanical post-processing on stainless steel 316L processed by laser powder bed fusion’, *Materials Science and Engineering: A*, vol. 802, p. 140660, Jan. 2021, doi: 10.1016/j.msea.2020.140660.

[16] R. Huang *et al.*, ‘Additive manufacturing of 17-4PH stainless steel: Effect of heat treatment on microstructure evolution and strengthening behavior’, *Materials Science and Engineering: A*, vol. 908, p. 146770, Aug. 2024, doi: 10.1016/j.msea.2024.146770.

[17] H. Eisazadeh, S. Khadka, X. Wang, and P. Yuya, ‘A comparative study of the mechanical characteristics of additively and conventionally fabricated 17-4 precipitation hardened stainless steel’, *Prog Addit Manuf*, vol. 9, no. 6, pp. 2445–2463, Dec. 2024, doi: 10.1007/s40964-024-00591-3.

[18] M. Parsazadeh, S. Sharma, and N. Dahotre, ‘Towards the next generation of machine learning models in additive manufacturing: A review of process dependent material evolution’, *Progress in Materials Science*, vol. 135, p. 101102, Jun. 2023, doi: 10.1016/j.pmatsci.2023.101102.

[19] R. R. Kyarimov, E. S. Statnik, I. A. Sadykova, A. A. Frantsuzov, A. I. Salimon, and A. M. Korsunsky, ‘Factorial-experimental investigation of LPBF regimes for VZh159 nickel superalloy grain structure and structural strength optimization’, *Front. Mater.*, vol. 11, p. 1470651, Oct. 2024, doi: 10.3389/fmats.2024.1470651.

[20] S. F. Nabavi, H. Dalir, and A. Farshidianfar, ‘A comprehensive review of recent advances in laser powder bed fusion characteristics modeling: metallurgical and defects’, *Int J Adv Manuf Technol*, vol. 132, no. 5–6, pp. 2233–2269, May 2024, doi: 10.1007/s00170-024-13491-1.

[21] S. Saha and S. Roy, ‘Metallic Dental Implants Wear Mechanisms, Materials, and Manufacturing Processes: A Literature Review’, *Materials*, vol. 16, no. 1, p. 161, Dec. 2022, doi: 10.3390/ma16010161.

[22] S. Sabooni *et al.*, ‘Laser powder bed fusion of 17–4 PH stainless steel: A comparative study on the effect of heat treatment on the microstructure evolution and mechanical properties’, *Additive Manufacturing*, vol. 46, p. 102176, Oct. 2021, doi: 10.1016/j.addma.2021.102176.

[23] H. R. Lashgari, C. Kong, E. Adabifiroozjaei, and S. Li, ‘Microstructure, post thermal treatment response, and tribological properties of 3D printed 17-4 PH stainless steel’, *Wear*, vol. 456–457, p. 203367, Sep. 2020, doi: 10.1016/j.wear.2020.203367.